

**MODELLING OF A CAPILLARY  
DISCHARGE SOFT X-RAY LASER**

**TEH CHEW PENG**

**THESIS SUBMITTED IN FULFILLMENT OF THE  
REQUIREMENTS FOR THE DEGREE OF  
DOCTOR OF PHILOSOPHY**

**DEPARTMENT OF PHYSICS  
FACULTY OF SCIENCE  
UNIVERSITY OF MALAYA  
KUALA LUMPUR**

**2013**

# UNIVERSITI MALAYA

## ORIGINAL LITERARY WORK DECLARATION

Name of Candidate: Teh Chew Peng (I.C/Passport No: 781126-14-5462 )

Registration/Matric No: SHC070018

Name of Degree: PhD

Title of Project Paper/Research Report/Dissertation/Thesis ("this Work"):

MODELLING OF A CAPILLARY DISCHARGE SOFT X-RAY LASER

Field of Study: COMPUTATIONAL LASER PHYSICS

I do solemnly and sincerely declare that:

- (1) I am the sole author/writer of this Work;
- (2) This Work is original;
- (3) Any use of any work in which copyright exists was done by way of fair dealing and for permitted purposes and any excerpt or extract from, or reference to or reproduction of any copyright work has been disclosed expressly and sufficiently and the title of the Work and its authorship have been acknowledged in this Work;
- (4) I do not have any actual knowledge nor do I ought reasonably to know that the making of this work constitutes an infringement of any copyright work;
- (5) I hereby assign all and every rights in the copyright to this Work to the University of Malaya ("UM"), who henceforth shall be owner of the copyright in this Work and that any reproduction or use in any form or by any means whatsoever is prohibited without the written consent of UM having been first had and obtained;
- (6) I am fully aware that if in the course of making this Work I have infringed any copyright whether intentionally or otherwise, I may be subject to legal action or any other action as may be determined by UM.

Candidate's Signature

Date

Subscribed and solemnly declared before,

Witness's Signature

Date

Name:

Designation:

## Abstract

This work presents a numerical study of a Neon-like Argon capillary discharge x-ray laser. We outline the theoretical framework and present the results of the numerical investigations of a one-dimensional single-fluid magneto-hydrodynamics (MHD) model, with separate electron and ion temperatures, of a capillary-discharge collisional soft x-ray laser. The MHD equations are solved by the Lagrangian cylindrical geometry approach. The effects of the gas filling pressure on the plasma densities and temperatures during the implosion-pinch phase have been investigated. In addition, gas filling pressure effects on the laser intensity for soft x-ray lasing conditions at a wavelength of 46.9 nm of argon filled gas inside the capillary have been analyzed. The results are compared with experimental measurements at the operating pressure ranges (0.1 – 0.4 mbar). Besides this, other input parameters such as capillary radius, peak current and current rise-time have also been considered in this study to optimize lasing conditions. The MHD model has also been studied to investigate the possibility of a nitrogen x-ray laser operating at the wavelength of 13.4 nm.

## Abstrak

Kerja ini membentangkan kajian berangka suatu laser sinar-x nyahcas rerambut Argon bak Neon. Kami menggariskan rangka kerja teori dan membentangkan keputusan siasatan berangka model magneto-hidrodinamik (MHD) bendalir tunggal dalam satu-dimensi, dengan suhu elektron dan ion berasingan, bagi suatu laser sinar-x lembut perlanggaran nyahcas rerambut. Persamaan MHD diselesaikan dengan pendekatan geometri silinder Lagrangian. Kesan tekanan isian gas ke atas ketumpatan dan suhu plasma semasa fasa letupan-picit (*pinch*) telah disiasat. Di samping itu, kesan tekanan isian gas ke atas intensiti laser untuk keadaan laser sinar-x lembut pada panjang gelombang 46.9 nm dengan isian gas argon di dalam tiub rerambut telah dianalisis. Keputusan dibandingkan dengan ukuran eksperimen pada julat tekanan kendalian (0.1 – 0.4 mbar). Selain daripada ini, parameter input yang lain seperti jejari rerambut, arus puncak dan masa naik bagi arus juga telah dipertimbangkan dalam kajian ini untuk mengoptimumkan keadaan untuk menghasilkan laser. Model MHD juga telah dikaji untuk menyiasat kemungkinan kendalian laser sinar-x nitrogen pada panjang gelombang 13.4 nm.

## **Acknowledgement**

I would like to express my deep gratitude to Professor Dr. Kwek Kuan Hiang and Professor Dr. Bernardine R. Wong Cheng Kiat, my research supervisors, for their patient guidance, enthusiastic encouragement and useful critiques of this research work. I would like to thank Associate Professor Dr. Chin Oi Hoong for her valuable discussion and comments. I would also like to thank Mr. Zainal, the technicians of the laboratory of physics department for this help in offering me the resources in running the program. My grateful thanks are also extended to my colleagues, Tony Hii King Ung, Vanessa Phung and Patrik Lim, for their spiritual support on this project. Special thanks to University Malaya to provide me Postgraduate Research Funds (PPP), Project No. PS307/2008C and PS330/2009C. Finally, an honorable mention goes to our families and friends for their understandings and supports on me in completing this project. Without helps of the particular that mentioned above, I would face many difficulties while doing this.

# Table of Contents

	Page
Abstract	iii
Abstrak	iv
Acknowledgements	v
List of figures	ix
List of tables	xiii
 <b>Chapter 1 Introduction</b>	 1
1.1 Extreme Ultraviolet and Soft X-ray Sources	1
1.1.1 Synchrotron Sources	3
1.1.2 Non-linear Harmonic Generation	4
1.1.3 Plasma Sources	5
1.1.3.1 Laser-produced Plasma Sources	8
1.1.3.2 Capillary Discharge Plasma Sources	10
1.2 X-ray Laser Sources	10
1.3 Applications of Short Wavelength Radiation	11
1.4 Overview of X-ray Lasers	12
1.5 Thesis Overview	14
 <b>Chapter 2 Theoretical Background</b>	 16
2.1 Introduction	16
2.2 Fundamental Laser Theory	16
2.3 Specific Concepts in X-ray Lasing	22
2.3.1 Recombination Pumping	26
2.3.1.1 X-ray Laser Experiments Using Recombination Pumping	30
2.3.2 Collisional Excitation Pumping	31
2.3.2.1 X-ray Laser Experiments Using Collisional Excitation Pumping	34
2.4 Capillary Discharge Driven Plasmas	34
2.4.1 Magneto-hydrodynamic Model	36
2.4.2 Coupled Rate Equation of The Plasma	38
2.4.3 Lagrangian Grid Structure	39
2.4.4 Numerical Method	40
2.4.5 Boundary Conditions	41
 <b>Chapter 3 Numerical Study of a Capillary Discharged Neon-like Argon X-Ray Laser</b>	 42
3.1 Properties of Argon Plasma in Equilibrium	42

3.2	Population and gain requirements for Ne-like Ar	46
3.3	Case Study: Ionization Dynamics and One-dimensional MHD Model	49
3.4	The Initial Parameters	49
3.5	Results of MHD Simulations	50
3.6	Argon Ionization And Energy Level Populations	54
3.7	Gain Factor Time Dependence	56
3.8	Influence of Opacity on Gain Coefficients	57
3.9	Comparison with Other Experiments	59
3.9.1	Case 1: Rocca's experiment (1994)	59
3.9.2	Case 2: Niimi's experiment (2002)	62
3.9.3	Case 3: Heinbuch's experiment (2005)	64
<b>Chapter 4</b>	<b>Laser System Optimization of Ne-like Ar Soft X-ray Laser</b>	<b>68</b>
4.1	Dependences of plasma parameters and gain factor on the pressure	68
4.2	Dependences of the pressure-optimized gain factor on the current peak value	71
4.3	A High Current Experiment Study	74
4.4	System Optimization Study of 100 kA Current Peak	78
<b>Chapter 5</b>	<b>Modeling of Capillary Discharge X-ray Image Output Using a Ray-tracing Code</b>	<b>89</b>
5.1	Ray Trajectories And Formalism	91
5.2	Geometry of Code	95
5.3	Numerical Results And Discussions	97
5.4	Analysis of Capillary Discharge Soft X-ray Laser Experiments	103
<b>Chapter 6</b>	<b>Modelling of a Nitrogen X-ray Laser Pumped By Capillary Discharge</b>	<b>107</b>
6.1	Introduction	107
6.2	Principle of Recombination Pumping	107
6.3	A Case Study	109
<b>Chapter 7</b>	<b>Conclusion</b>	<b>117</b>
<b>Appendix</b>		<b>119</b>
A.	Published Work	120
B.	Ray-tracing Code	137
C.	The Derivation of The Energy Balance with Thermal Diffusion for Electrons and Ions	140
D.	The Derivation of The Magnetic Field Transport and Diffusion Equation	141





## List of Figures

	Page
1.1 The wavelength and photon energy ranges and designations of the electromagnetic spectrum from Infrared (IR) to x-ray regions.	2
1.2 Schematic illustration of an undulator used to produce x-ray radiation through oscillating electron motion. Figure taken from Attwood [3].	4
1.3 Harmonic spectrum produced in 13 torr of Ne by 806 nm high intensity laser. Harmonic number 65 would correspond to a wavelength of 12.4 nm. Figure is adapted from Macklin [5].	5
1.4 Schematic diagram of a laser-produced plasma.	8
1.5 Comparison of relative brightness of difference types of EUV and soft x-ray sources. Where markers are shown these represent nominal values for the indicated wavelength. This figure is adapted from Reference [9] and a comparison of other sources with relatively lower brightness can be found therein.	9
1.6 Schematic diagram of the LiH capillary-discharge setup. Figure is adapted from reference [10].	10
2.1 Schematic diagram of a gain medium that supports lasing.	18
2.2 Energy-level diagram and relevant excitation and decay processes of an atomic three-level system.	20
2.3 Recombination scheme for C VI ion. Figure taken from reference [21].	28
2.4 Three-level laser energy diagram with collisional pumping processes shown.	32
2.5 Schematic diagram of energy levels involved in the collisionally excited Ne-like 3p-3s laser in Se and Ar. Taken from Ref. [19].	34
2.6 X-ray pinhole photograph of a pulsed power driven (exploding wire) z-pinch plasma exhibiting extreme axial non-uniformity due to instabilities (Taken from [19]).	35
3.1 Argon ionization fractions dependences on plasma electron temperature for atom density $N_0 \sim 2 \times 10^{18} \text{ cm}^{-3}$ .	45
3.2 Average plasma charge $Z$ for the Argon atom with density $N_0 \sim 2.0 \times 10^{18} \text{ cm}^{-3}$ as a function of temperature.	45
3.3 The contour of gain in 3p $^1S_0 - 3s \ ^1P_1$ transition as function of the electron temperature and density.	48
3.4 Basic parameters of discharge in capillary with diameter of 3 mm filled with argon at a initial gas filling pressure of 0.15 mbar for $I_0 = 16 \text{ kA}$ and rise time 50 ns. (a) The plasma time-space flow diagram; blue line corresponds to the discharge current at outer boundary; (b) contour lines of the decimal logarithm of the electron density (measured $\text{cm}^{-3}$ ) on the $(t, r)$ plane; (c) contour lines of the electron temperature (measured in eV).	51
3.5 Contour lines of the percentage of electric current (which normalized over 16 kA of peak discharge current) inside the region with radius $r$ and time $t$ .	54
3.6 Substantial changes of ionization fraction as a function of the time.	55
3.7 Population densities of Ar ions as a function of time.	56
3.8 The spatial and temporal evolution of gain.	57
3.9 The spatial and temporal evolution of gain after taking opacity effect into account.	58
3.10 Basic parameters of a discharge in a capillary of diameter of 4 mm	61

	filled with argon at a initial gas filling pressure of 700 mTorr for $I_0 = 39$ kA and rise time 30 ns. (a) The plasma time-space flow diagram; the dotted line corresponds to the discharge current at outer boundary; (b) contour lines of the logarithm of the electron density (measured $\text{cm}^{-3}$ ) on the $(t, r)$ plane; (c) contour lines of the electron temperature (measured in eV); (d) contour lines of the fraction of ion $\text{Ar}^{8+}$ ; (e) contour lines of the gain (measured $\text{cm}^{-1}$ ).	
3.11	Basic parameters of discharge in capillary with diameter of 3 mm filled with argon at a initial gas filling pressure of 150 mTorr for $I_0 = 27$ kA and rise time 50 ns. (a) The plasma time-space flow diagram; dotted line corresponds to the discharge current at outer boundary; (b) contour lines of the decimal logarithm of the electron density (measured $\text{cm}^{-3}$ ) on the $(t, r)$ plane; (c) contour lines of the electron temperature (measured in eV); (d) contour lines of the fraction of ion $\text{Ar}^{8+}$ ; (e) contour lines of the gain (measured $\text{cm}^{-1}$ ).	63
3.12	Basic parameters of discharge in capillary with diameter of 3.2 mm filled with argon at a initial gas filling pressure of 700 mTorr for $I_0 = 22$ kA and rise time 30 ns. (a) The plasma time-space flow diagram; dotted line corresponds to the discharge current at outer boundary; (b) contour lines of the decimal logarithm of the electron density (measured $\text{cm}^{-3}$ ) on the $(t, r)$ plane; (c) contour lines of the electron temperature (measured in eV); (d) contour lines of the fraction of ion $\text{Ar}^{8+}$ ; (e) contour lines of the gain (measured $\text{cm}^{-1}$ ).	65
4.1	(a) Maximum compression time versus initial gas filling pressure, (b) Temporal evolution of electron density, (c) Temporal evolution of electron temperature.	69
4.2	Time dependences of the gain factor for alumina capillary ( $r_0 = 1.5$ mm, rise time 50 ns, $I_{max} = 16$ kA) for various initial gas filling pressures (in mbar).	70
4.3	Current wave form for 13.5 kA, 16 kA and 19 kA which are extracted from the experiments of Tan [17].	71
4.4	The electron densities and electron temperature on the axis of the capillary during the maximum compression with various initial gas filling pressures for the peak discharge, $I_{max}$ , of 13.5 kA (black dash line), 16 kA (black solid line) and 19 kA (black dot-dash line) which superposed from the Fig. 3.3.	72
4.5	Dependence of gain factor peak value with opacity effect included on the initial gas filling pressures for current peak of 13.5 kA (dashed line) and 19 kA (solid line).	73
4.6	Basic parameters of discharge in capillary with diameter of 4 mm filled with argon at a initial gas filling pressure of 1.3 Torr for $I_0 = 190$ kA and rise time 18 ns. (a) The plasma time-space flow diagram; dotted line corresponds to the discharge current at outer boundary; (b) contour lines of the decimal logarithm of the electron density (measured $\text{cm}^{-3}$ ) on the $(t, r)$ plane; (c) contour lines of the electron temperature (measured in eV); (d) contour lines of the fraction of ion $\text{Ar}^{8+}$ ; (e) contour lines of the gain (measured $\text{cm}^{-1}$ ).	76
4.7	Contour lines of the percentage of electric current (which normalized over 190 kA of peak discharge current) inside the region with radius $r$ and time $t$ .	77
4.8	(a) Radial motion of outer plasma mass elements, (b) Temporal evolution of electron temperature, (c) Temporal evolution of electron	80

	density (d) Temporal evolution of gain; for various initial gas filling pressures (in mbar) for 100 kA of current peak, 50 ns of current rise time and 6 mm of capillary diameter.	
4.9	(a) Radial motion of outer plasma mass elements, (b) Temporal evolution of electron temperature, (c) Temporal evolution of electron density (d) Temporal evolution of gain; for various initial gas filling pressures (in mbar) for 100 kA of current peak, 75 ns of current rise time and 6 mm of capillary diameter.	82
4.10	(a) Radial motion of outer plasma mass elements, (b) Temporal evolution of electron temperature, (c) Temporal evolution of electron density (d) Temporal evolution of gain; for various initial gas filling pressures (in mbar) for 100 kA of current peak, 100 ns of current rise time and 6 mm of capillary diameter.	83
4.11	Electron density and temperature at peak of the gain of each configuration.	85
4.12	The gain values versus initial gas filling pressure in each configuration.	86
5.1	Coordinate definitions for cylindrical geometry	91
5.2	Electron profile from Eq. (5.12).	93
5.3	Ray trajectories obtained from the electron profile, Eq. (5.7).	94
5.4	The geometry of the code. The plasma is divided into cells along the propagation axis.	95
5.5	Electron density profile at maximum compression by current pulse of 16 kA peak current having rise time about 50 ns with 20 cm long capillaries of 3 mm diameter filled with 0.15 mbar of pure argon gas.	98
5.6	Ray trajectories with stimulated electron density profile for propagation along $z$ at the initial point of $4 \times 10^{-3}$ cm with different launching angles.	99
5.7	Determination of initial launch angle.	99
5.8	Gain profile at maximum compression by current pulse of 16 kA peak current having rise time about 50 ns with 20 cm long capillaries of 3 mm diameter filled with 0.15 mbar of pure argon gas.	100
5.9	Integrated intensity obtained as a function of $z$ . Rays are launched at the time of pinch. The red bold solid curve is obtained with the same code but without refraction effects.	101
5.10	The image of the plasma column at various points along the capillary.	102
5.11	The images of the plasma column in the exit of the capillary and the pinhole.	102
5.12	Comparison experiment at data and the simulation in a 3 mm diameter capillary excited by current pulse of 16 kA peak current having a first half cycle duration of about 50 ns. The full line is meant to guide the eye.	104
5.13	Comparison data of the experiment and the simulation in 3 mm in diameter capillary, excited by current pulse of 19 kA peak current having a first half cycle duration of about 50 ns.	105
6.1	Temperature dependences of nitrogen ionization fractions evaluated according to PrismSPECT code for initial nitrogen atom density $N_0 = 1 \times 10^{18} \text{ cm}^{-3}$ .	108
6.2	Time dependence of the capillary current (dashed line) and trajectories of nitrogen plasma elements inside the capillary which simulated from Helios-CR code.	110
6.3	The evolution of core temperatures and densities of ion and electron simulated from Helios-CR code.	111

6.4	Temporal and spatial evolution of ionization fraction of nitrogen simulated from Helios-CR code.	113
6.5	XRD signals (left axis) and current measurements (right axis) are shown as a function of the time. The legend shows the filter transmission energy (300 – 455 eV Ti, 300 – 575 eV Cr, and 300 – 855 eV Ni). Here the measurement with the initial pressures of N <sub>2</sub> molecules of 0.6 Torr which extracted from Ref. [74].	114
6.6	Time-integrated transmission grating spectroscopy results at four different initial gas densities, 0.6, 1.0, 1.4, and 1.8 Torr. Bottom $x$ axis is the spectrum wavelength $\lambda$ in nanometers. The Top $x$ axis is the spectrum wavelength $E$ in eV, extracted from Ref. [74].	115

## List of Tables

		Page
1.1	Examples of observed x-ray lasers.	14
3.1	The ionization potential was extracted from [43] and peak abundance of Argon was calculated using PrismSPECT code [44].	44
4.1	The summary of the plasma output during the pinch at 2.5 mbar initial gas filling pressure, 100 kA peak current, 6mm capillary diameter and at the various current rise time.	81
4.2	Suggestion of range for the initial gas filling pressures in each capillary diameter.	88
5.1	The prepulse time delay that corresponding to optimum initial gas filling pressure.	105

# Chapter 1

## Introduction

### 1.1 Extreme Ultraviolet and Soft X-ray sources

The extreme ultraviolet (EUV) and soft x-ray spectral regions are two of the more challenging regions of the electromagnetic spectrum within which to develop radiation sources and the applications for these sources. There is no exact definition of the wavelengths for which these two regions encompass, but a rough guideline is shown in Figure 1.1 with the EUV region extending from about 110 nm to approximately 40 nm, and the soft x-ray region spanning 40 nm to nearly 0.1 nm. The difficulty with working at these wavelengths is mainly due to the optical properties of materials in the EUV and soft x-ray regions. The complex index of refraction in solids at these wavelengths is characterized by strong absorption and weak reflectivity. Hence there is a general lack of transmissive and refractive optical materials for such things as windows and lenses. Most gases also begin to absorb strongly below 110 nm due to the first ionization threshold occurring for photons of this energy. This requires either a low pressure or vacuum environments to transmit or propagate the short wavelength radiation to wherever it is to be used. In general these two technical difficulties have hindered the development of radiation sources in this region compared with the visible spectrum. Applications of EUV radiation have also lagged behind those for optical radiation due to the lack of well developed and mature sources. By contrast, visible and ultraviolet lasers were invented in the early 1960s and have undergone nearly 40 years of development. These can now be found in a myriad of applications from communications to medicine.

However the last few decades have been somewhat of a renaissance for activity in EUV and soft x-ray research. This has been due to some achievements of

fundamental physics as well as application driven advancements. Specifically, the demonstration of the first x-ray laser at 20.6 nm in 1985 by Matthews, *et al.* [1] at the Lawrence Livermore National Laboratory brought in a new era of coherent short wavelength research. Around the same time the concept of x-ray and EUV lithography became a much touted future extension to current use of visible optical technology to manufacture microcircuits [2] . This has since fostered an increase in development of high brightness sources.

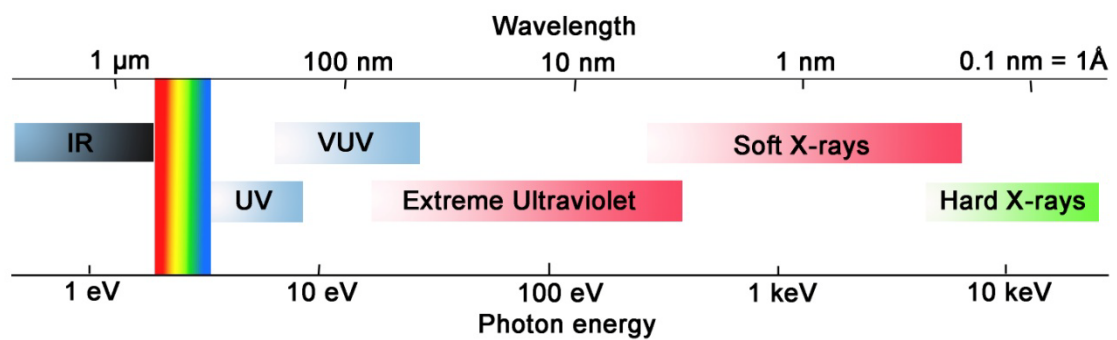


**Figure 1.1** The wavelength and photon energy ranges and designations of the electromagnetic spectrum from Infrared (IR) to x-ray regions.

The different types of EUV and soft x-ray sources can be grouped into categories according to the general characteristics of how the radiation is produced. The three main types are plasma sources, synchrotron sources and non-linear harmonic generation sources. Further classification can be made as to whether the source is coherent, i.e the radiation preserves phase relation, or is incoherent and the radiation has more of a noise-like character. Each of these sources will be briefly introduced by describing their emission characteristics and the general technology behind each source. This thesis examines specifically the dynamics of x-ray lasers which is a subset of plasma sources and will be given a more complete introduction and general overview. However it is important to consider how each of these sources relates to the others and in a way complement each other in terms of potential applications.

EUV and soft x-rays can be produced in three ways; by synchrotron sources, non-linear harmonic generation and plasma sources.

### **1.1.1 Synchrotron sources**

The synchrotron source as a radiating source in the EUV and soft x-ray has been in widespread use since the early 1950s. It has become a reliable source of radiation for basic research and a test bed for many applications. Synchrotron radiation itself is a byproduct of the motion of accelerated charged particles. Large facilities such as the Advanced Light Source (ALS) at the Lawrence Berkeley Laboratory utilize storage rings where the electron beam is circulated and then used to produce radiation. Special insertion devices are placed in the path of the electron beam to produce radiation with specific characteristics, such as wavelength spectrum and spectral qualities. Two general types of insertion devices called undulators and wigglers are in common use today. These devices are periodic arrays of magnets which cause the electron beam to deflect due to the Lorentz force and undergo oscillatory motion and give off synchrotron radiation. Fig. 1.2 shows a schematic diagram of an undulator. The actual spectrum is different in undulators and wigglers. Undulators produce periodic narrow bands of radiation due to interference effects while wigglers produce a more continuous spectrum. One important characteristic of synchrotron radiation is its partial coherence as opposed to the laser-produced plasma and capillary discharge source which are essentially incoherent. This makes synchrotron radiation almost laser-like which is important for applications which require a degree of coherency.



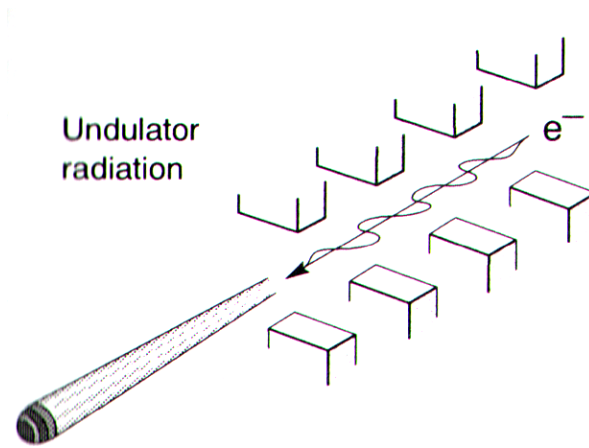


**Figure 1.2** Schematic illustration of an undulator used to produce x-ray radiation through oscillating electron motion. Figure taken from Attwood [3].

### 1.1.2 Non-linear harmonic generation

Production of short wavelength light can also be accomplished by non-linear harmonic generation. This technique has been widely used since the invention of the laser to convert the fundamental frequency of the laser into its second, third and fourth harmonics using non-linear optical crystals. The process of harmonic generation occurs through the interaction of a high intensity beam of light with the nonlinear intensity-dependent response of a material such as crystal or gas. Recently much work has gone into investigating high order harmonic generation in an effort to produce short wavelength radiation. This is accomplished by focusing a high intensity laser into a gas, such as Xenon (Xe) or Neon (Ne). The interaction of the laser with the nonlinear polarizability of the atom can produce very high order harmonics up to 125 or more [4]. Figure 1.3 shows an example of the spectrum of odd orders of the fundamental wavelength generated in a high-order harmonic experiment using Ne gas [5]. High order harmonic generation is a coherent process which can produce extremely bright sources of soft x-ray and EUV radiation as shown in Figure 1.5. The wavelength of the radiation can also be tuned by adjusting the output of the driving lasers, as is common practice

today. Also phase matching techniques in gas-filled capillaries have significantly increased the efficiency of the harmonic output at the shorter wavelengths [6].

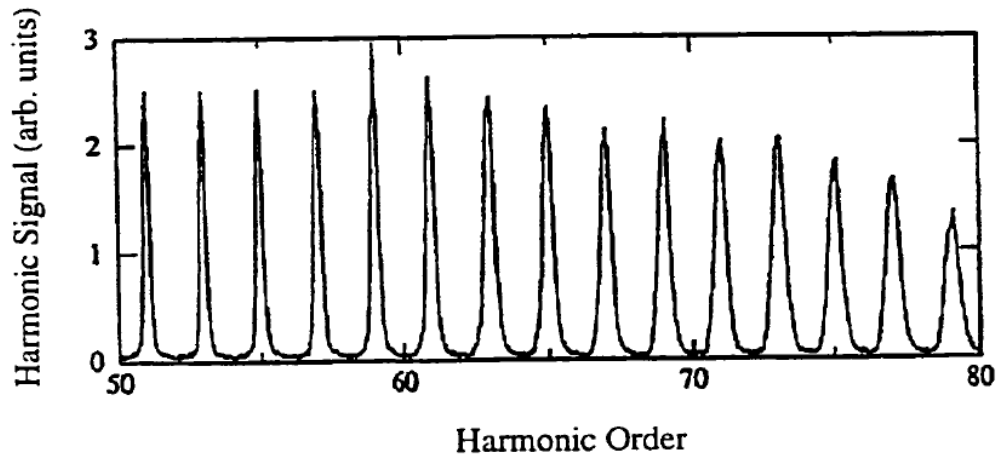


**Figure 1.3** Harmonic spectrum produced in 13 torr of Ne by 806 nm high intensity laser. Harmonic number 65 would correspond to a wavelength of 12.4 nm. Figure is adapted from Macklin *et al.* [5].

### 1.1.3 Plasma sources

EUV and soft x-ray sources contain information about their physical plasma state. The physics of plasmas involves interaction between many charged particles on a microscopic scale through the electric and magnetic fields associated with their positions and velocities. Fortunately, by consideration of macroscopic, collective interactions where the charges are described in terms of charge densities and currents may simplify this extremely complex many body problem. In general the radiation consists of a broad spectral continuum, plus narrow line emission from the various ionization stages of those elements present. The process in which radiation is emitted from plasmas consists of three main types called free-free, bound-free and bound-bound. The free-free process is often called bremsstrahlung radiation. Such radiation is due to the interaction of free electrons as they collide and undergo changes in acceleration which gives rise to the release of radiative energy via photons. This process produces a continuous or broadband spectrum since radiation can be procured at all wavelengths. In

contrast the free-bound spectrum process involves the capture of a free electron by an ion whereby the energy gained is given off by the release of a photon. This also produces a continuous spectrum due to the just mentioned continuous range of electron energies. This process is also referred to as recombination radiation.

In plasma the bound-bound radiative process involves the specific electronic transition in an ion between two states bound to the nucleus of the ion. The energy level structure of the ion, just as in neutral atoms, is composed of discrete states which are described by quantum mechanical wavefunctions characterized by principal, orbital and spin quantum numbers. The states are arranged in energy according to these quantum numbers. However the binding energy between the charged nucleus and remaining electrons of an ion is larger than that of a neutral atom due to the additional net charge on the nucleus. This causes the energy level separation of states to be higher in the ion. When an electron makes a transition from an upper energy states to a lower energy states a photon is emitted with exactly the energy of the separation of the states. In ions this energy level separation can correspond to the photon energies extending into the EUV and soft x-ray wavelength regions. Thus bound-bound radiation gives rise to so-called line radiation since the emitted wavelength is discrete. In addition the frequency spread or linewidth of the radiation can be quite narrow due the specific characteristics of the transition. Such emission is termed narrowband. In some ions the energy level structure has many closely-spaced levels. When emission occurs from each of these closely-spaced levels the wavelengths are very similar and tend to overlap each other creating a quasi-continuous spectrum. Hence plasma sources in general are comprised of continuous radiation and line radiation at specific wavelengths.

The actual emission spectrum of plasma is solely determined by the state of plasma and, of course, the components or ionic species contained in the plasma. The state of the plasma can be defined in general by two fundamental parameters,

temperature and density. In collisionally dominated plasma (common to laboratory plasmas) each of the constituent particles, i.e. the ions and electrons, will tend to form a Maxwellian distribution of velocities due to equipartition of energy through collision with each other [7]. The only parameter that defines this distribution is the temperature such that the plasma may be described as having an electron temperature and an ion temperature,  $T_e$  and  $T_i$ , respectively. Hence the temperature describes the kinetic and/or thermal energy of the electrons and ions. Furthermore due to plasma neutrality the corresponding electron density and ion density in the plasma are related by,  $n_e = \sum_i Z_i n_i$ , where  $n_e$  is the electron density,  $n_i$  is the ion density of species  $i$ , and  $Z_i$  is the charge state of species  $i$ .

The consequence of describing the plasma by its temperature and density is quite far reaching. However for the purposes here describing short wavelength radiation from plasmas, a few general comments can be made to illustrate some qualitative issues. Considering weakly ionized plasma the effect of increasing the electron temperature by some means generally causes a shift to higher ionization levels through collisional ionization. Thus the spectrum of radiation would then originate from higher ion stages or states thereby accessing more energetic transitions and producing shorter wavelengths. The effect of increasing electron density for a given ion density increases the charge state by the above neutrality relation. It also goes directly to creating increased populations of excited levels that are capable of radiating thereby increasing the amount of radiation emitted.

The following sub-sections describe the techniques for generating plasmas in order to produce EUV and soft x-ray radiation. These are laser-produced plasma sources and capillary discharge plasma sources.

### 1.1.3.1. Laser-produced plasma sources

The laser-produced plasma has been extensively studied as a mean of producing short wavelength radiation [8]. The laser plasma is created by focusing an intense pulsed laser on a target made of heavy element such as tungsten, tin, etc. The schematic diagram of laser-produced plasma is shown in Fig. 1.4. The laser radiation is absorbed by the material and quickly forms plasma of dense highly ionized material due to the heating caused by the absorption of laser radiation. The heating causes the plasma to become increasingly ionized thus creating highly charged ions with many electrons removed. Intense x-ray and EUV emission is produced in the form of line and broadband continuum radiation. An approximation to the emission spectrum of a laser-produced plasma can be made by considering the plasma to be a blackbody radiator at some temperature. This ignores the characteristic line radiation, which can be very significant, but serves to illustrate the general emission character. The blackbody approximation to laser-produced plasma at an electron temperature of 177 eV is shown in Fig. 1.5.

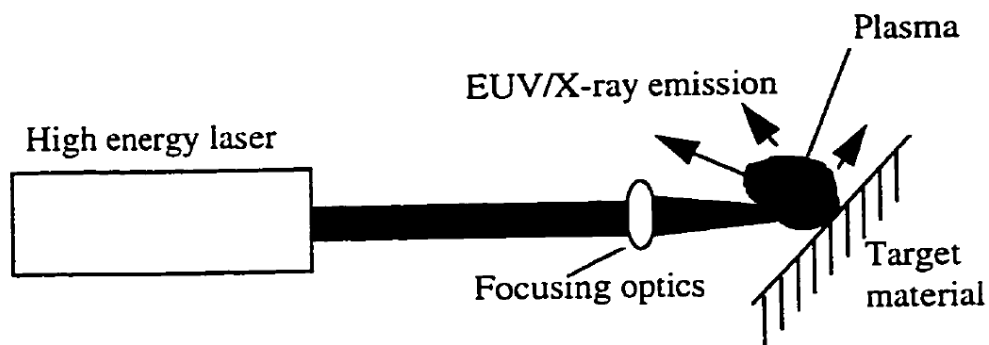


**Figure 1.4** Schematic diagram of a laser-produced plasma.

Fig. 1.5 is an adaptation of a useful diagram conceived by Ceglio [9] in which different EUV and soft x-ray sources may be compared with respect to their individual brightness defined by the quantity (photons/ (sec mm<sup>2</sup> mrad<sup>2</sup> .01% bandwidth)). A word of caution is needed here in interpreting this figure. A judicious definition of spectral

brightness may tend to place one type of source above the other and make it appear more intense and thus give the connotation of being better. In this case short duration narrow band sources such as laser-produced plasmas (considering line radiation) are favored by the definition mentioned above. As the remaining types of sources are discussed and related to this figure it is important to consider that it is only a relative comparison. In fact as the sources are discussed it will become evident that different sources are suited to different tasks and therefore should only be absolutely compared in terms of analyzing each source in its competitiveness for a specific use or application.

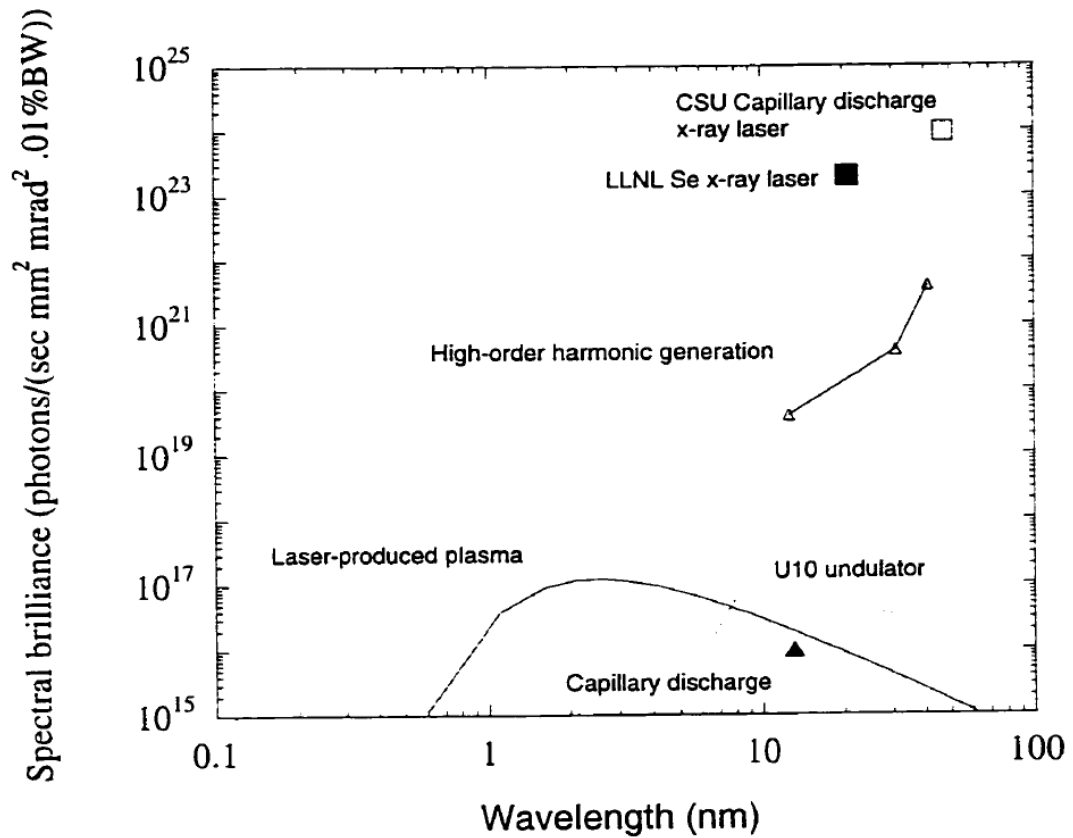


**Figure 1.5** Comparison of relative brightness of difference types of EUV and soft x-ray sources. Where markers are shown, these represent nominal values for the indicated wavelength. This figure is adapted from Reference [9] and a comparison of other sources with relatively lower brightness can be found therein.

### 1.1.3.2. Capillary discharge plasma sources

Another example of a plasma source is the capillary-discharge shown on Figure 1.6. The plasma in a capillary discharge is confined inside a small bore or capillary a few mm in diameter. The plasma is generated by the electrical breakdown of the evacuated insulating capillary itself or by the electrical breakdown of a gas or other vapor contained within the bore. These plasmas are excited by high current pulses and can generate intense continuous spectra as well as line radiation. More details will be described in the next chapter.

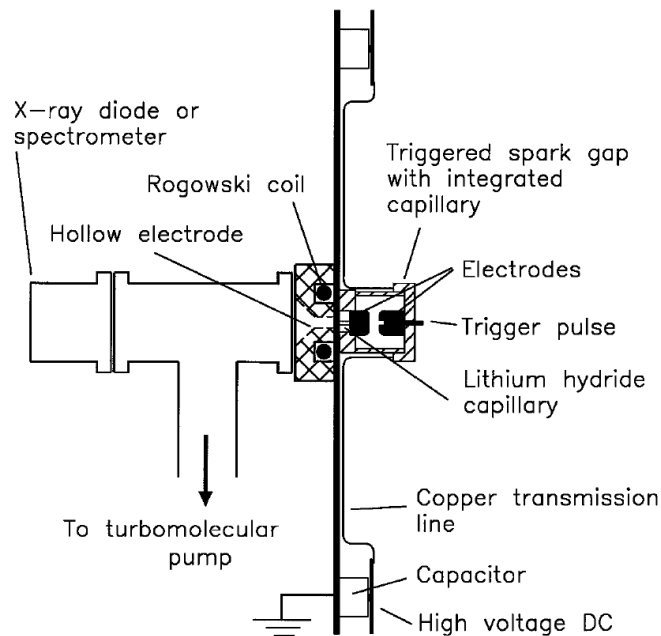


**Figure 1.6** Schematic diagram of the LiH capillary-discharge setup. Figure is adapted from reference [10].

## 1.2 X-ray laser sources

X-ray lasers are a subset of plasma sources since they utilize plasmas as the active medium by which amplification of the radiation occurs. These sources are the major subject of this work, thus they are only addressed here to describe how they fit in with the other sources being compared and discussed. They are the brightest sources available at their unique concentration of light into a small directed beam of very

narrow linewidth. They are coherent sources as well, making them suitable for special applications such as interferometry and holography. The Neon-like Argon ( $\text{Ar}^{8+}$ ) laser at 46.9 nm was demonstrated in 1994 by Rocca, *et al.* [11] at Colorado State University using plasma produced in a capillary by an electrical discharge. Chapter 2 will give a more detailed introduction and overview of x-ray lasers and lay the groundwork for the investigations in x-ray laser plasma dynamics studied for this thesis.

### 1.3 Applications of Short Wavelength Radiation

Much of the advancements in short wavelength radiation sources have been due to the demand for such in certain applications. One very important application mentioned earlier is extreme ultraviolet lithography. As integrated circuits become more complex they must pack more features into essentially the same amount of physical space. Typically this has been done by reducing the wavelength in optical lithography in order to increase the resolution and produce finer and finer features. However as the features continue to shrink below 0.1  $\mu\text{m}$ , optical lithography will cease to provide the needed resolution. Thus the use of EUV radiation has come to the forefront as the source necessary to carry on the technology past the 0.1  $\mu\text{m}$  limit. Much effort has gone into developing laser plasma and capillary discharge sources due to their demand for use in EUV lithography [12, 13].

X-ray microscopy has become an important tool in the ever-increasing need for imaging equipment in the biological and nano-structure fields. These microscopes use laser plasma sources as well as synchrotron sources for a variety of demanding high resolution imaging needs [14].

In general short wavelength sources tend to be somewhat large and expensive. Synchrotron sources tend to be the costliest and most complex of the short wavelength sources due to the overheads associated with the electron storage ring. Laser plasma and



harmonic generation sources usually require expensive high energy lasers drive. Electrical discharge sources are probably the least complicated and can be made very compact. Due to the demands of the applications mentioned above there is a need to reduce the size and cost in order to make these sources more practical. For instance in EUV lithography the capillary discharge requires much less space and costs significantly less than a comparable source utilizing laser-produced plasma. An EUV microscope may also one day be constructed utilizing a capillary discharge source which would be no larger than present day scanning electron microscopes.

Application driven development is a strong force behind the technology of short wavelength sources. These sources will therefore evolve in directions dictated by the specific areas. For instance the capillary discharge with its small footprint and high average power could be applied to microscopy and lithography. High harmonic generation with its high peak power and coherence properties will probably find use in studies of dynamics systems, such as pump-probe diagnostics. X-ray lasers are already being used as tools to do interferometry of high density plasmas in support of fusion research and are just beginning to find applications in chemical research as well. In addition, the scaling down in size of sources makes them more accessible to small scale laboratories which will in turn lead to the development and realization of more applications.

#### **1.4 Overview of X-ray Lasers**

X-ray lasers have been briefly introduced in the context of comparing the different types of short wavelength radiation sources. A more general overview will now be given to introduce some of the specific types of x-ray lasers not already mentioned and describe past and current efforts to achieve lasing in the EUV and soft x-ray regions. To date all successful x-ray lasers have operated in plasmas. There are two

main reasons behind this fact. Firstly, it has already been mentioned that x-ray transitions arise from the electronic transitions in highly charged ions. Thus a plasma is directly suited to providing ionized species for which x-ray radiation may be produced. The second reason is that plasmas can generally satisfy the requirements and provide the appropriate conditions for producing a laser medium at short wavelengths. This is by no means inevitable since the requirements are quite stringent, but plasmas can provide the right conditions under the right circumstances. The details of the latter are the major focus of this work and will be developed in the following chapters.

Until recently most x-ray lasers were produced in laser-produced plasmas using very high energy large driver systems. The lasers used to produce the plasmas had pulse energies in the few hundred of joule range or more and generally occupied large facilities. It is not surprising that with such high energy lasers the plasmas generated were very high temperature plasmas composed of highly stripped ions. This was the case for the first x-ray laser in 24x ionized Se. Since the first x-ray laser, many more lasers have been demonstrated in highly ionized plasmas. In fact there exist particular types of ions that have been most successful for producing lasers. For instance  $\text{Se}^{24+}$  has the same number of remaining electrons as does neutral Neon, hence it is termed a Ne-like ion. Another example would be  $\text{C}^{5+}$  which has only one remaining electron and therefore is similar to hydrogen and is termed a H-like ion. The electronic configuration of these ions then is similar to their neutral counterpart. It has been found that by scaling a known laser transition in a neutral species to the similar transition in the neutral-like ion there exists a good chance of creating a laser. This is the basis of isoelectronic scaling and it will be discussed in detail in Section 2.3 of Chapter 2. With that in mind the Hydrogen-like, Neon-like, and also the Nickel-like ions have been found to be successful ion species to create x-ray lasers.

To date, EUV and soft x-ray lasers have been observed from nearly 70 nm down to 3.6 nm. Table 1.1 shows a sample list of some of the observed x-ray lasers [15]. Note that in some cases lasing occurs at multiple wavelengths.

**Table 1.1** Examples of observed x-ray lasers. This is adapted from reference [15].

Ne-like ionic species	Lasing wavelength (nm)	Ni-like ionic species	Lasing wavelength (nm)
Y <sup>29+</sup>	15.5	Au <sup>54+</sup>	3.56
Sr <sup>28+</sup>	16.41; 16.65	W <sup>46+</sup>	4.31
Se <sup>24+</sup>	20.64; 20.98	Ta <sup>45+</sup>	4.48
Ge <sup>22+</sup>	23.22; 23.63	Eu <sup>35+</sup>	6.58
Ar <sup>8+</sup>	46.88	Yb <sup>42+</sup>	8.11

Recent advances in capillary discharge x-ray lasers and small scale high energy lasers have formed a new class of x-ray lasers based on the “table-top” concept. Thus instead of large driver systems, x-ray lasers can now be built and developed in smaller laboratory environments. In the case of capillary discharge the electrical driver systems are quite modest in size and can even be made quite compact [16] such that a capillary discharge x-ray laser can effectively fit on a table-top. High-power, ultrashort pulse lasers or so called table-top terawatt lasers are also being investigated as the driver for x-ray lasers as well. The latter is especially suited to the optical-field ionized x-ray laser which is a special class of x-ray laser based on a highly non-equilibrium plasma.

## 1.5 Thesis Overview

The objective of this research is to study the dynamics of the plasma in a capillary-discharge of soft x-ray lasers through magneto-hydrodynamic (MHD) modelling. Throughout the end of the research, qualitative trends in the kinetics of ions and the design of Z-pinch will be suggested.

This introduction has illustrated the types of sources available in the EUV and soft x-ray regions and briefly discussed the technologies behind each source. Particular emphasis has been placed on x-ray lasers, which is the topic of this thesis.

In Chapter 2 some basic concepts of the laser will be developed and then extended to x-ray lasers. This is followed by a discussion of two of the main methods to produce x-ray lasers in plasmas, i.e., recombination pumping and collisional pumping. A discussion of the theory behind the capillary-discharge x-ray laser will be given since it provides the basis for simulation investigation for this type of x-ray laser. In addition background theory will be described for modelling of a capillary-discharge soft x-ray laser.

Chapter 3 describes a numerical study of a collisional excitation pumping of capillary discharge neon-like argon soft x-ray laser based on Helios-CR [17] simulation. Through this study, in Chapter 4, the optimization of gain for specific configurations [18] can be estimated.

However, the electron density profile will also bend the ray and its will influence the output intensity of laser. Due to this, Chapter 5 describes the modelling of a capillary discharge soft x-ray out intensity based on the ray tracing code.

In chapter 6, the feasibility of a nitrogen-recombination soft x-ray laser using capillary discharge Z-pinch has been examined in order to search for shorter wavelength to enable for the technology.

Finally, Chapter 7 summarizes the work and gives concluding remarks on the relevance of the work presented with respect to the field of x-ray lasers.

## Chapter 2

### Theoretical Background

#### 2.1 Introduction

The main focus of the work presented in this thesis is the analysis and description of the plasma dynamics associated with the operation of x-ray lasers. In this chapter the basic framework will be developed for the investigations undertaken in two different types of x-ray lasers.

To begin, the general concepts of fundamental laser theory will be given and then extended to x-ray lasers. Once the basics have been established the specific scheme of collisionally excited x-ray lasers will be introduced. This will provide the basis for the detailed modelling of such lasers in Chapter 3. Next both x-ray pumping schemes will be described since it forms the background for operation of the capillary discharge driven x-ray laser. In addition, plasma concepts necessary to understand the capillary discharge-driven x-ray laser will be given. These concepts introduce the key plasma conditions and parameters that are crucial to successful x-ray laser operation. The final section of this chapter will provide the theory behind plasmas to establish the key parameters in the plasma dynamics relevant to the capillary discharge driven x-ray laser.

#### 2.2 Fundamental Laser Theory

The term "laser" is defined as *Light Amplification by Stimulated Emission of Radiation* [19]. Laser operates on the principle of amplification (i.e., the gain in intensity of a photon beam as it passes through atoms in a medium such as solid or gas.) This amplification occurs due to stimulated emission which is the photon-induced radiative decay of an atomic transition. To help illustrate the concept of gain, consider a simple two-level atomic system consisting an upper energy level or state,  $u$ , and a lower

energy level,  $l$ , with the corresponding energy separation  $\Delta E_{ul} = E_u - E_l > 0$ . The lasing transition is between these two levels and has a wavelength  $\lambda_{ul}$ . Fig. 2.1 shows an elongated column consisting of the two-level atoms representing a gain medium of amplifier length  $z$  that supports lasing, it grows exponentially over the length  $L$ . Then, as it reaches the saturation intensity  $I(L)$  or  $I_{sat}$ , it no longer grows at that rate. It then begins to extract most of energy from the medium to the right of  $L$  and grows at an approximately linear rate over the remaining length  $Y$ . The intensity of the laser beam grows exponentially from some initial value  $I_0$  as it traverses a distance  $z$  along the medium according to the equation,

$$I(z) = I_0 e^{g(\nu)z}, \quad (2.1)$$

where  $g(\nu)$  is the frequency dependent gain coefficient and has dimensions of inverse of the length and is usually expressed in  $\text{cm}^{-1}$ . The gain coefficient is further defined according to [15],

$$g(\nu) = \sigma_{ul}(\nu) \left( N_u - \frac{g_u}{g_l} N_l \right), \quad (2.2)$$

where  $\sigma_{ul}$  is the stimulated emission cross section for the transition from the upper laser level,  $u$ , to the lower laser level,  $l$  and  $N_u$  and  $N_l$  are the population densities of the upper laser level,  $u$ , to the lower laser level,  $l$ . For exponential growth it is clear that  $g(\nu) > 0$  or

$$\frac{N_u}{N_l} \left( \frac{g_l}{g_u} \right) > 1. \quad (2.3)$$

Eq. (2.3) describes the necessary condition for a laser that a population inversion must exist. That is, the population density (number per unit volume) of the upper level,  $N_u$ , must be larger than the lower level  $N_l$  times the statistical weight ratio  $g_u/g_l$  for the upper and lower levels.

In a collection of atoms in thermodynamic equilibrium at a temperature  $T$  the population of the levels is governed by the Boltzmann distribution of  $N_u/N_l = g_u/g_l e^{-\Delta E/kT}$  where  $k$  is Boltzmann constant. This clearly does not fulfill the necessary requirement of a population inversion since the ratio  $N_u/N_l$  is always less than the unity. Thus the population inversion must be created by “pumping” which is general term used to describe a variety of processes that can promote population to the upper energy level. Pumping will be described in more detail after some discussion of the stimulated emission cross section.

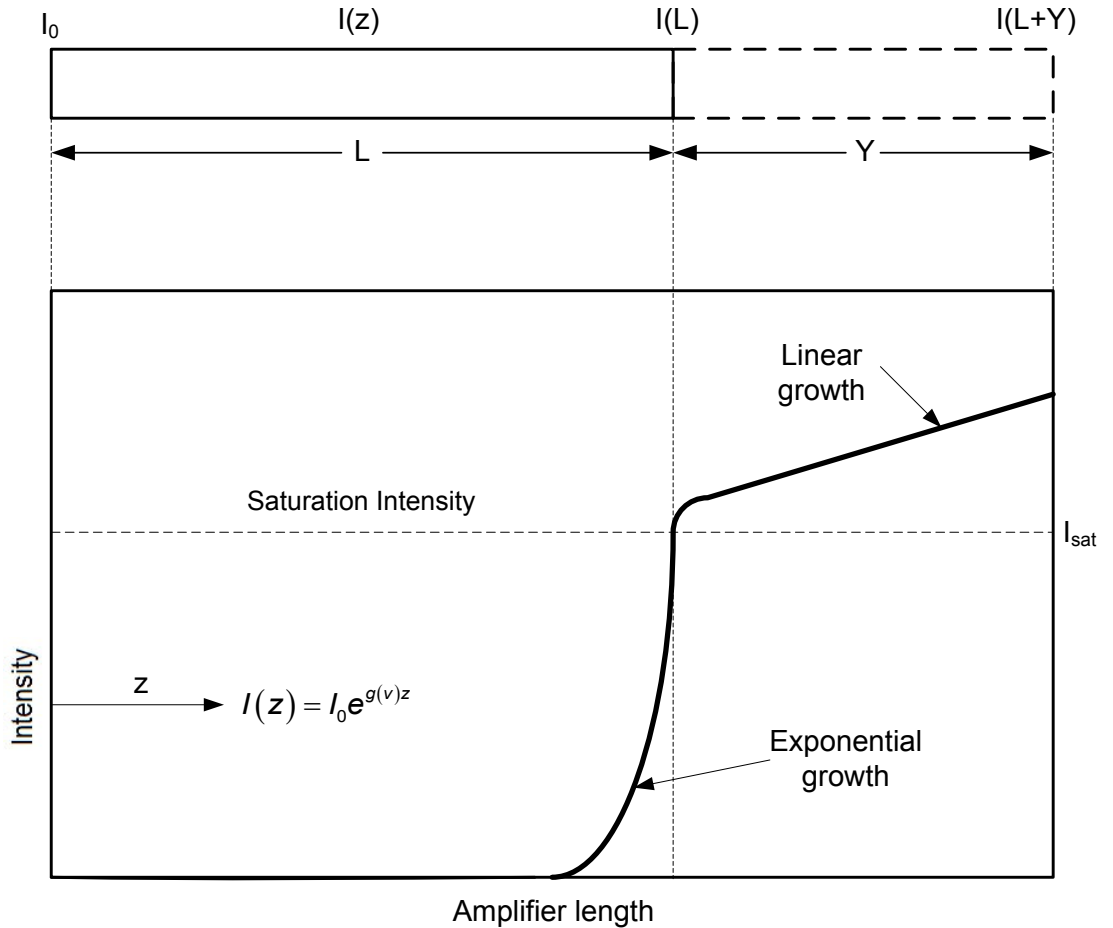


**Figure 2.1** Schematic diagram of a gain medium that supports lasing

The lasing transition is characterized by the stimulated emission cross section which has a dimension of area and measured in units of  $\text{cm}^2$ . This cross section

describes the probability of a stimulated emission event occurring on that transition. The actual form of the stimulated emission cross section depends on the type of emission broadening that occurs for the radiation. In gas lasers the broadening is typically dominated by Doppler effects caused by the thermal motion of the ions and leads to Gaussian lineshape profile for the cross section. The stimulated emission cross section at the center of the Gaussian frequency spread for Doppler broadening is given by [19],

$$\sigma_{ul} = \frac{\lambda_{ul}^3}{8\pi} A_{ul} \sqrt{\left(\frac{M}{2\pi kT}\right)}, \quad (2.4)$$

where  $M$  is the mass of the ion,  $T$  is the ion temperature, and  $A_{ul}$  is the spontaneous transition probability. Other broadening mechanisms lead to similar expressions for the stimulated emission cross section.

The two-level atomic system used for the above description does not include sufficient levels to describe the concept of pumping of the upper laser level and the creation of a population inversion. Thus the three-level laser system shown in Fig. 2.2 will now be used. It will be shown later that this system is also directly relevant to specific x-ray laser level models. The three atomic energy level or states are spaced according to their energy separation such that the upper level is at  $E_u$ , the lower level is at  $E_l$  and the lowest lying energy level,  $0$  (which could be a ground state), is at  $E_0$ . The upper and lower levels are subject to natural relaxation or decay processes to the next lower lying level. The upper and lower states may radiatively decay by spontaneous emission or they may also decay non-radiatively by collisions with other atoms. These decay processes shown in Fig. 2.2 and collectively labeled as  $\gamma$  for each of the downward pathways. Pumping to the upper energy level from the state  $0$  is accomplished through either collisional processes or absorption of radiation and is indicated by the rate  $\Gamma_{0u}$ . Pumping can also occur to the lower level via these same processes and is described by the rate  $\Gamma_{0l}$ .



The rate of change of population in the upper and lower levels can be described by a set of rate equations [19]. For the steady state case the equations can be set equal to zero and are given by,

$$\begin{aligned}\frac{dN_u}{dt} &= N_0\Gamma_{0u} - N_u(\gamma_{ul} + \gamma_{u0}) = 0 \\ \frac{dN_l}{dt} &= N_0\Gamma_{0l} + N_u\gamma_{ul} - N_l\gamma_{l0} = 0.\end{aligned}\tag{2.5}$$

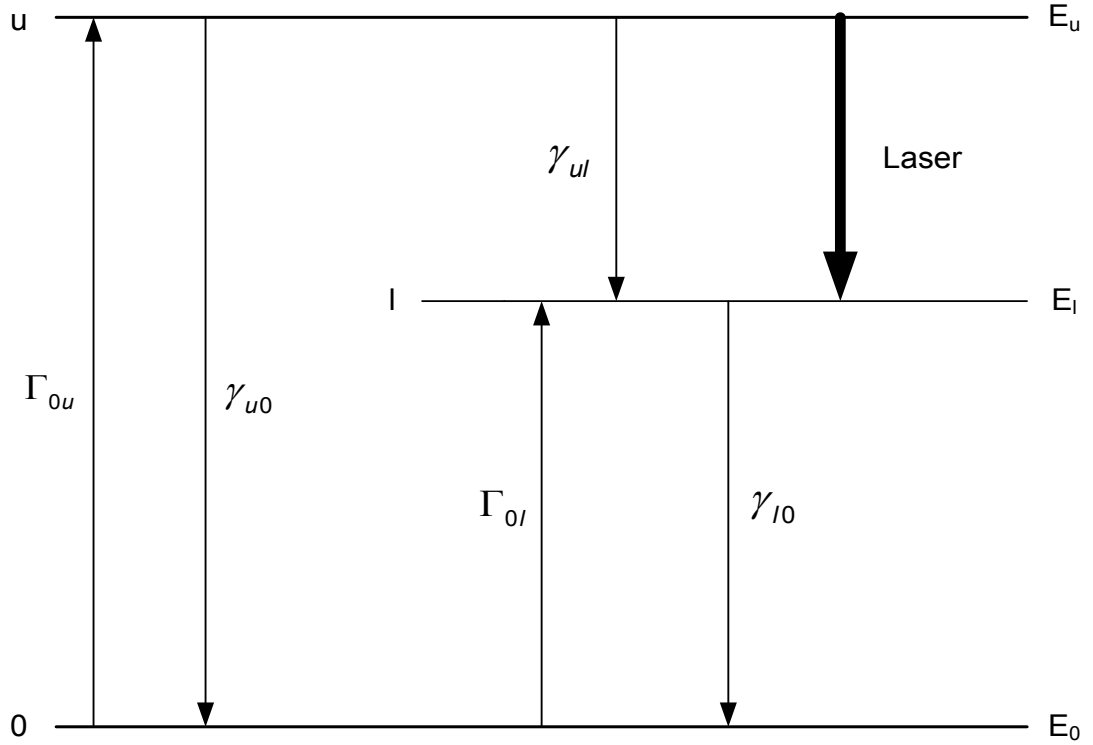


**Figure 2.2** Energy-level diagram and relevant excitation and decay processes of an atomic three-level system.

The ratio of the population upper state to the lower state is determined from these equations. It is often the case in atomic systems that the decay rate is purely radiative; therefore it is possible to set  $\gamma = A$  for each of the downward pathways. In addition when  $A_{l0}$  is large,  $A_{u0}$  is usually small due to consideration of the energy level separation. Thus solving Eq. (2.5) under these conditions yields the following for the ratio of the upper and lower population levels,

$$\frac{N_u}{N_l} \equiv \frac{1}{(1 + \Gamma_{0l}/\Gamma_{0u})} \frac{A_{l0}}{A_{ul}}. \quad (2.6)$$

In order for a population inversion to exist in steady state, the ratios of the pumping and the radiative decay must be such that Eq. (2.6) is greater than unity. More importantly, Eq. (2.6) indicates that it is better to have a very fast decay out of the lower level and a fast pumping to the upper level as compared to the lower level. It should also be noted that the population inversion will only last so long as the pumping is applied. In the case where the pumping is only on for a period of time greater than the lifetime of the upper level,  $1/A_{ul}$ , but not continuous, the operation of the laser is termed quasi-steady state. This is an important concept in x-ray lasers.

In addition to the steady state operation just described, the three-level system can be used to illustrate the transient inversion scheme. In this case it is assumed that there is no decay out of lower laser level. Thus the laser is said to be self terminating. This will also be of important to a specific x-ray laser pumping scheme to be discussed later. Eqn (2.5) cannot be set to zero since the time dependence is of interest in this case. To further simplify the equations,  $\gamma_{u0}$  is assumed to be negligible on the time scales of interest and thus the upper level decay time is simply  $\tau = 1/A_{ul}$ . Silfvast [19] shows that under these conditions the ratio of the upper level to the lower level is given by,

$$\frac{N_u}{N_l} = \frac{1 - e^{-t/\tau}}{\left[ \left( \frac{\Gamma_{0l}}{\Gamma_{0u}} \right) + 1 \right] \frac{t}{\tau} - (1 - e^{-t/\tau})}. \quad (2.7)$$

The maximum duration the inversion will last (and hence the gain) is given by setting  $\Gamma_{0l} = 0$  and solving for  $\tau$  with  $N_u/N_l = 1$ . This yields a value of  $\tau = 1.6/A_{ul}$ . Thus the transient pumped laser can be characterized by a short gain duration depending upon the exact value of the spontaneous decay rate of the upper energy level.

### 2.3 Specific Concepts in X-ray Lasing

The basic concepts and fundamental relations just described apply to lasers in general, whether x-ray, visible or infrared. However the fundamental parameters that define lasing, such as the stimulated emission cross section and gain, are somewhat different for x-ray lasers. In addition, the pumping requirements for x-ray lasers are significantly more demanding than for other lasers operating at longer wavelengths. This is mainly due to the nature of the highly energetic energy levels involved in the x-ray laser transitions. The concepts specific to x-ray lasers will now be addressed by examining some scaling relations.

In order to access x-ray transitions it is necessary to strip electrons from atoms and create highly ionized species. This is one reason why plasmas are an ideal medium to create x-ray lasers. As an example consider a lasing transition between two bound levels with principal quantum numbers  $n_1 = 3$  and  $n_2 = 2$  in a H-like ion. The energy level separation is given by  $\Delta E_{n_1 n_2} = -13.6Z^2 (1/n_2^2 - 1/n_1^2)$  (in eV) where  $Z$  is nuclear charge. In H-like  $B^{4+}$  ( $Z = 5$ ), for example, the  $n_1 = 3$  to  $n_2 = 2$  transition has an energy separation of 47 eV which corresponds to an x-ray wavelength of 26.3 nm. Likewise H-like Carbon ( $Z = 6$ ) has a wavelength of 18.2 nm for the same transition. This type of scaling of wavelength with  $Z$  for a given transition in an ion with a neutral-like electronic configuration is termed isoelectronic scaling. Hydrogen was used here as a simple example for which the energy separation is easily calculated, but isoelectronic scaling applies to other ion species as well even if the  $Z^2$  scaling is not maintained. For instance  $Se^{24+}$  has essentially the same relative energy level structure as neutral Ne. Isoelectronic scaling is most useful in utilizing known lasing transitions in neutral atoms and then proceeding along the same electronic configuration in highly charged ions to identify possible lasing transitions at short wavelengths.

In H-like ions the spontaneous transition probability scales as  $Z^4 A_{ul}^H$  where  $A_{ul}^H$  is the probability for the same transition in hydrogen. The lifetime of the upper level is given by the inverse of the spontaneous transition probability or  $(Z^4 A_{ul}^H)^{-1}$ . This illustrates that for H-like ions upper level lifetimes scale as  $1/Z^4$ ; thus the lifetimes decrease rapidly for increasing nuclear charge of the ion. (In the special case of the transient inversion laser mentioned in Section 2.2 the gain duration lasts only on the order of this lifetime and this effectively restricts the lengths of x-ray laser gas mediums unless traveling wave excitation is used). Typical upper level lifetimes in the x-ray region are picoseconds to femtoseconds. This reduction in lifetime duration also applies in general to non H-like ions, but the same scaling cannot be used.

The stimulated emission cross section generally decreases with wavelength as can be seen for the case of Doppler broadening in Eq. (2.4). However there is an implicit wavelength dependence on  $A_{ul}$  that should be included before continuing with a scaling relation. The spontaneous transition rate can be expressed in terms of the oscillator strength for the transition,  $f_{ul}$ , charge of the electron,  $e$ , the permittivity of a vacuum,  $\epsilon_0$ , the mass of electron,  $m_e$  and speed of light,  $c$ , which is fairly constant for a given transition along isoelectronic sequences [15]. Thus  $A_{ul}$  can be written as [19],

$$A_{ul} = \frac{2\pi e^2 f_{ul}}{\epsilon_0 m_e c (g_u/g_l) \lambda_{ul}^2}. \quad (2.8)$$

The stimulated emission cross section follows from substitution of Eq. (2.8) into (2.4) which gives,

$$\sigma_{ul} = \frac{\lambda_{ul}}{8\pi} \left( \frac{2\pi e^2 f_{lu}}{\epsilon_0 m_e c (g_u/g_l)} \right) \sqrt{\left( \frac{M}{2\pi kT} \right)}, \quad (2.9)$$

where the wavelength dependence is explicitly seen to be not as strong but still decreases significantly at shorter wavelength. One might conclude that the gain would

also decrease, however this is generally not the case with x-ray lasers. In fact x-ray lasers usually exhibit high gain values with decreasing wavelength.

The basis of increasing gain with decreasing wavelength is that the reduction in stimulated emission cross section is compensated by the ability to produce a much higher inversion density at shorter wavelengths [19]. This is where pumping becomes very important in producing the large upper level state level densities. To see how much high densities are achieved, consider a collisional mixing argument based on the specific case of electron collisional excitation. (This concept will be discussed in greater detail in Sec 2.3.2). In plasmas composed of free electrons and ions, collisions occur frequently. In the case of electron-electron collisions, the number of collisions per unit time depends on the temperature and density of the electrons in the plasma. The electron collisions can cause both excitation and de-excitation of levels. If the collisional de-excitation rate of the upper level approaches that radiative decay rate out of the lower level the population inversion will begin to be destroyed. This effectively places an upper limit on the electron density in the plasma and still be able to support a population inversion. This maximum electron density is readily calculated [15] and is given by,

$$n_e^{\max} = \frac{5.1 \times 10^{24}}{\lambda_{ul}^3} \frac{A_{l0}}{A_{ul}} \frac{(kT_e)^{1/2}}{\langle G_{ul} \rangle} \quad (\text{cm}^{-3}), \quad (2.10)$$

where  $\lambda_{ul}$  must be given in Angstroms,  $kT_e$  is the electron temperature in eV, and  $\langle G_{ul} \rangle$  is the Gaunt correction factor that originates from the collisional rate and usually has a value between 0.1-1 [15]. Most lasers, lasing from visible to x-ray wavelengths, operate very close to this maximum electron density [19]. Since in a plasma the relation between ion density and electron density is  $n_e = \sum_i Z_i n_i$ , then it could be expected that the ion density, and hence the upper laser level density, would scale in the same manner since  $N_u \propto N_0$ . Therefore considering Eq. (2.9) and (2.2) the gain coefficient would

scale as  $\sim 1/\lambda^2$ . Hence the gain can increase with decreasing wavelength if sufficient pumping is available. The scaling done here does not apply to every type of pumping mechanism possible; however it does illustrate the general trend seen with many pumping methods in x-ray lasers [19].

Values for the gain coefficient  $g$  in x-ray lasers can range from 1 to hundreds in units of  $\text{cm}^{-1}$ . Thus it is seen that even short gain lengths can produce considerable  $gL$  products and hence large amplification.

However, there are two conditions which lead to gain reduction and extinction and they can become important in x-ray lasers just as in longer wavelength lasers. The first condition is collisional mixing which has just been described above and led to the relationship in Eq. (2.10). Exceeding the maximum electron density causes destruction of population inversion and hence reduction of the gain. The second condition is radiation trapping which reduces the decay rate of the lower state level due to the immediate reabsorption of a photon emitted from the lower state level to level  $0$ , thus re-exciting level  $l$ . This trapping is dependent on the ground state density  $N_0$ . Silfvast [19] shows that radiation trapping begins to increase  $N_l$  when the value of  $\sigma_{0l}N_0b$  becomes greater than 1.46 where  $b$  is the radius of the gain medium.

Another consequence of the limited gain duration is that x-ray lasers mainly operate in a mode termed as amplified spontaneous emission. This is stimulated emission without feedback as in an optical laser with an external high reflecting cavity surrounding the active medium. With short gain duration one must consider the light propagation time that limits the distance that mirrors can be placed relative to the ends of the medium and the number of passes allowed. Some experiments have been attempted with a single mirror that allow double pass amplification, however the plasma environments associated with x-ray lasers and the close proximity of the mirrors cause rapid degradation of the mirror reflectivity, if not catastrophic damage [15].

Production of the population inversion is critical to achieving lasing action. Populating the upper state level by pumping is a crucial and often quite sensitive mechanism. The two main processes for pumping x-ray lasers are recombination and collisional excitation. They are both atomic processes that involve electron interaction with ions and thus the plasma conditions fundamentally determine the effectiveness of the pumping and overall achievement of gain. Since these two processes are distinct and form the foundation for the work in this thesis, they are treated in detail in the following sections.

### 2.3.1 Recombination pumping

Recombination pumping is a method by which the upper laser level is populated by processes which begin with capture or recombination of continuum electrons with ions. Continuum electrons are free electrons of continuous energy distribution existing in the plasma. The two forms of recombination process are termed three-body recombination and radiative recombination. Three-body recombination requires the interaction of an ion and two free electrons. The ion combines with a free electron establishing a new ion (in an excited state) with one less charge (or formation of a neutral atom) and imparting the excess energy to the secondary electron. By contrast, radiative recombination involves the capture of a free electron by an ion with excess energy given off via emission of a photon [19].

The multiple steps involved in recombination pumping are illustrated in Fig. 2.3 where an energy level diagram is shown composed of the ground state of an ion  $A^{i+}$  (with excited levels  $p$ ) and the ground state of the next higher ion stage  $A^{(i+1)+}$ . The first step in recombination pumping is to produce an abundant population of  $A^{(i+1)+}$  ions in the ground state. This condition can generally be accomplished by some form of ionization of the plasma, electron-collisional or otherwise, that produces this ion stage.

Note that ionization also serves the purpose of producing free electrons which contribute to the three-body recombination process. At this point it is assumed that the plasma has a temperature given by  $T_e$ . The next step is the actual recombination of the electrons with the  $A^{(i+1)+}$  ions to form the next lower ion stage. The three body recombination process favors populating the upper lying levels in contrast to radiative recombination which favors the lower lying levels. This will be seen more clearly when the actual functional form of the rates is given. In collisional recombination, collisional mixing of the upper levels occurs on a very rapid timescale due to the small energy separation of the levels and quickly distributes population amongst the levels  $N_p$  according to the Saha equation [20],

$$N_p^{i+} = n_e N_0^{(i+1)+} p^2 \left( \frac{h^2}{2\pi m_e k T_e} \right)^{\frac{3}{2}} e^{\frac{-E_p}{k T_e}}, \quad (2.11)$$

where  $E_p$  is the ionization potential of any level  $p$  and  $h$  is the Planck constant. The third step is the critical part of recombination pumping and involves the cooling of the plasma. As the plasma cools the population in the upper levels decreases according to Eq. (2.11). Since the energy spacing between levels increase toward the lower lying levels there will be a level such that, with cooling, the collisional process becomes negligible compared to radiative decay from that level. Since population is still moving into the upper level, but not being depleted due to collisional processes, and the lower level is emptying due to radiative decay, a population inversion can be achieved which then leads to lasing between the upper and lower level as shown in Fig. 2.3.



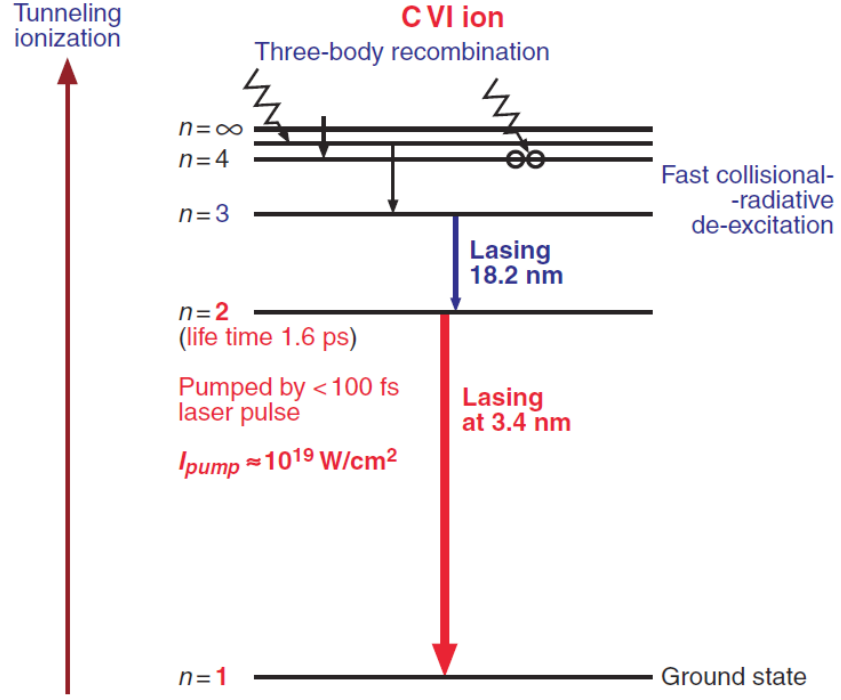


**Figure 2.3** Recombination scheme for C VI ion. Figure taken from reference [21].

Recombination processes such as three body recombination can be defined by rates that are useful for quantifying the downward movement of population in levels according to simple rate equations. The rate,  $R$ , of a process is found by averaging the product of the cross section for the process and the velocity of the interaction particles over a velocity distribution, usually Maxwellian. This is written as  $R = \langle \sigma(v)v \rangle$ . The cross section  $\sigma$  is generally found by quantum mechanical scattering calculations taking into account the initial and final wavefunctions of the interacting particles. To get the number of reactions per unit time per unit volume,  $R$  is multiplied by the number density of the two interacting particles. For electrons and ions interacting this would be  $n_e n_i R$  [19].

It is useful now to examine the functional forms of the recombination rates in order to gain an understanding of how the inversions in recombination lasers are

affected by the plasma parameters, namely temperature and electron density. The radiative recombination rate has the functional dependence [22],

$$R_{rr,p} \propto e^{E_p/T_e} \left( \frac{E_p}{T_e} \right)^{3/2}, \quad (2.12)$$

where  $p$  is the particular energy level in the ion,  $E_p$  is the ionization potential of that level and  $T_e$  is the plasma electron temperature. The three-body recombination also has the following functional dependence [23],

$$R_{3br,p} \propto e^{E_p/T_e} \frac{1}{T_e^3}. \quad (2.13)$$

The important consequence of the radiative rate as seen in Eq. (2.12) is that it is biased toward lower bound states and is less effective at populating higher levels such as an upper laser level. This is in contrast to the three-body rate which tends to populate the upper levels and has a much stronger dependence on the electron temperature. It is also important to note that the actual rate for three-body recombination is proportional to the square of the electron density since it requires the additional electron interaction whereas the radiative rate is only proportional to electron density.

Population inversions are created by populating upper lying levels by three-body recombination and then allowing thermal redistribution to move population to the upper laser level as discussed above. In order to preferentially pump the upper levels, strong cooling is generally required and the three-body rate must exceed the radiative rate. Otherwise the inversion will be destroyed by direct pumping of the lower levels. In addition the three body rate per unit time per unit volume is actually proportional to  $n_e^2 n_i \approx n_e^3$  since there are two electrons involved in the process. Thus the strong temperature dependence and the cubic scaling with electron density place much significance on the plasma parameters. This forces the plasma conditions necessary to produce a population inversion to be within a limited range of temperature and density parameter space.

### 2.3.1.1 X-ray laser experiments using recombination pumping

The experimental realization of recombination pumped x-ray lasers is often hindered by the demands on the plasma conditions necessary to produce inversions. In this brief section two methods to produce recombination lasers will be discussed based on collisionally ionized plasma and optical field ionized plasmas.

The collisionally ionized plasma as a medium for a recombination laser suffers from the apparently incompatible requirements of first producing a high temperature highly-ionized plasma and then trying to cool it rapidly to produce a population inversion. However it is possible to accomplish this by creating a laser-produced plasma and then allowing it to expand and thereby cool adiabatically. Actually at first glance this technique seems almost assured of producing a population inversion. That is, when a plasma expands and cools it would be expected that at some position and at some point in time the temperature and density would be appropriate for efficient pumping. It has worked in some cases, most notably the H-like  $C^{5+}$  which operates on the  $n = 3 \rightarrow n = 2$  transition at 18.2 nm [15]. Various methods to enhance the cooling through conduction or radiation have also been implemented [15].

Optical field ionization of a gas was recently proposed as a method to produce a highly non-equilibrium plasma for which recombination x-ray laser output might be achieved [24]. This scheme attempts to overcome some of the thermal problems in collisionally ionized plasmas for recombination x-ray lasers by utilizing the strong electric field of ultrafast, high intensity laser pulse to ionize electrons from atoms or ions within a time period significantly less than the recombination time of the plasma. If a long plasma filament could be created by the laser, and the plasma was imbedded in a cold background, plasma conditions could be appropriate for extremely rapid recombination leading to an inversion even to the ground state instead of an excited state as discussed above. Experiments have been conducted where a pre-formed laser-

produced plasma has been generated and then allowed to expand and cool and subsequently followed by optical field ionization with a short pulse high intensity laser. Gain has been reported using this technique in H-like Li at 13.5 nm [25].

### 2.3.2 Collisional excitation pumping

The most successful mechanism of pumping in x-ray lasers to date is electron-collisional excitation pumping. It is also the most straightforward approach to populating the upper laser level. The success of this approach is firmly grounded in well known visible and infrared lasers which utilize this mechanism [19]. In terms of x-ray lasers one can again consider iso-electronic scaling of known visible lasers to shorter wavelengths.

To illustrate the concept of collisional excitation pumping a three-level laser system like that in Fig 2.2 will be used. It is shown here again in Fig. 2.4 but the collisional processes are explicitly diagrammed as the pumping mechanism to the upper laser level. The analysis of the system in quasi-steady state is also exactly analogous to the discussion given in Section 2.2 that leads to the condition for an inversion given by Eq. (2.6). However it is useful to introduce the electron collisional excitation rate functional dependencies on the plasma parameters as was done in the previous section.

Pumping of the upper laser level via electron collisional excitation is found to have the following functional dependence [23],

$$K_{0u} \propto e^{-\Delta E_{0u}/T_e} / (\Delta E_{0u} \sqrt{T_e}), \quad (2.14)$$

where  $n_e K_{0u}$  is the pumping rate from the ground state to the upper level,  $\Delta E_{0u}$  is the energy level separation  $E_u - E_0$  and  $T_e$  is the plasma electron temperature. Collisional de-excitation serves to depopulate the upper laser level as well as empty the lower laser level. The de-excitation rate is found from the principle of detailed balance which

relates the rate of an atomic process with the rate of its inverse process. Utilizing this principle yields the following,

$$K_{ul} = K_{lu} \frac{g_l}{g_u} e^{\Delta E_{ul}/T_e}, \quad (2.15)$$

where  $g_l$  and  $g_u$  are the statistical weight for the lower and upper levels, respectively.

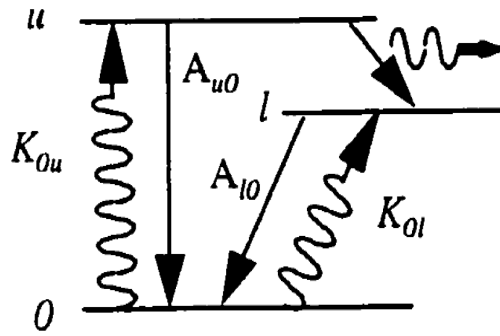


**Figure 2.4** Three-level laser energy diagram with collisional pumping processes shown.

This implies the following relation for de-excitation of the lower level,

$$K_{l0} \propto 1/(\Delta E_{l0} \sqrt{T_e}). \quad (2.16)$$

Similar relations hold for collisional de-excitation of the upper laser level to the lower laser level and to the ground state.

Considering again the three level system shown in Fig. 2.4, the energy spacing is generally such that  $\Delta E_{u0} > \Delta E_{l0} \gg \Delta E_{ul}$ . The de-excitation rate out of the lower laser level is usually quite rapid and, by energy gap considerations, larger than the rate out of the upper laser level to the ground state [19]. However, the de-excitation rate of the upper laser level to the lower laser level is therefore much greater due to the smaller energy gap. Thus, in order to establish a population inversion, it is usually necessary to have a fast radiative decay rate of the lower laser level to overcome the collisional de-

population of the upper laser level. In addition, the upper laser level should be a metastable level in that it does not decay too rapidly via spontaneous radiative decay to the ground. The metastable level requirement is important when the pumping rate to the lower level is significant as can be the case with direct electron collisional excitation.

As mentioned in Chapter 1 the Ne-like iso-electronic sequence has been quite successful in producing collisionally excited x-ray lasers. This is fundamentally due to the stability of the closed shell configuration to further ionization and, thus, the Ne-like stage exists over a wide range of plasma temperatures and densities. Fig. 2.5 shows the three level energy diagram for the  $\text{Se}^{24+}$  and  $\text{Ar}^{8+}$  Ne-like lasers. These lasers utilize the  $2p^5 3p - 2p^5 3s$  transition pumped from the  $2p^6$  ground state shown. Pumping occurs to the upper laser level by electron collisional excitation on a forbidden  $\Delta l = 0$  transition or monopole transition [15].

Fig 2.5 (b) focuses on the energy level diagram for Argon with given radiative transition rates for the upper to lower laser level and the rate for the lower level to the ground state. Substituting the rates into Eq. (2.6) gives  $N_u/N_l \approx 17$ , where the ratio of the pumping rates is approximately unity for Ne-like excitation. A population inversion is therefore assured. The only factors that could reduce gain in this system are electron-collisional mixing and radiation trapping. For the Ne-like Ar capillary discharge  $n_e^{\max} \approx 1 \times 10^{19} \text{ cm}^{-3}$  by Eq. (2.10) with  $kT_e \sim 60 - 80 \text{ eV}$  (see Chapter 3). Likewise the trapping factor  $\sigma_{0l} N_0 b$  can be approximated with Eq. (2.4) and is estimated to be close to the value for which trapping would slightly reduce the inversion.

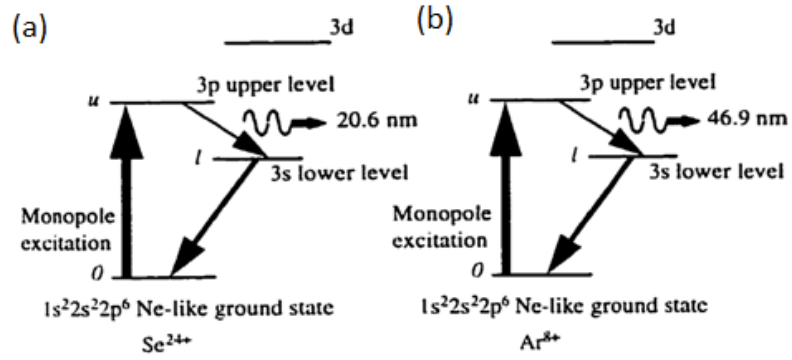


**Figure 2.5** Schematic diagram of energy levels involved in the collisionally excited Ne-like 3p-3s laser in Se and Ar. Taken from Ref. [15].

### 2.3.2.1 X-ray laser experiments using collisional excitation pumping

The previous section provided some basic concepts for understanding collisionally pumped x-ray lasers and also provided some background of the successful Ne-like scheme. Pumping by collisional excitation has proven much more fruitful than recombination pumping in terms of the number of demonstrated x-ray lasers. This is generally due to the less restrictive conditions on the plasma parameters for collisional pumping. For instance all the lasers included in Table 1.1 are collisionally pumped lasers. The two main techniques to produce the plasmas for these x-ray lasers are again laser-produced plasmas and the recently demonstrated electrically-driven capillary discharge plasma [11].

## 2.4 Capillary Discharge Driven Plasmas

The basic theory of the capillary discharge plasma, used to drive the Ne-like Ar laser, will now be described to provide a foundation for future chapters which deal directly with the dynamics of these plasmas. The first types of capillary discharges date back to the early 1960's and were investigated for the purposes of producing EUV and soft x-ray radiation [26]. The devices themselves are conceptually simple and consist of a narrow capillary channel made of an insulating material placed between two

electrodes. A high voltage electrical circuit usually containing a capacitor is discharged through the capillary, creating a plasma.

As stated previously early capillary discharge devices were mainly used for their ability to produce incoherent short wavelength radiation. It has not been until just recently that they were examined for the possibility of amplification of short wavelength radiation [27]. The primary reason behind this was the accepted notion that long column electrical discharge plasmas can be extremely non-uniform and would not support lasing action. The basis for this belief rested on many decades of research with large pulsed power devices, mainly Z- pinches and theta-pinches [15]. An example of non-uniformity in a z-pinch is shown in Fig 2.6 where the plasma along the axis is broken up and exhibits so-called instabilities. It is well known that electron density gradients in plasma cause refraction of light. The plasma of Fig. 2.6 indicates a very non-uniform plasma density such that any beam traversing the length would be subject to refraction. Such refraction losses would probably destroy any ability to achieve amplification along the length.



**Figure 2.6** X-ray pinhole photograph of a pulsed power driven (exploding wire) z-pinch plasma exhibiting extreme axial non-uniformity due to instabilities (Taken from [15]).

Demonstration of the first capillary discharge x-ray laser put an end to the notion of the non-uniformity of discharge created plasma [28]. The axial uniformity of the capillary discharge is one of the important characteristics that make it possible for amplifying short wavelength radiation. The concept of the discharge uniformity will be addressed in later chapters.



In order to produce the high electron densities and electron temperatures necessary to pump an x-ray laser in discharge devices a sufficient amount of energy must be transferred to the plasma in a relatively short period of time. Once the discharge is created the energy is deposited into the plasma through the current that flows through the column. If the current is of sufficient strength, a “pinch” will form which is the collapse of the plasma column due to the self-generated azimuthal magnetic field associated with the longitudinal current.

The pinched discharge can be treated as a balance between the inward electromagnetic forces and the outward fluid pressure forces, where the fluid is the idealistic representation of the free electron density and ion density. This is the basis of the equilibrium pinch and is used here to illustrate the constriction of plasma particles.

#### 2.4.1 Magneto-hydrodynamic model

The one dimensional single-fluid Magneto-hydrodynamic (MHD) model is based on the method of describing the Z-pinch discharge plasma as a hydro-magnetic fluid. The basic MHD equations used are depicted below.

The continuity equation (mass conservation) is given by

$$\frac{\partial \rho}{\partial t} + \nabla \cdot (\rho \mathbf{u}) = 0, \quad (2.17)$$

where  $\rho$  is mass density and  $\mathbf{u}$  is the plasma fluid velocity. Generally, in any steady state process, the rate at which mass enters a system is equal to the rate at which mass leaves the system. In this system, the continuity equation is automatically satisfied.

The momentum conservation equation is solved in the one-fluid approximation where the plasma electrons and ions are assumed to flow together as a single fluid. The momentum equation is governed by

$$\rho \frac{\partial \mathbf{u}}{\partial t} = -\nabla (P_e + P_i + P_r + q) + \mathbf{J} \times \mathbf{B} \quad (2.18)$$

where  $P_e$ ,  $P_i$  and  $P_r$  are the thermal pressures due to electrons, ions and radiation, respectively.  $\mathbf{B}$  is the magnetic field induced by the axial current and  $\mathbf{J}$  is the axial component of the electric current density. Here,  $q$  is the von Neumann artificial viscosity [29] which is included in the equation of motion to handle shocks.

The energy balance with thermal diffusion for electrons and ions are described by (refer Appendix C)

$$C_{v,e} \frac{\partial T_e}{\partial t} = V \nabla \cdot (\kappa_e \nabla T_e) + \frac{V \eta}{(4\pi)^2} |(\nabla \times \mathbf{B})|^2 - \left( \frac{\partial E_e}{\partial V} + P_e \right) \frac{\partial V}{\partial t} - C_{v,e} \frac{(T_e - T_i)}{t_{eq}} + R_{Abs} - R_{Emis}, \quad (2.19)$$

$$C_{v,i} \frac{\partial T_i}{\partial t} = V \nabla \cdot (\kappa_i \nabla T_i) - \left( \frac{\partial E_i}{\partial V} + P_i \right) \frac{\partial V}{\partial t} + C_{v,i} \frac{(T_e - T_i)}{t_{eq}} - q \frac{\partial V}{\partial t}. \quad (2.20)$$

where  $C_{v,\alpha}$ ,  $T_\alpha$ ,  $E_\alpha$ ,  $P_\alpha$  and  $\kappa_\alpha$  are, respectively, the specific heat, temperature (in eV), specific internal energy, pressure and thermal conductivity [30], of the electrons ( $\alpha = e$ ) and ions ( $\alpha = i$ ). While  $V$  is the specific volume, the second term in Eq. (2.19) is the joule heating term,  $\eta$  is defined as the plasma electrical resistivity [31],  $R_{Abs}$  and  $R_{Emis}$  are the radiation absorption and emission terms [32], and  $t_{eq}$  is the electron-ion collisional coupling term.

The difference between the temperature diffusion equations for the electrons and ions is the absence of the Joule heating term in the ion equation. Since the currents are mainly due to the lighter electrons, the energy is transferred to the ion through the collision specified by the term involving  $t_{eq}$ .

The magnetic field transport and diffusion equation reads

$$\frac{\partial \mathbf{B}}{\partial t} = \frac{\eta}{4\pi} (\nabla \cdot \nabla) \mathbf{B} - (\nabla \cdot \mathbf{u}) \mathbf{B}. \quad (2.21)$$

This equation is obtained using Maxwell equations and generalized Ohm's law with the time variation of the electric field being neglected [33] (refer Appendix D).

### 2.4.2 Coupled rate equation of the plasma

The non-local thermal equilibrium (non-LTE) atomic level population density of excited levels in ion species is coupled by the various atomic processes occurring in the plasma. We adopted the collisional-radiative model to obtain the population. The rate equation for atomic level  $i$  can be written as:

$$\frac{dn_i}{dt} = -n_i \sum_{i \neq j}^{N_L} W_{ij} + \sum_{i \neq j}^{N_L} n_j W_{ji} \quad (2.22)$$

where the first term on the right hand side refers to depopulation of level  $i$ . On the other hand, the second term accounts for population of level  $i$ .  $n_i$  is the number density of level  $i$ , and  $N_L$  is the total number of levels in the system. For upward transitions ( $i < j$ ), the depopulating rate [17] is

$$W_{ij} = \begin{cases} n_e C_{ij} + B_{ij} \bar{J}_{ij} & \text{(excitations)} \\ n_e \gamma_{ij} + \beta_{ij} + \Omega_{ij} & \text{(ionizations)} \end{cases} \quad (2.23)$$

while for downward transitions ( $i > j$ ), the populating rate [17] is

$$W_{ji} = \begin{cases} n_e D_{ji} + A_{ji} + B_{ji} \bar{J}_{ij} & \text{(deexcitations)} \\ n_e^2 \delta_{ji} + n_e (\alpha_{ji}^{RR} + \alpha_{ji}^{DR}) & \text{(recombinations)} \end{cases} \quad (2.24)$$

where  $n_e$  is the electron density;  $\bar{J}_{ij}$  is the frequency-averaged mean intensity of the radiation field over a line profile;  $C_{ij}$ ,  $\gamma_{ij}$ ,  $D_{ij}$ , and  $\delta_{ji}$  are rate coefficients for collisional excitation, ionization, deexcitation, and recombination;  $A_{ji}$ ,  $B_{ij}$  and  $B_{ji}$  are, respectively, the Einstein coefficients for spontaneous emission, and stimulated absorption and emission;  $\beta_{ij}$  is the photoionization rate;  $\Omega_{ij}$  is the autoionization rate;  $\alpha_{ji}^{RR}$  is the radiative recombination rate coefficient; and  $\alpha_{ji}^{DR}$  is the dielectronic recombination rate coefficient [34-37].

### 2.4.3 Lagrangian grid structure

These MHD equations have been adopted in the Lagrangian reference frame [38, 39] using the specific volume expression, that considers, a frame moving with the fluid at velocity  $u$ . The geometry is cylindrical with symmetry in the  $\theta$  and  $z$  directions. The position of each cell and the velocity on cell boundary are determined by

$$\frac{dr}{dt} = u. \quad (2.25)$$

All dynamical values in the equations evolve as a function of position  $r$  from the capillary axis at a time  $t$ . Zoning can be adjusted in such a way that the initial length of a zone differs from one region to the next. Conservation of mass implies that element masses do not change during the simulation, so that within every zone of the grid [40]

$$dm = \rho(r)\pi r dr. \quad (2.26)$$

This also implies that element masses do not change during the simulation. Considering an element with initial boundaries  $r_{oi}$  and  $r_{oi-1}$  and initial density  $\rho_{oi}$ , the mass is given by [41]

$$m_i = \rho_{oi}\pi(r_{oi}^2 - r_{oi-1}^2). \quad (2.27)$$

Physically,  $m$  is the amount of mass per radian per cm in the plasma.

The boundaries move in response to forces. The mass density at any time is related to the boundary positions by

$$\rho_i = \frac{m_i}{\pi(r_i^2 - r_{i-1}^2)}. \quad (2.28)$$

The average radius corresponds to the center-of-mass coordinate. Assuming a uniform density, the average of a cylinder element is related to the boundary radii by

$$R_i = \sqrt{\frac{r_i^2 + r_{i-1}^2}{2}}. \quad (2.29)$$

#### 2.4.4 Numerical method

Eq. (2.17) – (2.21) represent a set of five nonlinear coupled partial differential equations in five unknowns. These equations can be changed to Lagrangian frame of reference by using Eq. (2.26).  $m$  is now an independent Lagrangian variable and  $r$  becomes a dependent variable. Hence, we now write the system of equations in terms of  $m$ . The equations were solved numerically in a manner similar to the methods of Ref. [42]. The scheme entailed dividing the plasma into  $N$  zones and then finite differencing the equations [43], using implicit numerical solution to find  $B$ ,  $T_e$  and  $T_i$ , and an explicit solution to find  $u$  and  $r$ . Both  $r$  and  $u$  are defined at the grid nodes (cell boundary) while  $B$ ,  $T_e$  and  $T_i$  are defined at the cell centres located midway between the grid nodes. Each cell or zone is split into two subzones based on the midpoint of each cell.

To initialize the calculation, various initial and boundary conditions are given to the code. These will be discussed in next section. The code begins by dividing the plasma into  $N$  radial zones. Then the mass of each zone,  $m$ , is determined (Eq. (2.27)), and the sub-zonal masses are defined as half the zonal mass. The nodal mass is defined as the sum of the neighbouring sub-zonal masses. The nodal, zonal and sub-zonal masses all remain fixed throughout the calculation.

The basic steps of the procedure are first to calculate the velocity  $u$  from Eq. (2.18), then calculating the radius  $r$  from (2.25). Equations (2.19) – (2.21) are next solved to find  $B$ ,  $T_e$  and  $T_i$ . Then the variables are shifted and the algorithm repeats, calculating new values in terms of the previous ones. The time steps  $\Delta t$  are not constant but instead are allowed to vary subject to constraints. The stability requirement for this scheme is given approximately by the Courant-Friedrichs-Lewy (CFL) hydrodynamics stability condition in [43].

### 2.4.5 Boundary conditions

The boundary conditions which have been applied to the hydrodynamic equations (2.17) – (2.21) correspond to the simplest approximation of capillary discharge x-ray lasers. If the radius of the capillary (the outer boundary) is denoted by  $r_0$  and assuming that no particle moves through the plasma-vacuum interface, we have

$$\left[ \frac{\partial}{\partial r} T_e \right]_{r=r_0} = \left[ \frac{\partial}{\partial r} T_i \right]_{r=r_0} = 0, \quad (2.30)$$

$$u(r_0) = 0. \quad (2.31)$$

The magnetic field at the outer boundary is constrained by the Biot-Savart law to be given by:

$$B(r_0) = \frac{0.2I(t)}{r_0}, \quad (2.32)$$

where the current

$$I(t) = I_0 \sin(\omega t). \quad (2.33)$$

The boundary conditions at the radial axis are

$$\left[ \frac{\partial}{\partial r} T_e \right]_{r=0} = \left[ \frac{\partial}{\partial r} T_i \right]_{r=0} = 0, \quad (2.34)$$

$$u(0) = 0, \quad (2.35)$$

and

$$B(0) = 0. \quad (2.36)$$

In the following chapter, the set of hydrodynamic equations, expressed via Lagrangian grids subject to the above boundary conditions, will be solved numerically.

# Chapter 3

## Numerical Study of a Capillary Discharged Neon-like Argon X-Ray Laser

The purpose of these model calculations is to suggest qualitative trends in the kinetics of neon-like ions and the design of Z-pinch. In this chapter model calculations of the behaviour of neon-like soft x-ray laser for Argon will be presented. The gain coefficients for  $2s^2 2p^5 3p$  ( $J = 0$ ) to  $2s^2 2p^5 3s$  ( $J = 1$ ) transition (which occurs at 46.9 nm in argon) have been calculated and the maximum gain to be expected from the collisionally pumped neon-like laser scheme has been predicted. Further, the plasma conditions under which this gain can be expected to occur, and the appropriate Z-pinch design and external parameter inputs that will achieve these plasma conditions have been determined.

As a first estimation of the absolute gain of the  $3p \ ^1S_0 - 3s \ ^1P_1$  transition, the fraction of neon-like argon ions are calculated over a broad range of plasma conditions and then the population inversion density of the laser transitions are determined for the same set of plasma conditions. Combining these two sets of the results enables the computation of the maximum gain and the plasma conditions for which it is obtained. By then, magneto hydrodynamic (MHD) models for discharge-driven soft x-ray lasers are used to predict the input parameters that are needed to produce these plasma conditions.

### 3.1 Properties of Argon Plasma in Equilibrium

Hot dense plasmas are essentially fully ionized, that is, every atom has at least one electron removed. In fact the temperatures are sufficiently high that most atoms have many fewer bound electrons than protons in the nucleus. The ionization state (number

of electrons removed) depends primarily on the binding energies of the various electrons and on the electron plasma temperature. Typically the outer electrons in a multi-electron atom are bound by only a few electron volts, while the core K, L, and M shell electrons (principal quantum numbers  $n = 1, 2$ , and  $3$ ) are closer to the nucleus and held more tightly, with binding energies of hundreds or thousands of electron volts. Table 3.1 gives the binding energies of argon which have been compiled by NIST [44]. The first column presents the degree of ionization of the Argon atom while the second column shows the energy in electron volts required to remove an electron from that ionization state.

Argon, in its neutral state, has 18 electrons. The first row of Table 3.1 indicates that 15.8 eV of energy is needed to remove one electron, creating the  $\text{Ar}^{1+}$  ion. The energy required to remove an additional electron is 27.6 eV, forming the  $\text{Ar}^{2+}$  ion. Subsequently, having removed eight electrons, there are 10 electrons remaining ( $\text{Ar}^{8+}$ ), forming a closed shell in a neon-like ( $1s^2 2s^2 2p^6$ ) configuration. The high symmetry of the closed shell makes removal of an additional electron much more difficult; hence, they maintain their stability even when faced with temporal, spatial, and other changes and the ionization potential (binding energy) jumps significantly to 422.5 eV for neon-like argon. This remarkable threshold grows for further electron removal can be considered an ionization bottleneck for a plasma of a given temperature.

As a first estimation of absolute gain of this transition, the fractional abundance of charge states is evaluated using steady-state ionization model [45]. PrismSPECT [46] is a collisional-radiative spectral analysis code designed to simulate the atomic and radiative properties of laboratory and astrophysical plasmas and it solves the equation of state and provides radiative properties for plasma in non-local thermodynamic equilibrium (non-LTE) and local thermodynamic equilibrium (LTE) state. To obtain a neon-like argon state ( $\text{Ar}^{8+}$ ) the equilibrium argon plasma must be heated to a



temperature of about 41 eV (Table 3.1). The ionization population fraction in the range  $T_e \sim 1 - 10000$  eV for a given electron number density  $N_e \sim 2.0 \times 10^{18} \text{ cm}^{-3}$  are depicted in Fig. 3.1. The electron number density  $N_e \sim 2.0 \times 10^{18} \text{ cm}^{-3}$  has been chosen to be shown in this section, because it is the electron number density that has been achieved during the pinch of the case study in the section 3.5. The maximum ionization population fraction of neon-like  $\text{Ar}^{8+}$  ion  $f^{8+} \approx 0.95$  is accomplished at temperature  $T_e \approx 41$  eV. The temperature range of Ne-like ionization state is approximately between  $10 - 200$  eV. It should be remembered that the steady-state ionization model neglects the time taken to ionize the plasma. The average charge  $Z$  as function of temperature (see Fig. 3.2) has two regions where it changes quickly and has two temperature plateaus  $T_{e1} \sim 20 - 60$  eV (at  $Z \sim 8$ ) and  $T_{e2} \sim 400 - 1000$  eV (at  $Z \sim 16$ ). The ionization plateaus can be understood from the ionization bottleneck of the electron configuration of the argon atom.

**Table 3.1** The ionization potential was extracted from [44] and peak abundance of Argon was calculated using PrismSPECT code [46].

Ionization	Potential, eV	Abundance	Temperature, eV
0	15.8	0.9411	1.0
1+	27.6	0.9609	1.8
2+	40.7	0.8732	3.1
3+	59.7	0.8780	5.2
4+	75.1	0.7430	8.9
5+	91.0	0.5475	13.0
6+	124.3	0.5551	17.5
7+	143.5	0.2395	21.0
8+	422.5	0.9478	41.0
9+	479.7	0.5431	95.0
10+	540.0	0.3871	125.0
11+	618.7	0.3493	155.0
12+	685.9	0.3167	185.0
13+	755.2	0.2888	220.0
14+	855.8	0.3683	250.0
15+	918.4	0.2740	310.0
16+	4120.7	0.9074	800.0
17+	4426.2	0.5711	2500.0

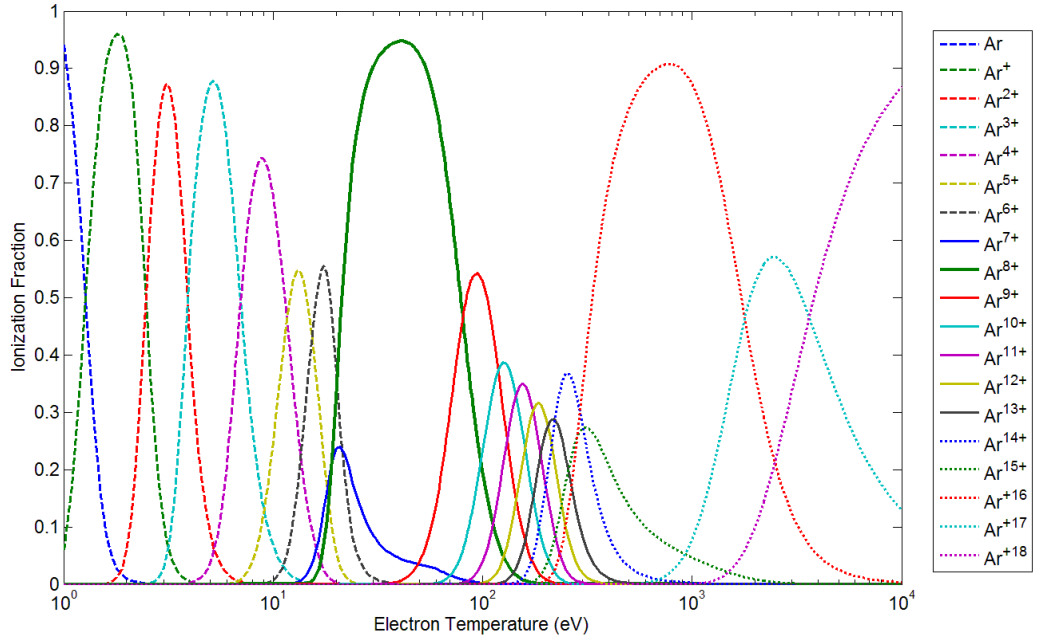


**Figure 3.1** Argon ionization fraction dependence on plasma electron temperature for atom density  $N_0 \sim 2 \times 10^{18} \text{ cm}^{-3}$ .

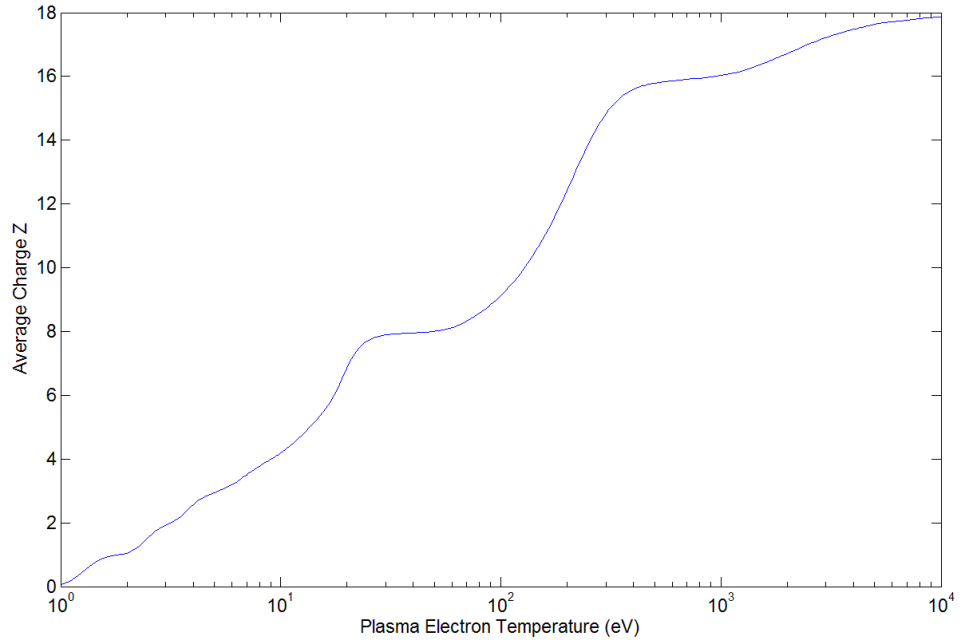


**Figure 3.2** Average plasma charge  $Z$  for the Argon atom with density  $N_0 \sim 2.0 \times 10^{18} \text{ cm}^{-3}$  as a function of temperature.

### 3.2 Population and gain requirements for Ne-like Ar

From the proceeding section, the electron temperature needed to obtain Ne-like Argon was identified. Yet in existence of laser regime, the transition of finer structure of ion has to be taken into account. So in the scheme of yielding a 46.9 nm laser line, the population inversion of  $3p\ ^1S_0 - 3s\ ^1P_1$  transition has been studied and this was usually measured by the gain.

For Doppler-broadening, the gain ( $G$ ) of a radiative transition which consists the population density of an upper laser level  $u$  and a lower laser level  $l$  is expressed as [15]

$$G_{ul}^{q+} = \frac{1}{8\pi} \sqrt{\frac{M_i}{2\pi k T_i}} A_{ul} \lambda_{ul}^3 g_u \left( \frac{n_u^{q+}}{g_u} - \frac{n_l^{q+}}{g_l} \right), \quad (3.1)$$

where  $\lambda_{ul}$  represents the transition wavelength  $A_{ul}$  is the transition probability (radiative decay rate),  $T_i$  is the temperature of ion,  $n_j^{q+}$  is the ion population density in the level  $j$  of ion  $q^+$  having statistical weight  $g_j$ ,  $k$  is the Boltzmann constant, and  $M_i$  is the ionic mass.

In Helios-CR, the relative level populations are  $m_j^{q+} = n_j^{q+} / n^{q+}$ , where  $n^{q+}$  represents the total (summed over all of the levels of the ion under investigation) number density of the  $q^+$  ion. Therefore, Eq. (3.1) can be rewritten for gain per total Ne-like Ar ion density ( $G_{ul}^{8+} / n^{8+}$  in units of  $\text{cm}^{-4}$ ), where  $q = 8$  denotes the Ne-like Ar) as

$$\frac{G_{ul}^{8+}}{n^{8+}} = \frac{1.01 \times 10^{-31}}{T_i^{1/2}} A_{ul} \lambda_{ul}^3 g_u \left( \frac{m_u^{8+}}{g_u} - \frac{m_l^{8+}}{g_l} \right), \quad (3.2)$$

where  $\lambda$  and  $T_i$  are expressed in Å and eV, respectively. The right-hand side of Eq. (3.2) consists of terms only related to Ne-like Ar. Hence, it represents inherent characteristics of gain on a transition in Ne-like Ar for a given  $N_e$  and  $T_i$ .

To estimate the absolute value of gain, the population density of ions can be related to ionization balance by writing

$$n^{8+} = \frac{n^{8+}}{N_i} N_i = \delta^{8+} N_i. \quad (3.3)$$

Here,  $N_i$  is the total ion density and  $\delta^{8+}$  is the fractional abundance of the Ne-like Ar ion. Eq. (3.3) takes into account the different statistical weights for lower and upper laser levels ( $g_u = 1$ ,  $g_l = 3$ ). Hence, lasing starts at the moment when population inversion is achieved.

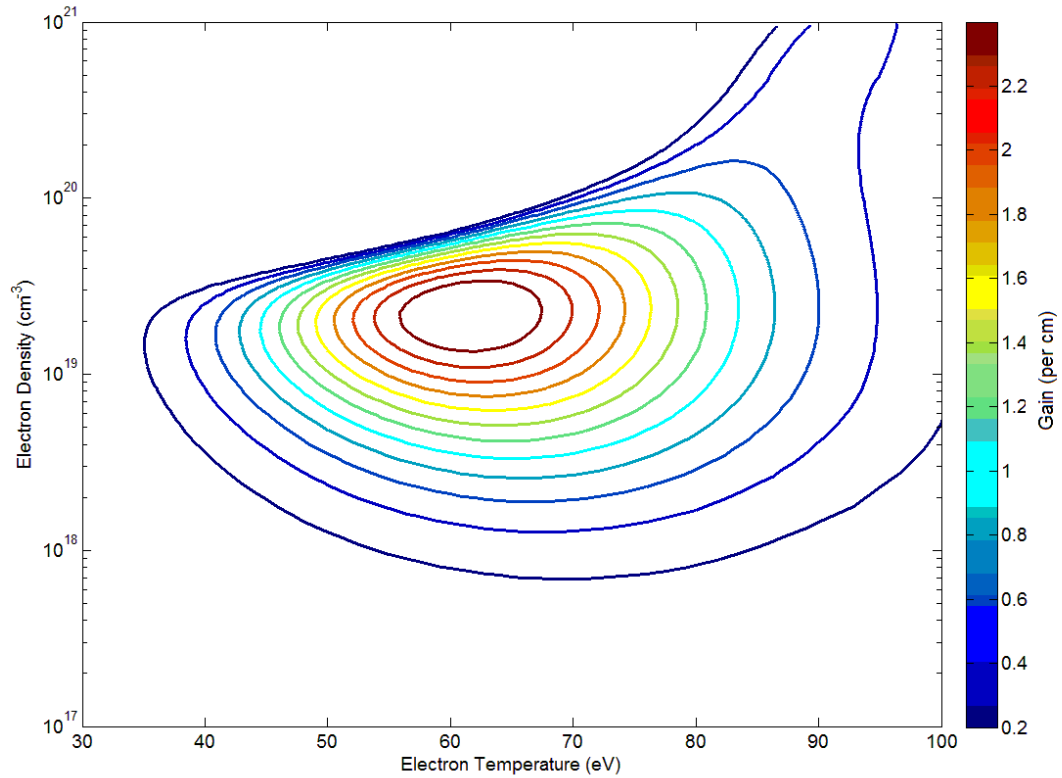
Fig. 3.3 presents a contour plot of gain against  $N_e$  and  $T_e$ , computed using the steady-state ionization model. The effect of reabsorption of the resonance radiations on the distribution of population density of excited-states has been neglected (optically-thin plasma assumption). In addition, it has been assumed that the electron and ion temperature are similar, i.e.,  $T_e = T_i$ . This assumption generally gives the upper limit of gain in capillary discharge.

Fig. 3.3 indicates that large gain formed for  $N_e \approx 2 \times 10^{19} \text{ cm}^{-3}$ . For the regime  $N_e > 10^{20} \text{ cm}^{-3}$ , collisional depopulation rate exceeds that of radiative decay. Hence, the populations will be distributed corresponding to the Boltzmann distribution function and the collisional quench of the population inversion occurs (i.e., unsuitable gain regime). Although the fractional abundance of Ne-like Ar becomes maximum at  $T_e \approx 40 \text{ eV}$  using the steady-state approximation for ionization model (in Fig 3.1), the optimum regime of gain is approximately at  $T_e \approx 60 \text{ eV}$ , as shown in Fig. 3.3. This shows an inconsistency between electron temperature that maximizes gain and fractional abundance of Ne-like Ar ion, which is a conventional problem of Ne-like x-ray lasers [47]. The inconsistency accrues by considering of the excitation energy into the  $n = 3$  levels is generally three-quarters of the ionization energy and consequently gives a temperature which large ground-state excitation rates will lead to large

ionization rates if the electron density is adequate (the relaxation time for the ionization balance  $\sim 10^{11} n_e^{-1}$ ) [48].

The collisions between particles in the plasma transfer energy from particle to particle in a random manner, thereby heating the plasma and ionizing the atoms. Normally, multiple ionization states are developed, each with its own characteristic emission lines, leading to a rich spectrum of lines. However, by carefully controlling the temperature and density of the plasma, the population of specific ionization species can be preferentially established. Generally, such high temperatures and densities are established at, or close to the pinch radius.

Under certain plasma conditions (electron density of  $0.1 - 4 \times 10^{19} \text{ cm}^{-3}$ , and electron temperature  $\approx 40 - 90 \text{ eV}$ , as shown in Fig.3.3), collisional electron impact excitation of the ground state Ne-like ions produces a population inversion between the  $3p$  ( $J=0$ ) and the  $3s$  ( $J=1$ ) levels resulting in amplification at the  $46.9 \text{ nm}$  wavelength.



**Figure 3.3** The contour of gain of the  $3p \ ^1S_0 - 3s \ ^1P_1$  transition as function of the electron temperature and density.

### 3.3 Case Study: Ionization Dynamics and One-dimensional MHD Model

In plasmas created by fast capillary discharge, ionization dynamics are extremely important, in particular for low- $Z$  atom species, due to the very fast time scales of changing hydrodynamical plasma parameters at the pinching time leading to ionization state distributions which are far from their steady-state values. The time scales for atomic processes are large compared to the time scales for the change of the plasma parameters, so the transient effects become more prominent. Hence, in order to estimate the non-equilibrium effects on gain of Ne-like Ar ion, only the time progression of the ground states is reproduced during the calculation of hydrodynamical plasma parameters using the one-dimensional, two-temperatures MHD model with cylindrical geometry which is solved in the Lagrangian reference frame.

As a case study, an experiment described in Ref. [18] has been selected. The stimulation of every discharge consists of three steps:

- a) Time and radial dependencies of electron temperature, mass plasma density and electron density are assessed by the MHD code Helios-CR [17].
- b) Time dependencies of energy level populations and ionization fractions for Ne-like Ar ions are evaluated by the kinetic code [17].
- c) Time dependencies of gain on the capillary axis are estimated according to Eq. (3.2).

### 3.4 The Initial Parameters

Using the general physical model outlined in chapter 2, the discharge channel can be stimulated with specific values of the controlling parameters. The parameters of a working discharge x-ray laser reported in Ref. [18] are used. Here the radius of the capillary has been fixed at 0.15 cm, and current rise time is about 50 ns. For this basic

situation, the filling pressures and the current profiles are varied to investigate the impact of these variations on the plasma.

For the simulations, we use the HELIOS-CR code described in Ref. [17]. It is a code which designed to study the progression of radiating plasmas in 1-dimension. The dynamics of plasmas heated by external radiation sources or by laser beams in planar, cylindrical, or spherical configuration can be studied in this code. It is also a modelling platform that can design for non-LTE and LTE plasmas in one dimension.

The capillary is prefilled with neutral argon to a certain initial filling pressure. In this case study, the pressure 0.15mbar is used. The initial ion density can be written as

$$n_i = P_0 N_a \times 41.1 \times 10^{-6} \text{ (in cm}^{-3}\text{)}, \quad (3.4)$$

where  $P_0$  denotes the initial gas filling pressure and  $N_a$  is Avogadro's number. In the experiment, a pre-pulse current was used to pre-ionized the capillary just before the arrival of the main current so that a uniform plasma discharge that is favourable for lasing is obtained. In order to initiate the discharges in the simulation, the filling gas was artificially pre-ionized by setting its initial electron temperature to 0.25 eV. The peak discharge current used is 16 kA. These are the typical values used in the laser of Ref. [18].

### 3.5 Results of MHD simulations

In the capillary discharge regime, the plasma column created by the injected current pulse induces a fast radial collapse towards the axis, producing a shock wave that compresses and heats the plasma column with a large density of Ne-like ions, with a very high axial uniformity and a large length to diameter ratio of the order of 1000:1. In Ne-like schemes, the plasma tends to readily adopt the Ne-like stage due to ionization bottlenecks. Under certain plasma conditions (electron density of  $0.1 - 4 \times 10^{19} \text{ cm}^{-3}$ , and electron temperature  $\approx 40 - 90 \text{ eV}$ , as shown in Fig.3.3), the soft x-ray laser of 46.9

nm produces from a population inversion between the 3p ( $J=0$ ) and the 3s ( $J=1$ ) levels by using collisional electron impact excitation of the ground state Ne-like ions.

Fig. 3.4 presents the calculated temporal evolution of a capillary discharge with a peak current of 16 kA and 0.15 mbar gas filling pressure. The temporal evolution of the trajectories of argon plasma elements inside the channel of this configuration is illustrated in Fig. 3.4a. Here, the blue line represents the discharge current which extracted from experiment. Figure 3.4b shows contour plots of the logarithm of the electron density measured in  $\text{cm}^{-3}$  while Figure 3.4c shows the electron temperature measured in eV. These figures also provide quantitative information about the distribution of the plasma parameters inside the channel at different times. Some characteristic features are discussed below.

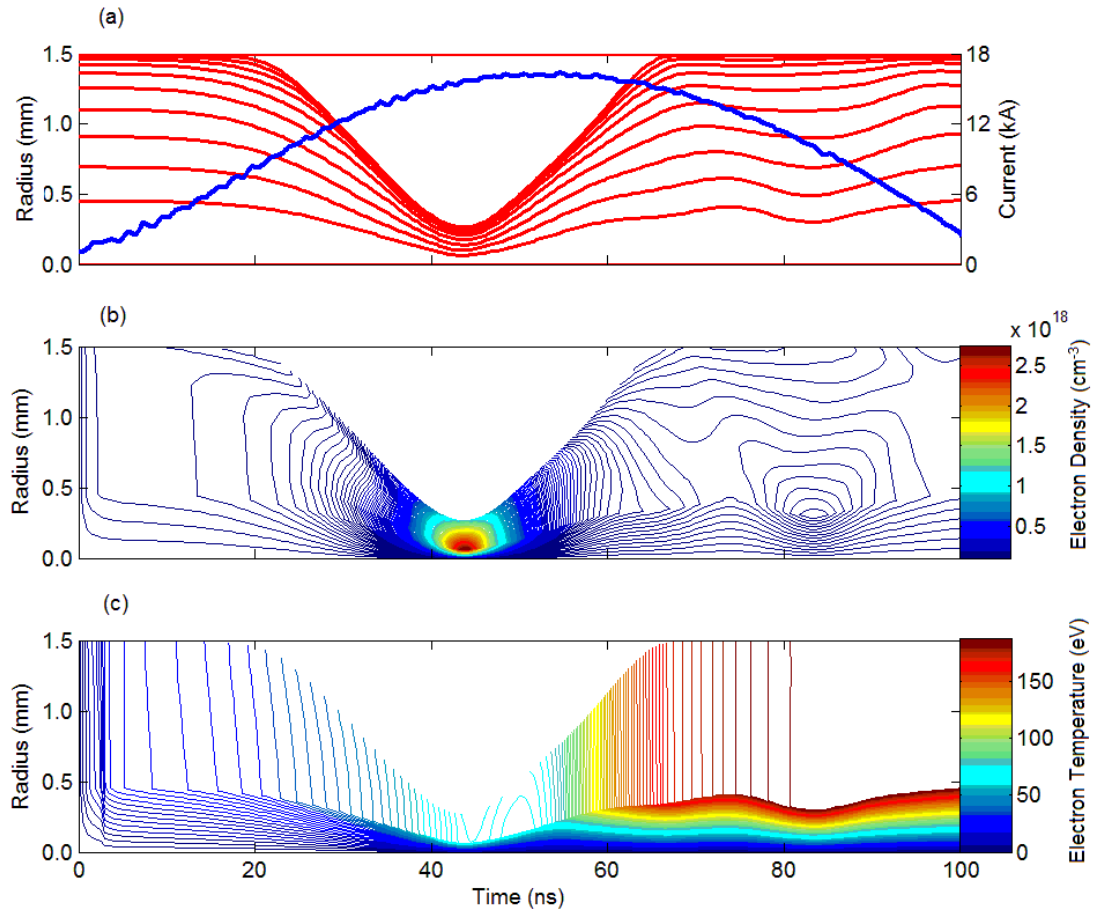


**Figure 3.4** Basic parameters of discharge in capillary with diameter of 3 mm filled with argon at a initial gas filling pressure of 0.15 mbar for  $I_0 = 16$  kA and rise time 50 ns. (a) The plasma time-space flow diagram; blue line corresponds to the discharge current at outer boundary; (b) contour lines of the natural logarithm of the electron density (measured  $\text{cm}^{-3}$ ) on the  $(t, r)$  plane; (c) contour lines of the electron temperature (measured in eV).



The evolution of Z-pinch plasma can be depicted by the balance between the magnetic pressure and the thermal pressure or so called the magnetic piston as described by Eq. (2.18). In the early stages ( $t < 20$  ns) the plasma does not compress immediately but actually tries to expand due to the fact that the plasma pressure exceeds other forces. However, this expansion is constrained by the rigid wall of the capillary. The pressure in the outer zones of the plasma is due to both the initial filling pressure and Joule heating. Generally, the current tends to flow in the outer part of the cylindrical plasma, and Joule heating occurs due to the current passing through the plasma. This heating results in an increase in pressure which can be sufficiently high for the outer regions of the plasma to initially expand before being accelerated inward by the magnetic piston.

When the discharge current has reached a value such that the magnetic pressure is greater than the thermal pressure (i.e., for  $t > 20$  ns), the plasma is compressed inward toward the axis. At the same time, a vacuum region starts to form near the wall and a converging shock wave is developed which propagates towards the channel axis. The shock waves eventually meet at the axis, and are subsequently reflected. During compression, the plasma becomes hotter due to Joule and shock heating, and the thermal pressure increases, essentially ionizing the argon. Before the time 50 ns, when the total current has been increasing to the maximum value, the discharge current is high and the Lorentz force dominates. Thus, the compression phase ceases. When the thermal pressure balances the magnetic pressure, the plasma reaches maximum compression ( $t \approx 43.5$  ns) and then expands ( $t > 43.5$  ns). During the compression, the plasma has been finally produced to high density and temperature plasma on the axis, as shown in Fig. 3.4b and 3.4c. At  $t = 43.5$  ns, the temperature  $T_e$  reaches the value of 70 eV and should rapidly cool down. The value of electron density  $N_e$  at the pinch is about  $3 \times 10^{18} \text{ cm}^{-3}$ . A hot plasma core with the radius  $r_{core} = 0.266$  mm and central mass density  $\rho_{core} = 1.22 \times 10^{-4} \text{ g/cm}^3$  is formed. However, after compression the shock

wave gets reflected from the axis to the wall of plasma column. Eventually, this reflected shock hits the compression plasma boundary. Hence it continues heat up to 160 eV during expansion due to the inner zones of plasma trying to compress again after the first pinch.

At the stage of expansion the uniformity of the plasma column may be disrupted by the MHD instabilities which cause turbulent mixing and heat transport. Hence, this is crucial to find discharge regime that free of MHD instabilities during the expansion and the suggestion was also made by Bobrova *et al* [49] that to enhance the MHD stabilities, the current pulse needs to be short enough which, under the condition of the ratio between the time scale for a shock wave to reach the channel axis and time scale for the external circuit, is about 1.

The dynamics of plasma column in capillary discharge can be also described via the current distribution in Fig. 3.5. In the propagation of compression wave, after 20 ns, the plasma column (a thin layer) was developed together with approximately 30 – 40% total current. At the same time, less than ~1% of the full current is inside the region close to the axis. This means that in the initial stage of the discharge, the Lorentz force is the main source of the shock wave formation. Then the magnetic pressure transfers the energy to the argon plasma as kinetic energy. Hence, during the compression the magnetic field does not play a significant role in plasma column formation. This kinetic energy later is converted into thermal energy after the shock wave gets reflected and heats the plasma column [49].

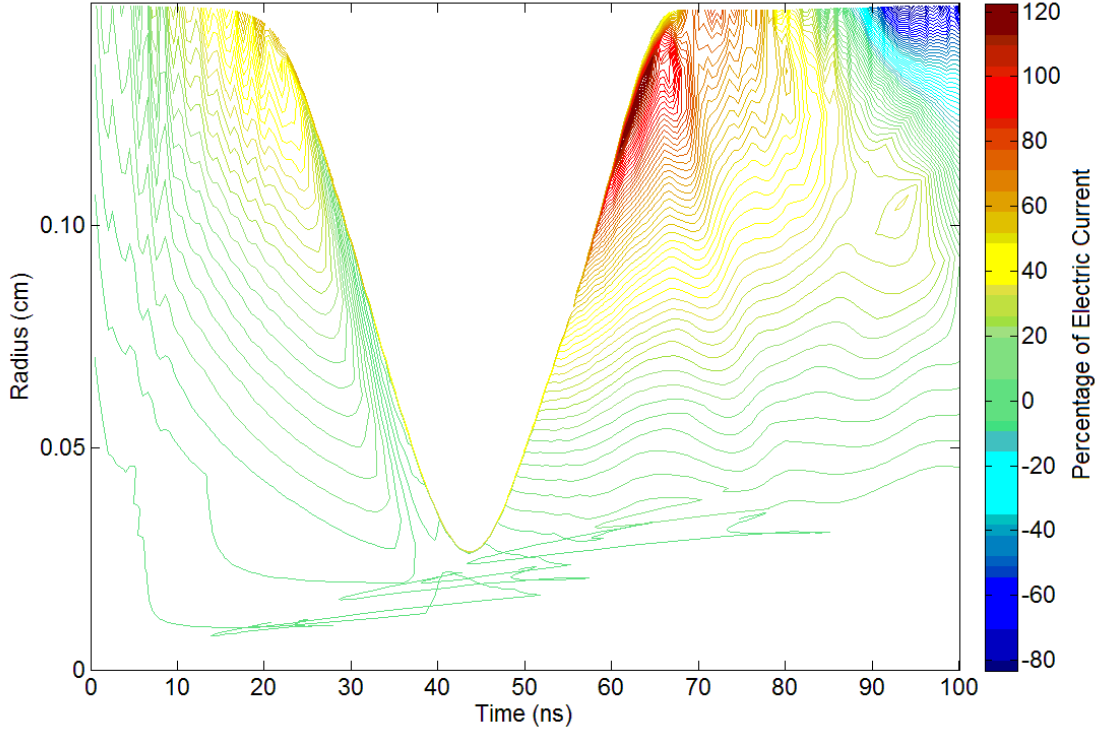


**Figure 3.5** Contour lines of the percentage of electric current (which normalized over 16 kA of peak discharge current) inside the region with radius  $r$  and time  $t$ .

### 3.6 Argon Ionization and Energy Level Populations

The Helios-CR code [17] has been used to simulate the temporal variation of the ionization states and energy level populations. Significant changes of population densities and ionization occur in the time interval from 35 ns to 80 ns, i.e. during the pinch collapse (see Fig. 3.6 and 3.7). The population densities of neon-like argon ( $\text{Ar}^{8+}$ ) ions grow rapidly and become dominant in the compression part of the pinch. At the pinch time (43.5 ns), neon-like argon ( $\text{Ar}^{8+}$ ) ions achieved the maximum population value. The population of these ions is dominant throughout the expansion of the plasma.

The levels  $\text{Ar}^{8+} 3s \ ^1P_1$  and  $\text{Ar}^{8+} 3p \ ^1S_0$  begin to be populated once the population of  $\text{Ar}^{8+}$  ions become significant. For example, at  $t = 37$  ns,  $n_{\text{Ar}^{8+}} \sim 10^{14} \text{ cm}^{-3}$  (see Fig. 3.7).

At  $t = 37$  ns onward, as long as the population inversion of upper laser level  $\text{Ar}^{8+} 3s \ ^1P_1$  remains greater than lower laser level  $\text{Ar}^{8+} 3p \ ^1S_0$  where statistical weights have been taken into account ( $g_u = 3$ ,  $g_l = 1$ ), the laser action occurred. On the other hand, due to

the ionization bottleneck of  $\text{Ar}^{8+}$ , the density of its population was maintained at a high level as expected, compared with other species of ions.

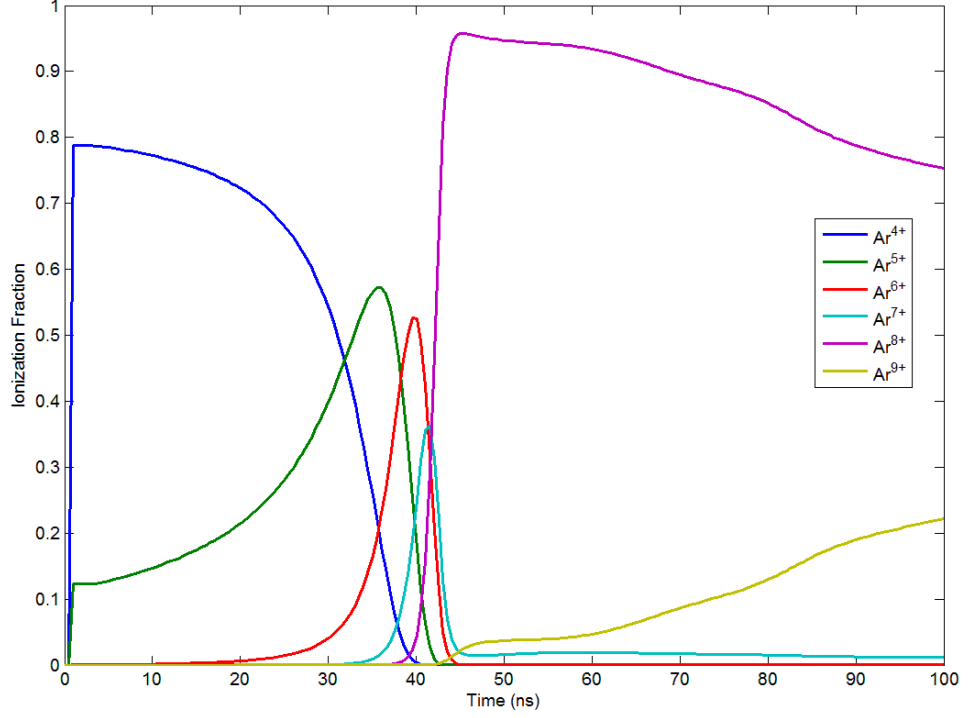


**Figure 3.6** Substantial changes of ionization fraction as a function of time.

A comparison of Ne-like Ar ionization states shown in Fig. 3.1 using a steady-state approximation and Fig. 3.6 on the capillary axis using a time-dependent ionization calculation shows that in the transient ionizing plasma, the ionization state distribution shifts to higher temperature as compared to the steady-state approximation. For example, the Ne-like Ar fraction in Fig. 3.6 has a value about 0.95 at  $T_e \approx 70$  eV (which is shown in Fig. 3.4 (c)), while the steady-state approximation at the same temperature predicts a value  $\approx 0.7$ . In other words, a time-dependent ionization calculation required higher electron temperature to achieve maximum Ne-like ionization state. This is because of the finite relaxation time in the case of steady state [45]. In addition, after the pinch time ( $> 43.5$  ns), Fig. 3.6 shows the lag of ionization fraction due to high  $T_e$  and low  $N_e$ ,

which means long time of recombination or freezing of charge states as compared with steady-state ionization model.

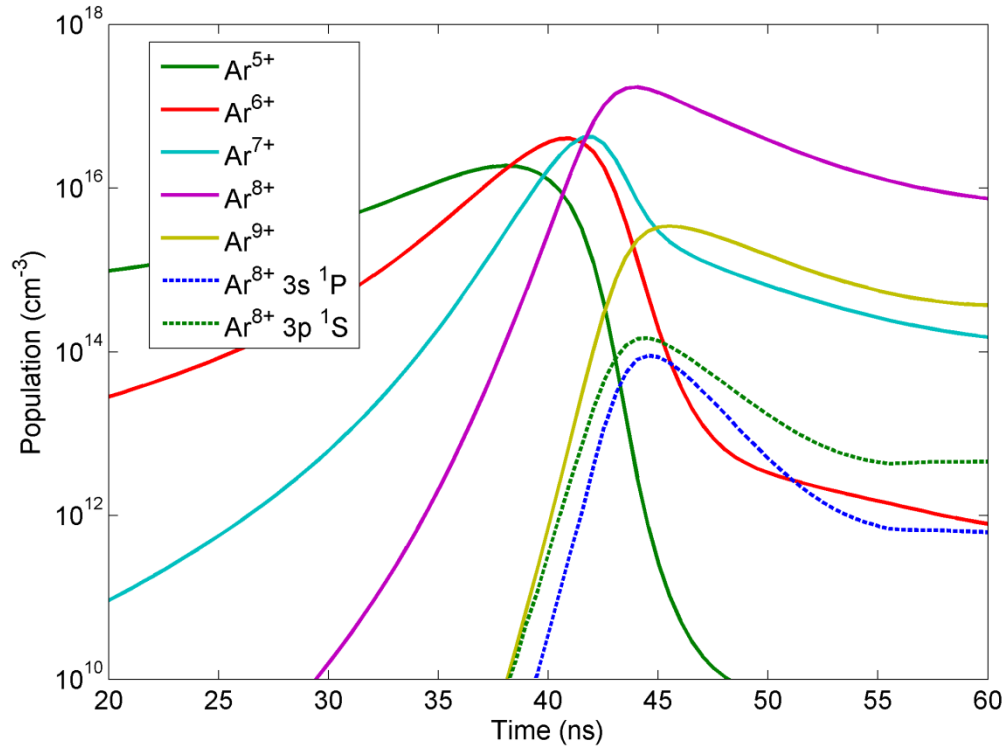


**Figure 3.7** Population densities of Ar ions as a function of time.

### 3.7 Gain factor time dependence

The time dependence of small signal gain factor  $G$  is determined by the time dependences of both laser level populations  $n_{3p\ ^1S_0}^{8+}$  and  $n_{3s\ ^1P_1}^{8+}$ . Fig. 3.8 shows the radial and temporal evolution of the gain of the case above (a non-ablating alumina capillary with radius  $r_0 = 1.5$  mm filled with initial gas filling pressure of 0.15 mbar, current pulse with  $T_{1/4} = 50$  ns and current peak value  $I_{\max} = 16$  kA). The gain factor has a shape of very short peak with maximum value  $G(t_G) = 0.94$  cm<sup>-1</sup> on the capillary axis at the time  $t_G = 44.5$  ns (see Fig. 3.8) where the corresponding electron density is  $3.3 \times 10^{18}$  cm<sup>-3</sup> and electron temperature is 72 eV. The peak value of gain is achieved during the pinch time. The active laser medium is created for a relatively short period

approximately equal to 3.5 ns (Full width half maximum (FWHM) of the gain peak was considered). This gain value was fulfilled with plasma conditions (electron density of  $0.1 - 4 \times 10^{19} \text{ cm}^{-3}$ , and electron temperature  $\approx 40 - 90 \text{ eV}$ , as shown in Fig.3.3).

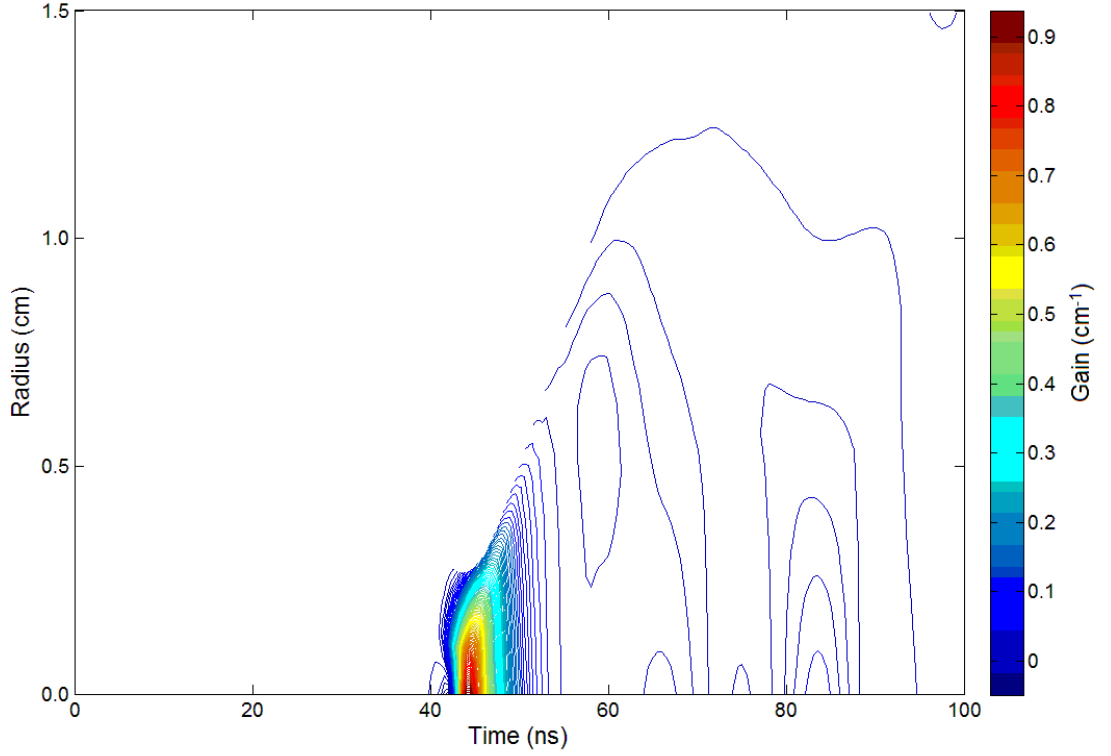


**Figure 3.8** The spatial and temporal evolution of gain.

### 3.8 Influence of Opacity on Gain Coefficients

The effect of opacity (i.e., reabsorption) on the gain coefficient has been investigated. The static optical depth ( $\tau_{ul}$ ) at line centre ( $\lambda_{ul}$ ) on a radiative transition between the levels  $u$  and  $l$  is defined by [15]

$$\tau_{ul} = K(\lambda_{ul})L, \quad (3.5)$$

where  $L$  is the effective length of the plasma.  $K(\lambda_{ul})$  is the absorption coefficient as

$$K(\lambda_{ul}) = r_c \left( \frac{\pi M c^2}{2 k T_i} \right)^{1/2} N_u \lambda_{ul} f_{ul} \quad (3.6)$$

where  $f_{ul}$  is the absorption oscillator strength between the levels  $u$  and  $l$ ,  $c$  the speed of the light in vacuum,  $M$  the atomic mass of the ion,  $r_c$  is the classical radius of an electron,  $k$  is the Boltzmann constant,  $T_i$  the ion temperature and  $N_u$  is the number density of the upper level  $u$ .

In order to estimate the opacity effect, the absorption coefficient of each Lagrangian cell is calculated based on the outputs from Helios-CR. Basically the ion temperature and the number density of the upper level  $u$  were post-processed into the calculation of absorption coefficient. Fig. 3.9 reveals that the opacity effect reduces the gain due to overpopulation of lower laser level for these conditions.

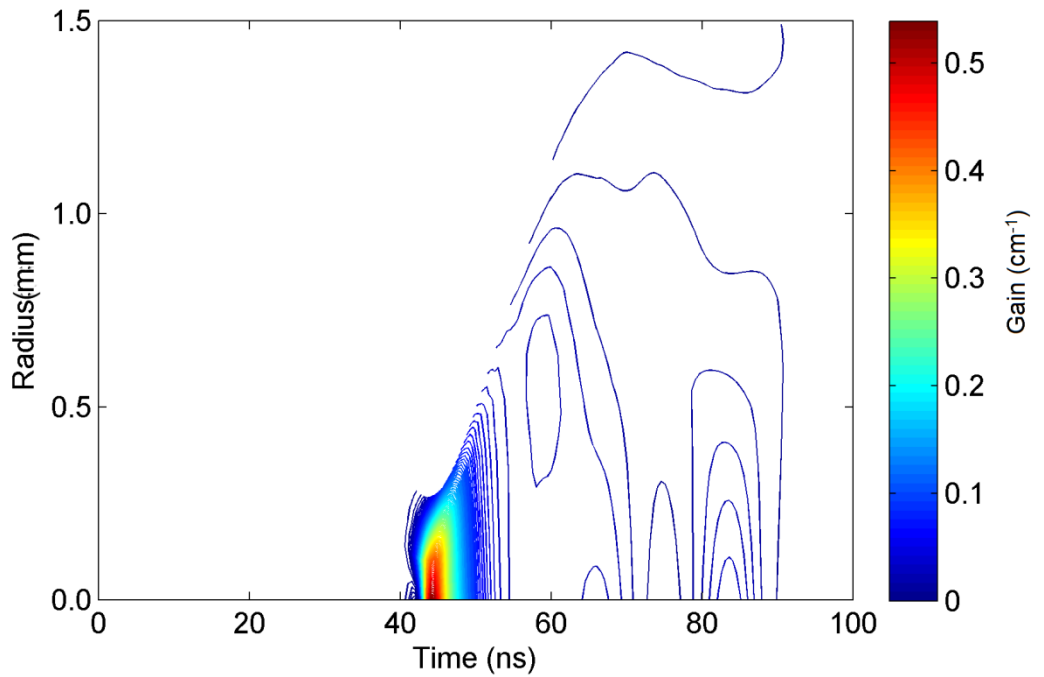


**Figure 3.9** The spatial and temporal evolution of gain after taking opacity effect into account.

Here, the value of the peak gain has been reduced to  $0.54 \text{ cm}^{-1}$  from a maximum of  $0.94 \text{ cm}^{-1}$  in the absence of opacity effects. This reduction of gain is due to the overheating of ions at the maximum compression time, close to the axis of the capillary.

### 3.9 Comparison with Other Experiments

Up to this point, no data can be compared with the experiment of [18], because the only available experiment output is laser intensity. So in order to investigate the accuracy of simulation MHD model, Helios-CR code [17], other experiments (i.e. Rocca [50], Niimi [51] and Heinbuch [52]) are considered in this section.

These three experiments were chosen because they had more define parameters such as the size of laser was imaged and the time of compression was roughly captured in their studies. These experiments inputs and outputs later will help in verify the results of the simulation from Helios-CR code for each case. In the way, the dynamic of plasma in Z-pinch which has been studied in section 3.5 – 3.8 using Helios-CR code can be explained and understood more.

#### 3.9.1 Case 1: Rocca's experiment

Rocca's experiment [50] showed a sequence of time-resolved pinhole images of the soft x-ray emitting region of the plasma column as a function of time for a 39 kA peak current with a half-period of about 60 ns, discharging through a 4 mm diameter, 12 cm long capillary filled with argon at 700 mTorr pressure.

The image obtained at 26 ns from the beginning of the current pulse show the emission from cylindrical shell and the diameter of the soft x-ray emitting region is 3.5 mm. The FWHM diameter of the radiating region of the plasma column at the time of maximum compression (about 41 ns) is measured to be  $\sim 200$  and  $\sim 300 \mu\text{m}$  with and without a thick carbon foil filter which filters out radiation with  $\lambda > 30 \text{ nm}$ , respectively. Fig. 3.10 presents the calculated temporal evolution of a capillary discharge with a peak current of 39 kA and 700 mTorr gas filling pressure. The temporal evolution of the trajectories of argon plasma elements inside the channel of this configuration is illustrated in Fig. 3.10a. Here, the dotted line represents the discharge current. Fig.



3.10b shows contour plots of the logarithm of the electron density measured in  $\text{cm}^{-3}$  while Fig. 3.10c shows the electron temperature measured in eV. Fig. 3.10d shows contour plots of the fraction of ion  $\text{Ar}^{8+}$  and Fig. 3.10e shows contour plots of the gain measured in  $\text{cm}^{-1}$ . These figures also provide quantitative information about the distribution of the plasma parameters inside the channel at different times.

By comparison, the simulated results from Helios-CR in Fig. 3.10 shows that the plasma column pinches at 45 ns (this estimate agrees with Rocca's calculation [50]) with a maximum compression of 1 mm diameter. The corresponding electron density is  $1.3 \times 10^{19} \text{ cm}^{-3}$ , the corresponding electron temperature is 64 eV, the fraction of  $\text{Ar}^{8+}$  ion is 0.89, the gain without opacity effect is  $3.17 \text{ cm}^{-1}$  and the gain with opacity effect is  $\sim 1 \text{ cm}^{-1}$ . The simulated pinch time differs by 4 ns as compared to the measured pinch time. This small shift can be accounted for. The size of plasma column during maximum compression in the simulation is greater than that of the experiment because only the FWHM radiating region of the plasma column was measured in the experiment. Hence, the actual size of plasma column should be bigger than that reported, so it gave good agreement with the simulation. The size simulated radiating region of the plasma column will be estimated in section 5.4 and the size of diameter is predicted to be about  $400 \mu\text{m}$ .

The requirement of the temperature and density of the plasma were falling in an adequate regime that estimated in section 3.2. However the calculated gain is much higher than the estimation value in Fig. 3.3. This is because the calculated gain was generated from the non-local thermodynamic equilibrium (non-LTE) model, while the results displayed in Fig. 3.3 used the LTE model. In other words, the plasma was far from its equilibrium state.

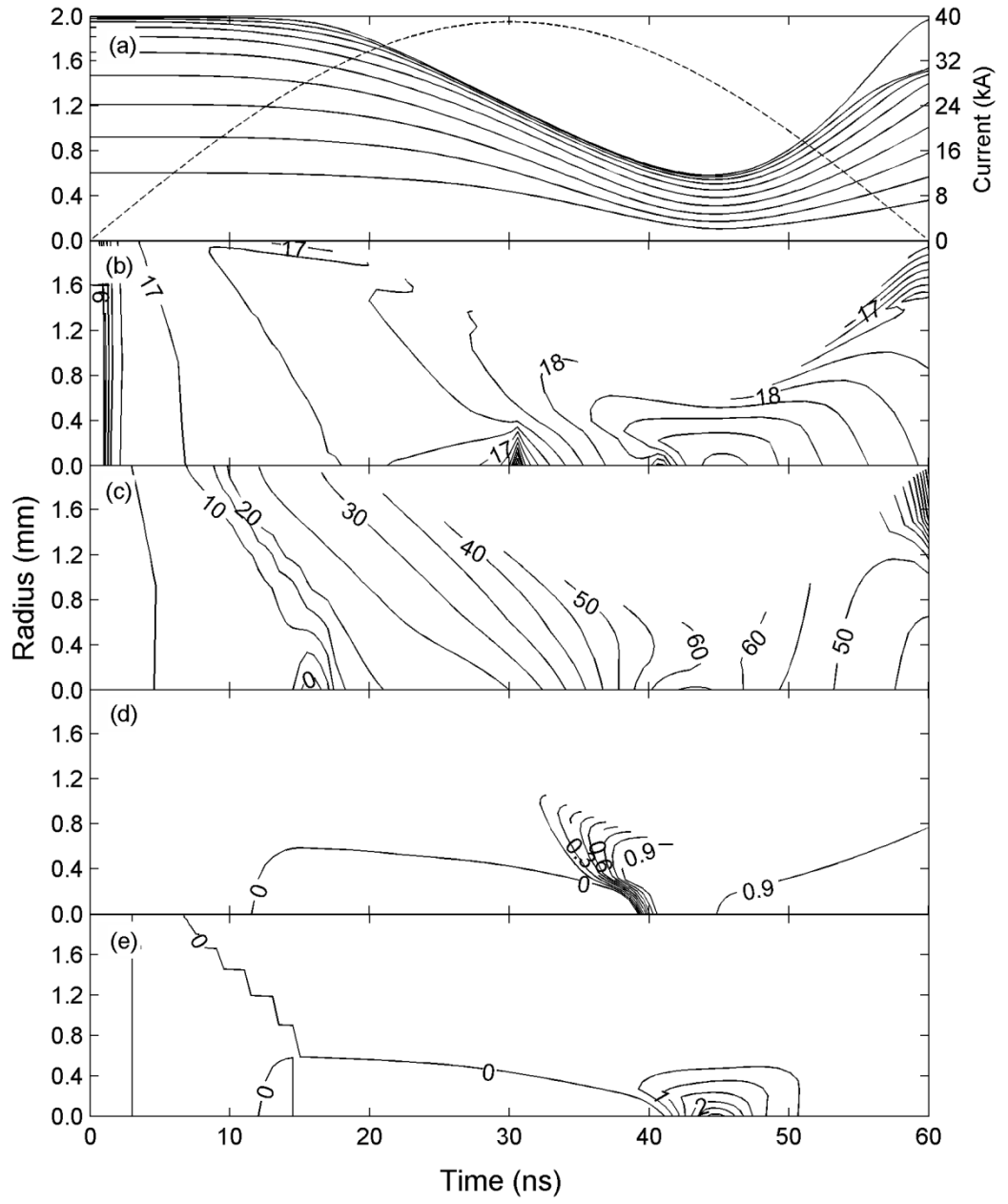


**Figure 3.10** Basic parameters of a discharge in a capillary of diameter of 4 mm filled with argon at a initial gas filling pressure of 700 mTorr for  $I_0 = 39$  kA and rise time 30 ns. (a) The plasma time-space flow diagram; the dotted line corresponds to the discharge current at outer boundary; (b) contour lines of the logarithm of the electron density (measured  $\text{cm}^{-3}$ ) on the  $(t, r)$  plane; (c) contour lines of the electron temperature (measured in eV); (d) contour lines of the fraction of ion  $\text{Ar}^{8+}$ ; (e) contour lines of the gain (measured  $\text{cm}^{-1}$ ).

### 3.9.2 Case 2: Niimi's experiment

In Niimi's experiment [51], side-view observations of the plasma have been performed using a Pyrex glass capillary. Argon gas filled the capillary at 150 mTorr pressure. The main discharge of 27 kA with a rise time of 50 ns flowed in the capillary with and without pre-discharge.

The framing photographs showed that onset of instability was observed at pinch time (i.e. between 30 to 40 ns) and the reproducibility of the plasma was considerably enhanced in the capillary with pre-discharge. In the capillary-discharge plasma with a pre-discharge current of 10 A, the framing photographs showed the pinch time to be between 20 to 30 ns and the diameter of discharge plasma at this time was about 300  $\mu\text{m}$ . In Niimi's experiment, the aperture was kept open for 10 ns. Hence it is not possible to determine more precisely the time when the pinch occurs.

Fig. 3.11 shows the calculated outputs based on the parameters used in this experiment. The time of the simulated pinch at 32.5 ns and the diameter of discharge plasma at this time was about 600  $\mu\text{m}$ . The size of the pinch plasma reported in the experiment was measured is from the radiating region, so the actual size of the plasma column should be  $> 300 \mu\text{m}$ . So in general the simulated diameter of the pinch plasma 600  $\mu\text{m}$ , which later in section 5.4 shows the radiating region to be about 400  $\mu\text{m}$ , is acceptable. The corresponding electron density during the simulated pinch time is  $4.4 \times 10^{18} \text{ cm}^{-3}$ , the electron temperature is 130 eV, the fraction of ion  $\text{Ar}^{8+}$  is 0.82 and the calculated gain value is  $2.7 \text{ cm}^{-1}$  (see Fig. 3.11) and the opacity effect reduced the gain to  $1.2 \text{ cm}^{-1}$ . Although the calculated gain value is high, the electron temperature is not in the region where 40 – 90 eV (required in order to have population inversion) and the plasma also tends to compress again toward the peak of the current flow. This causes the instability of the pinch which was also observed in the experiment. As conclusion that the initial gas filling pressure was low and caused the plasma to overheat during the

pinch. So lasing action did not occur in this experiment, which was also corroborated in the simulation.

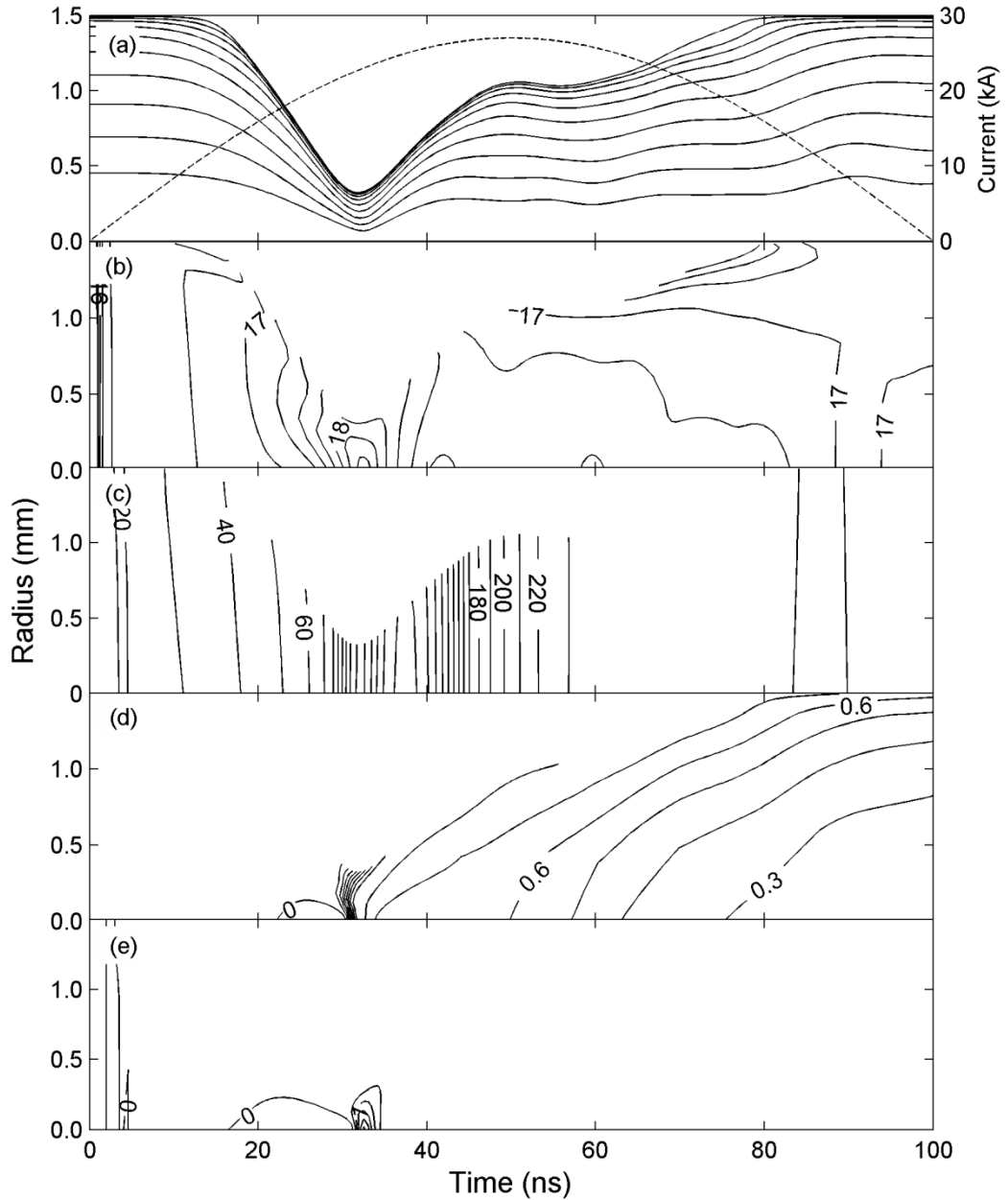


**Figure 3.11** Basic parameters of discharge in capillary of diameter 3 mm filled with argon at a initial gas filling pressure of 150 mTorr with  $I_0 = 27$  kA and rise time 50 ns. (a) The plasma time-space flow diagram; the dotted line corresponds to the discharge current at the outer boundary; (b) contour lines of the decimal logarithm of the electron density (measured  $\text{cm}^{-3}$ ) on the  $(t, r)$  plane; (c) contour lines of the electron temperature (measured in eV); (d) contour lines of the fraction of ion  $\text{Ar}^{8+}$ ; (e) contour lines of the gain (measured  $\text{cm}^{-1}$ ).

### 3.9.3 Case 3: Heinbuch's experiment

In Heinbuch's experiment [52], laser amplification was obtained on Ne-like Ar plasma column generated in an aluminium-oxide capillary of 3.2 mm interior diameter and 21 cm length filled with pre-ionized Ar gas at an optimized pressure 0.7 Torr. The plasma was excited by current pulses of 22 kA peak amplitude that were monitored with a Rogowski coil. The pulse had 10% to 90% rise time of approximately 60 ns.

The pinch was reported to have occurred at about 40 ns after the beginning of the main current pulse and the plasma column reached its minimum diameter of 200 – 300  $\mu\text{m}$ . The laser was successfully operated from shot to shot variation of the peak of the excitation current pulse for 1500 consecutive shots at repetition rates up to 12 Hz.

Comparing with the simulated results shown in Fig. 3.12, the plasma column pinches at about 60 ns with a maximum compression diameter of about 1.5 mm. The corresponding electron density is  $2.6 \times 10^{18} \text{ cm}^{-3}$ , the corresponding electron temperature is 46 eV, the fraction of ion  $\text{Ar}^{8+}$  is 0.98, the gain without opacity effect is  $0.18 \text{ cm}^{-1}$  and the gain with opacity effect is  $0.11 \text{ cm}^{-1}$ .

The gain peak value dropped as the electron temperature was too low. It is suggested that the initial gas filling pressure needs to decrease to, say 500 mTorr. A reduced mass density inside the capillary would cause the shock to pinch faster and cause the plasma to get heated more easily than at 700 mTorr pressure.

On the other hand, the difference between the measured pinch time and the simulated pinch time is about 20 ns. This discrepancy can be explained as follows: 1500 consecutive shots were measured in the experiment, the plasma inside the capillary was in a pre-discharge state every shot. The first shot of the experiment was predicted (using Helios-CR code) about the same with a single pulse was considered in the simulated case where uniform initial electron temperature of 0.25 eV and electron density (vary according to initial gas filling pressure) were performed. In the simulation,

every single shot was treated as identical. In contrast, for 1500 consecutive shots in the experiments, the pre-discharge plasma will be well developed based on the previous shots. So the pinch time would be even earlier and the pinch diameter would be smaller were expected.

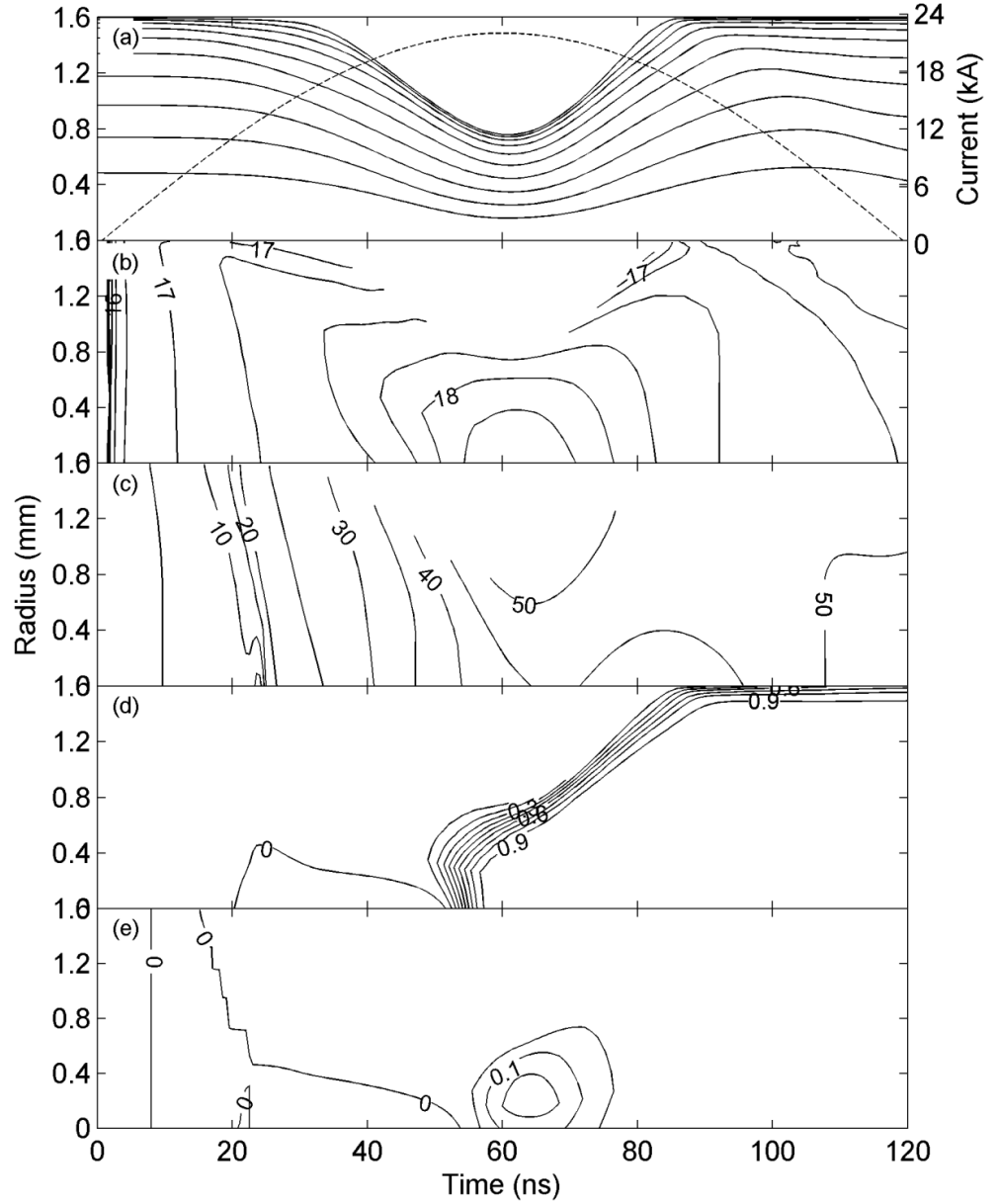


**Figure 3.12** Basic parameters of discharge in a capillary with diameter of 3.2 mm filled with argon at a initial gas filling pressure of 700 mTorr for  $I_0 = 22$  kA and rise time 30 ns. (a) The plasma time-space flow diagram; dotted line corresponds to the discharge current at outer boundary; (b) contour lines of the decimal logarithm of the electron density (measured  $\text{cm}^{-3}$ ) on the  $(t, r)$  plane; (c) contour lines of the electron temperature (measured in eV); (d) contour lines of the fraction of ion  $\text{Ar}^{8+}$ ; (e) contour lines of the gain (measured  $\text{cm}^{-1}$ ).

Based on the comparison of these three experiments, the simulated pinch time has been shifted forward by about 5 ns. Results in Ref. [52] revealed that, in contrast to the some artificial adjustment of the classical transport coefficients described in many published reports using single-fluid MHD simulation, the effect of neutral atoms should taken into account using two-fluids MHD equations to better estimate pinching time. However, the discrepancy may also be related to initial plasma condition (for example, pre-ionization) in capillary discharge [53, 54].

A perusal of Fig.3.3, Fig. 3.4 and Fig. 3.8 shows that the initial conditions, for instance, the initial gas filling pressure, the peak current form and the radius of the capillary need to be further optimized to produce the higher gain coefficient of the Ne-like Ar x-ray laser. These will be shown in chapter 4 in which a detailed study of the influence of the input parameters to the optimization of the system is performed.

On the other hand, the results show an overheating of ions at pinching time near the axis of the capillary, which reduces the gain. In reality, the function of ion temperature is caused to reduce gain owing to line broadening (see. Eq. (3.1)), and (ii) to increase the gain due to reduction of opacity effect [55]. The latter one has nonlinear effect on the population distributions.

In addition, the results show that the maximum gain coefficient for Rocca's experiment occurred on the capillary axis was about  $1 \text{ cm}^{-1}$  and the effective gain coefficient in that experiment was somewhat lower than this value ( $\sim 0.6 \text{ cm}^{-1}$ ), which may be due to the refraction loss. Although the effects of the wall ablation and the effect of neutral atoms on the plasma dynamics have not been taken into account in the calculation, the estimated value for gain has agreement with all experiments that were considered [15].

The estimated diameter size of the plasma during the pinch was also in range of acceptance region. The estimation of the diameter of the radiating plasma will be further

discussed in Chapter 5 in which refraction losses are included. In order to obtain the laser amplification, it is necessary to produce a plasma that satisfies the lasing condition and provides a laser gain. These require that the temperature and density of the plasma have to be within an adequate regime as suggested in section 3.2.

In conclusion, from the study of three experiments above, the Helios-CR code was able to give a good agreement with the experimental results. Tan's experiment [18] has been simulated by Helios-CR code whereby the dynamics of the plasma can be understood quantitatively. Although the output of Tan's experiment only provided the information of laser intensity, the diameter of radiating region during maximum compression can be estimated to be  $< 500 \mu\text{m}$  (the simulated radius of plasma column from Helios-CR is about 0.266 mm) and the actual pinch time may occur at 48 ns after initiation of the discharge current, whereby the stimulated pinch time is predicted to be at 43.5ns (based on the evaluation of three experiments, the simulated pinch time has been shifted forward by about 5 ns).



## Chapter 4

### Laser System Optimization of Ne-like Ar Soft X-ray Laser

The experiment of Tan [18] was studied in the previous chapter which showed that the plasma's electron temperature was 72 eV and its electron density was  $3.3 \times 10^{18} \text{ cm}^{-3}$  during pinch time. This pair of values estimated the gain of the  $3p \ ^1S_0 - 3s \ ^1P_1$  transition to be about  $1 \text{ cm}^{-1}$  in Fig. 3.3. This indicates that, with suitable adjustment of plasma conditions during the pinch, there is the possibility of obtaining a higher gain  $3p \ ^1S_0 - 3s \ ^1P_1$  transition than achieved in the case study studied in the previous chapter. Hence, this motivates the study of laser system optimization of Ne-like Ar soft x-ray laser in this chapter.

In these models, the relevant experimental parameters are the capillary radius  $r_0$ , initial argon gas filling pressure  $p_0$ , discharge current peak value  $I_{max}$  and its quarter period  $T_{1/4}$ . Hence, the optimization is performed in the four-dimensional space  $(r_0, p_0, I_{max}, T_{1/4})$  of the experimental parameters, taking the peak values of the gain factor  $G(t_G)$  where  $t_G$  is the pinch time (when the minimum plasma radius of the capillary), electron temperature and electron density as the criteria to be achieved.

#### 4.1 Dependences of plasma parameters and gain factor on the pressure

The simulations of the capillary discharge dynamics for  $r_0 = 1.5 \text{ mm}$ ,  $T_{1/4} = 50 \text{ ns}$ ,  $I_{max} = 16 \text{ kA}$  at various initial gas filling pressures  $p_0$  of argon have been performed. Fig. 4.1(a) shows that the pinch time  $t_G$  on reaching the minimum radius of the capillary is tuned by the choice of the initial gas filling pressure  $p_0$ . For lower values of  $p_0$  the pinch time  $t_G$  on reaching the minimum plasma radius of the capillary occurs at an earlier time. This is because, for the lower initial values of  $p_0$ , the mass density inside the capillary is reduced which makes the plasma easier to compress and to heat.

Fig. 4.1(b) and (c) show the temporal evolution of the electron density and electron temperature on the axis of the capillary at various initial gas filling pressures. The electron density increases with increasing initial gas filling pressure. On the other hand, the values of electron temperature decrease with increasing initial gas filling pressure.

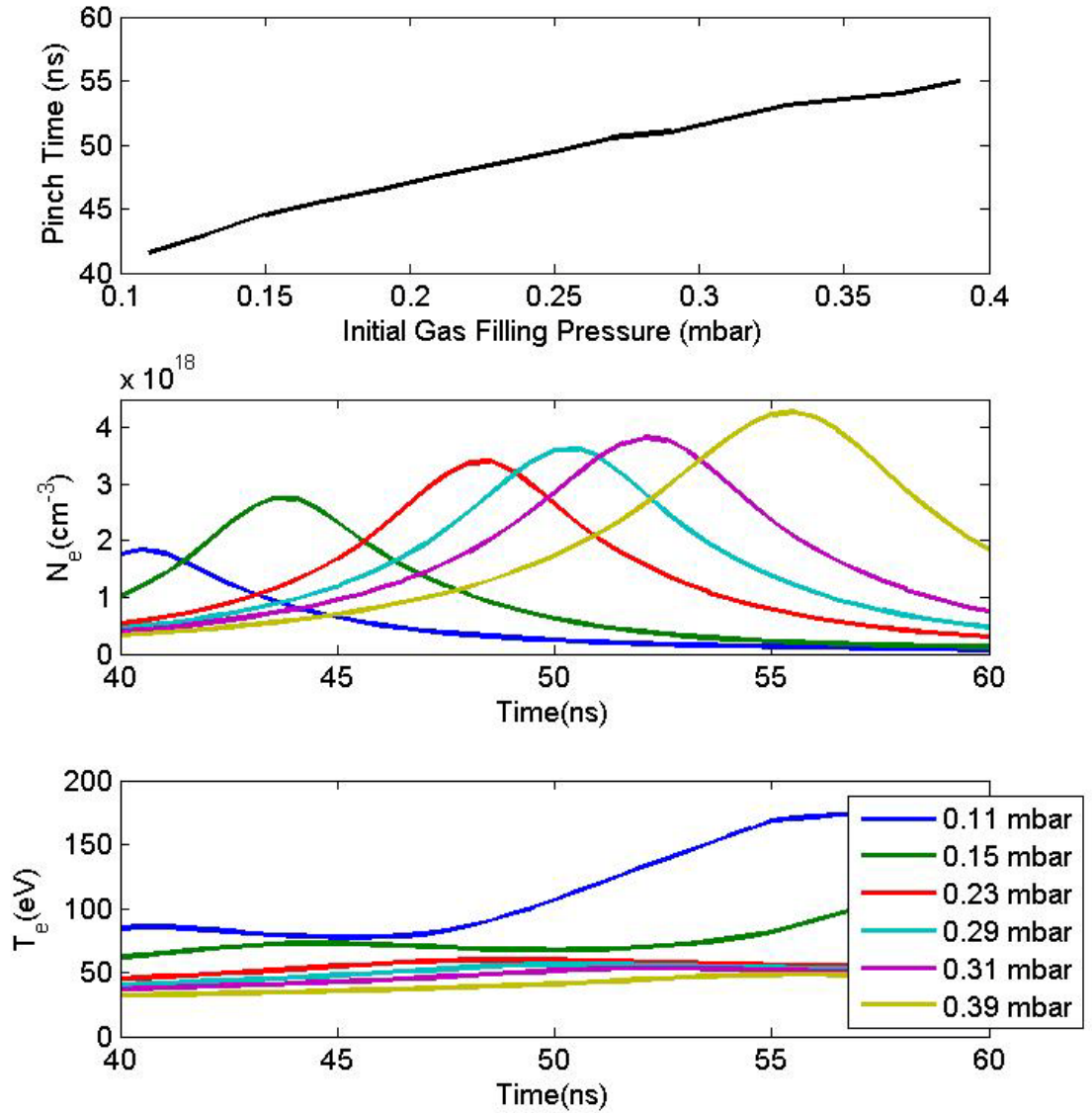


**Figure 4.1** (a) Maximum compression time versus initial gas filling pressure, (b) Temporal evolution of electron density, (c) Temporal evolution of electron temperature.

The gain factor time-dependences have been also calculated for various initial gas filling pressures  $p_0$ . The values of the gain factor are very sensitive to the changes of

initial gas filling pressure  $p_0$  [cf. Fig. 4.2]. The highest value of the peak gain on the axis  $G(t_G)$  is achieved for  $p_0 = 0.15$  mbar (see Fig.4.2). The corresponding peak value of electron temperature  $T_{e,\max}(t_G) = 72$  eV results in highly ionized plasma with abundance of  $\text{Ar}^{8+}$  (see Fig.3.4c) and with the electron density  $N_e(t_G) = 3.3 \times 10^{18} \text{ cm}^{-3}$  (see Fig. 3.4b).

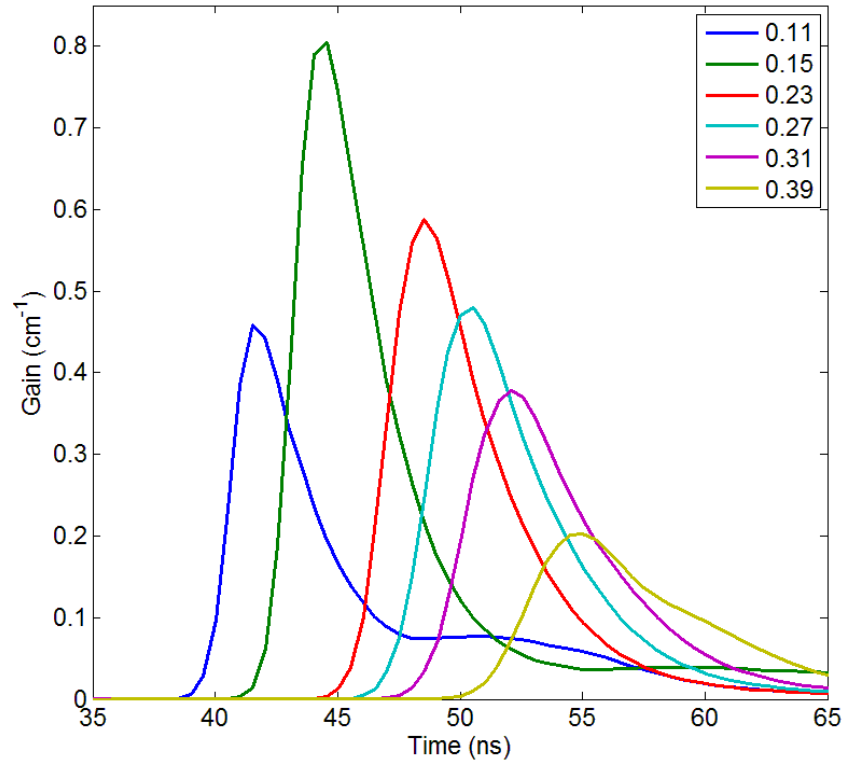


**Figure 4.2** Time dependences of the gain factor on the axis of alumina capillary ( $r_0 = 1.5$  mm, rise time 50 ns,  $I_{\max} = 16$  kA) for various initial gas filling pressures (in mbar).

## 4.2 Dependences of the pressure-optimized gain factor on the current peak value

Fig. 4.3 shows the peak discharge currents ranging from 13.5 kA to 19 kA obtained from the experiments of Tan [18].

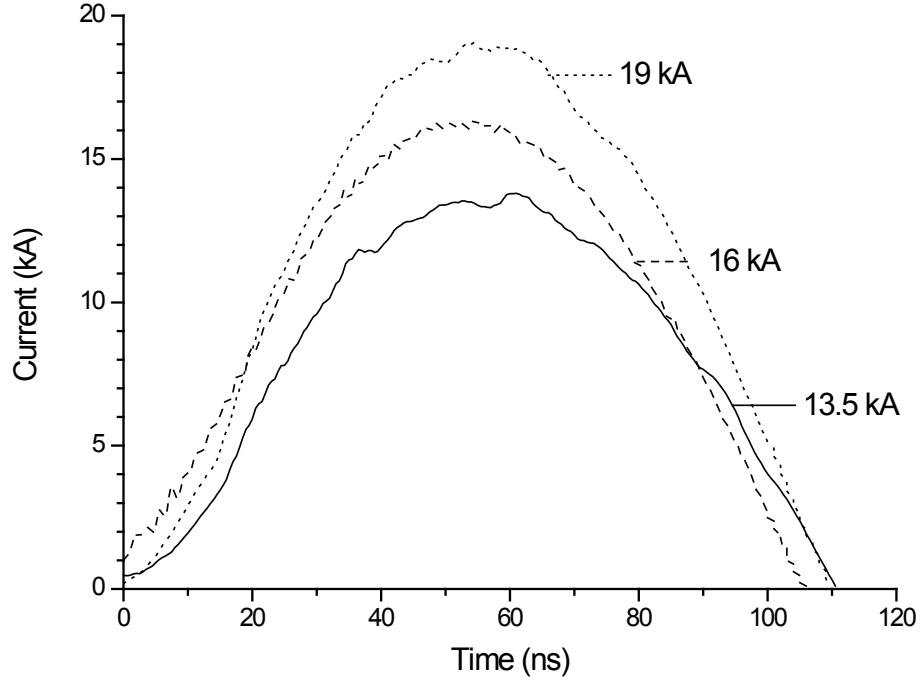


**Figure 4.3** Current wave form for 13.5 kA, 16 kA and 19 kA which are extracted from the experiments of Tan [18].

In Fig. 4.4, displays a contour plot of electron density versus electron temperature (where temporal information has been suppressed) at various gas filling pressures. The results of electron temperature  $T_{e,max}(t_G)$  and electron density  $N_e(t_G)$  for 13.5 kA, 16 kA and 19 kA are summarized in Fig. 4.4. The range of electron temperature  $T_{e,max}(t_G)$  broadens with the increase in the peak discharge current,  $I_{max}$ , i.e., from 40 – 70 eV (for  $I_{max} = 13.5$  kA), 45 – 85 eV ( $I_{max} = 16$  kA) to 58 – 100 eV (for  $I_{max} = 19$  kA) with the range of  $p_0$  0.11 – 0.35 mbar; whereas the range of electron density  $N_e(t_G)$  ( $2 - 6 \times 10^{18}$  cm<sup>-3</sup>) for 19 kA of peak discharge current is higher than the range of electron density  $N_e(t_G)$  ( $0.8 - 2 \times 10^{18}$  cm<sup>-3</sup>) for 13.5 kA of peak discharge current with the same range of initial gas filling pressures of 0.11 – 0.35 mbar. While the electron densities  $N_e(t_G)$  in

the range of  $4.2 - 1.6 \times 10^{18} \text{ cm}^{-3}$  for 16 kA of peak discharge current. So Fig. 4.4 describe the case of initial input parameters, i.e.  $r_0 = 1.5 \text{ mm}$ ,  $T_{1/4} = 50 \text{ ns}$  and the range of  $p_0$  is from 0.11 – 0.35 mbar remain unchanged, the increment of  $I_{max}$  give effect of the increment of the range of electron temperatures  $T_{e,max}(t_G)$  and electron densities  $N_e(t_G)$ . This further increase the gain values,  $G(t_G)$ . However, this increment of the gain values,  $G(t_G)$ , will hit the maximum value. This gives that the limitation of  $I_{max}$  would be implied to avoid electron density  $N_e(t_G)$  is too high and resulting optical thick plasma; also to prevent from high electron temperatures  $T_{e,max}(t_G)$  as the outcome ions  $\text{Ar}^{8+}$  abundance are demolished and low gain values  $G(t_G)$  would be obtained.

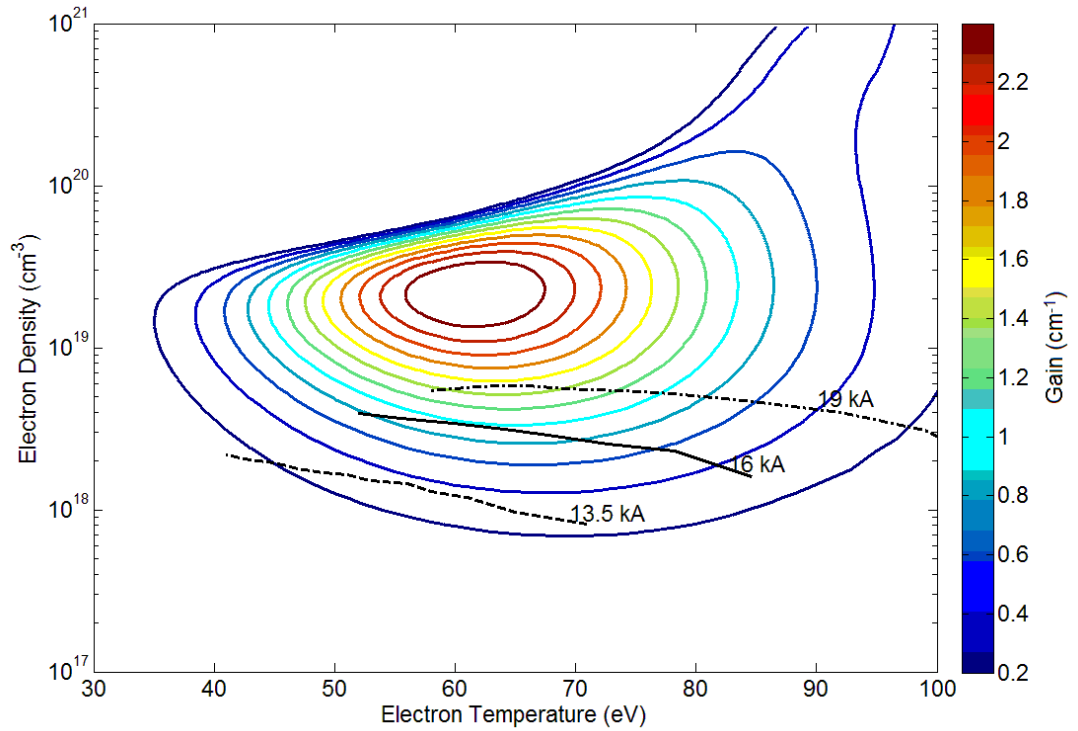


**Figure 4.4** The electron densities and electron temperature on the axis of the capillary during the maximum compression with various initial gas filling pressures for the peak discharge,  $I_{max}$ , of 13.5 kA (black dash line), 16 kA (black solid line) and 19 kA (black dot-dash line) which superposed from the Fig. 3.3.

Note that, the rightmost points of each  $I_{max}$  line in Fig. 4.4 is corresponds to  $p_0 = 0.11 \text{ mbar}$ . If  $p_0$  has been fixed to 0.11 mbar and all other parameters remain unchanged, the results show that for higher discharge current, the compression by the magnetic

piston is more severe and hence, faster shock front speed. This gives rise not only to higher electron temperature, but also to higher electron density. This leads to overheating of the plasma so that the conditions suitable for lasing are destroyed. In order to reduce the electron temperature, higher initial gas filling pressure is needed when high discharge currents are needed.

Fig. 4.5 shows the dependency of the gain factor peak values  $G(t_G)$ , with opacity effect included, on the initial gas filling pressures for discharge current peak of 13.5 kA (dashed line) and 19 kA (solid line) which were calculated from the non-LTE model. A comparison with the contour gain factor  $G(t_G)$  of Fig. 4.4 which was calculated from LTE model, shows only a slight difference at these peak discharge currents in the gain factors  $G(t_G)$  derived from the LTE and non-LTE models become even bigger at higher peak discharge currents, as will be shown in the following sections.

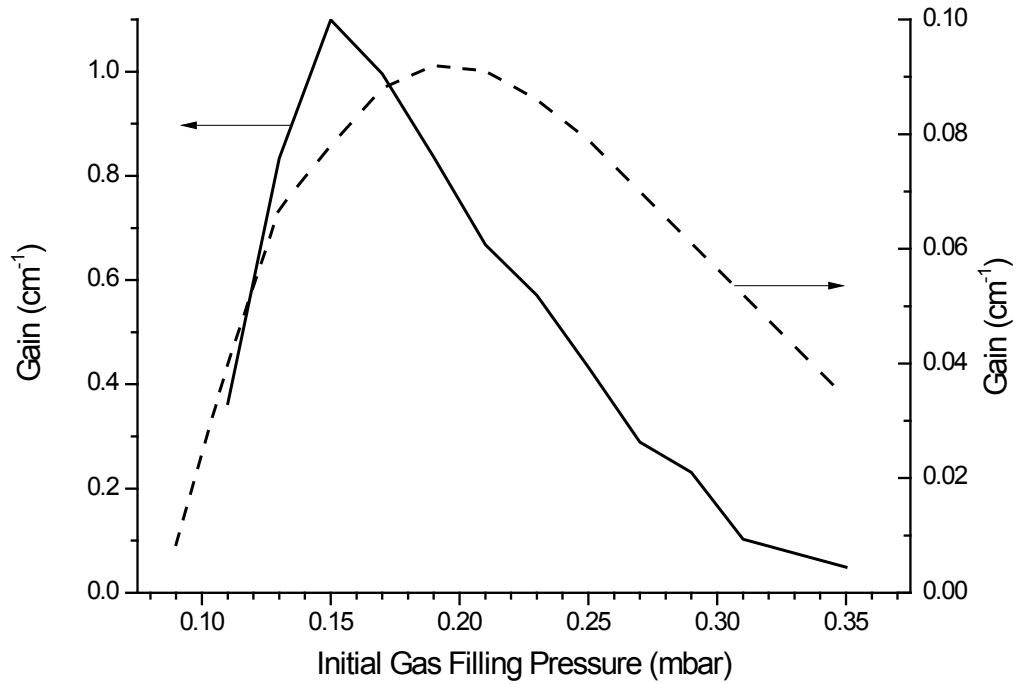


**Figure 4.5** Dependence of gain factor peak value with opacity effect included on the initial gas filling pressures for current peak of 13.5 kA (dashed line) and 19 kA (solid line).

The calculated pressure range for the peak current of 13.5 kA, which fulfill the electron profile (electron density of  $0.1 - 4 \times 10^{19} \text{ cm}^{-3}$ , and electron temperature  $\approx 40 - 90 \text{ eV}$ , as shown in Fig.3.3), is  $0.09 \text{ mbar} < p_0 < 0.23 \text{ mbar}$ , which compares favourably with  $0.10 \text{ mbar} < p_0 < 0.22 \text{ mbar}$  which was measured by Tan [18].

The calculated pressure range for the peak current of 19 kA, which fulfill the electron profile (electron density of  $0.1 - 4 \times 10^{19} \text{ cm}^{-3}$ , and electron temperature  $\approx 40 - 90 \text{ eV}$ , as shown in Fig.3.3), is  $0.17 \text{ mbar} < p_0 < 0.39 \text{ mbar}$ . Tan's experiment [18], measures the range of the pressure as  $0.14 \text{ mbar} < p_0 < 0.37 \text{ mbar}$ . Hence, the pressure ranges calculated from the simulations agree well with the experimental measurements.

To summarize, the initial gas filling pressures that seen to play an important role in determining the optimum electron parameters, i.e. electron density of  $0.1 - 4 \times 10^{19} \text{ cm}^{-3}$  and electron temperature  $\approx 40 - 90 \text{ eV}$ , required for lasing action.

In sections 4.1 and 4.2, the influence of initial gas filling pressures,  $p_0$  and of the electric current peak value,  $I_{max}$ , on the electron profiles have been studied. However, the rise time  $T_{1/4}$  and the size of the capillary radius  $r_0$ , were kept fixed in these two sections. Section 4.3 describes an experiment conducted at a high current peak value of 190 kA. We use the results obtained to motivate the optimization of the four parameters  $(p_0, I_{max}, T_{1/4}, r_0)$  at a high current of 100 kA, as discussed in section 4.4.

### 4.3 A High Current Experiment Study

There is great interest in the study of laser optimization schemes at high current peak values to sustain a more powerful laser output. However, this requires the generation of significantly hotter and denser plasma columns [50, 56], which in turn demands a substantial scaling up of excitation power density.

In Gonzalez's experiment [57], the plasma columns were generated utilizing current pulses with rise time of about 18 ns and peak amplitude of 190 kA. Utilizing this

discharge, Ar plasma columns were generated in capillaries of diameter 4 mm filled with 1.3 Torr of Ar gas. Time resolved soft x-ray spectra and pinhole images of the plasma were obtained. The paper also reported the experimental data and its comparison with model computations [56, 58, 59] which suggested that dense ( $> 1 \times 10^{20} \text{ cm}^{-3}$ ) argon plasma columns of 300  $\mu\text{m}$  diameter with electron temperatures  $>250 \text{ eV}$  had been generated.

The inputs ( $p_0 = 1.5 \text{ Torr}$ ,  $I_{\text{max}} = 190 \text{ kA}$ ,  $T_{1/4} = 18 \text{ ns}$ ,  $r_0 = 2 \text{ mm}$ ) from Gonzalez's experiment are used in the Helios-CR code to generate a higher degree of ionization than the required  $\text{Ar}^{8+}$ , as shown in Fig. 4.6. Plasma columns with maximum degree of ionization were of most interest to Gonzalez *et al* [57] for the development of shorter wavelength light. From Fig. 4.6 see that the  $3p \ ^1\text{S}_0 - 3s \ ^1\text{P}_1$  transition of Ne-like Ar at 46.9 nm cannot occur at during the pinch time. However, this transition should be detectable before the pinch time due to the high fraction of  $\text{Ar}^{8+}$  ions and high gain factor just before the pinch time.

On the other hand, it was found in the previous calculations from Helios-CR that the high current (Fig. 4.6a) results in a much larger shock-induced plasma temperature change, as it is natural to expect from the much larger amplitude and shorter duration of the current pulse, as compared with lower current (Fig. 3.4a). The depth of the layer in front of the hot dense shock is of the order of 100–200  $\mu\text{m}$  and is defined by the heat conductivity in the low density gas, and to a lesser extent by the process of electromagnetic field diffusion. Heat conduction enables a high electron temperature which results in the high degree of ionization observed.



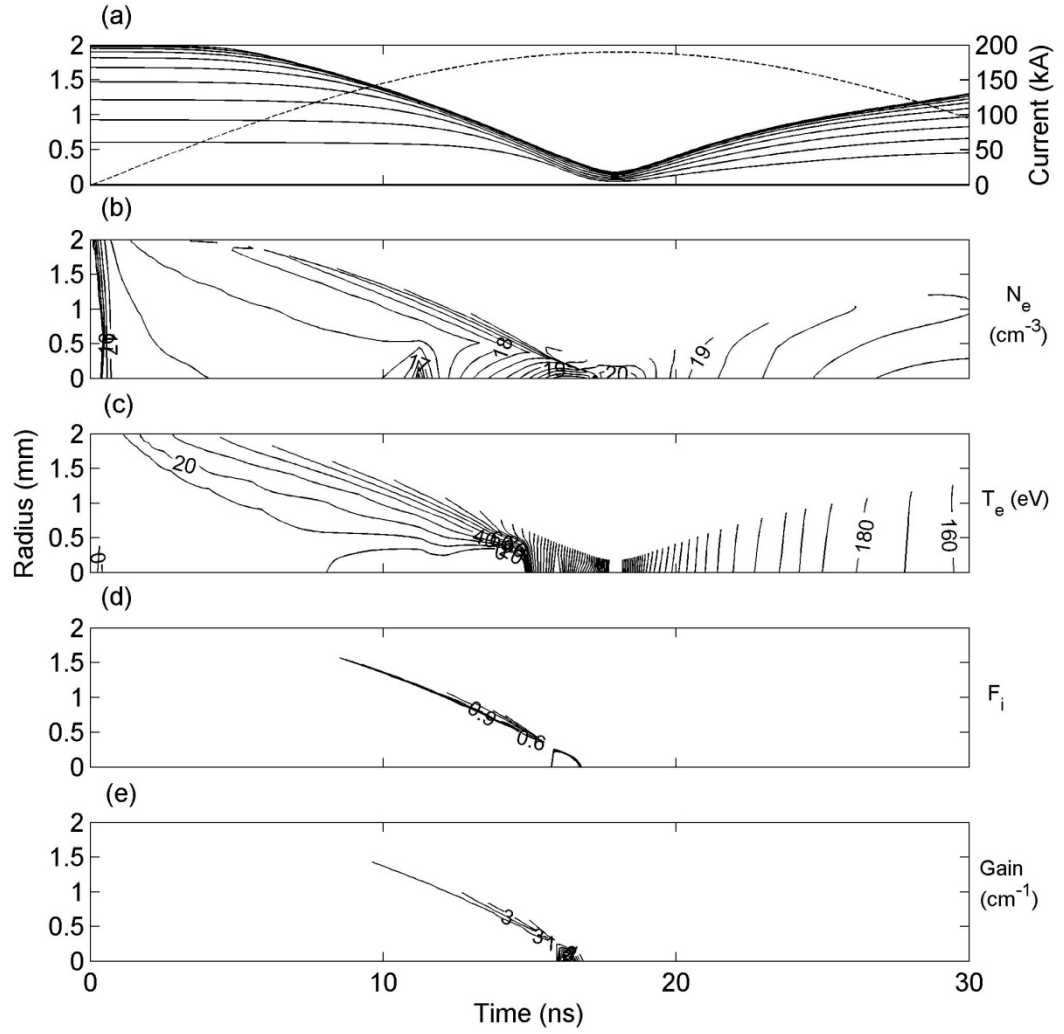


**Figure 4.6** Basic parameters of discharge in capillary with diameter of 4 mm filled with argon at a initial gas filling pressure of 1.3 Torr for  $I_0 = 190$  kA and rise time 18 ns. (a) The plasma time-space flow diagram; the dotted line corresponds to the discharge current at outer boundary; (b) contour lines of the decimal logarithm of the electron density (measured  $\text{cm}^{-3}$ ) on the  $(t, r)$  plane; (c) contour lines of the electron temperature (measured in eV); (d) contour lines of the fraction of ion  $\text{Ar}^{8+}$ ; (e) contour lines of the gain (measured  $\text{cm}^{-1}$ ).

Fig. 4.7 is the percentage of electric current which is normalized over 190 kA of peak discharge current inside the region of radius  $r$  and time  $t$ . More than 50% of the electric current at outermost region of the plasma was generated from 2 to 13 ns after the current flows into the capillary. At 6 ns after current flows, almost full (100%) electric current was detected at outermost region of the plasma. Also, when the heat wave and the magnetic wave arrive on axis, the maximum of the current density and

joule dissipation arrives at the centre of the capillary as in the Ne-like Ar soft-x-ray laser case. Quickly after that, within 1–2 ns, the front of the shock wave arrives to form the hot dense plasma column. Mass continues to be supplied, and after several more nanoseconds the plasma starts to cool due to expansion, radiation losses and current decay. The total current flowing inside the compressed plasma column is a small fraction, i.e. of the order of 1% of the total current at the center of the axis in Fig. 4.7.

However for 190 kA peak discharge current, the electron temperature  $T_{e,max}(t_G) = 250$  eV and electron density  $N_e(t_G) = 1.7 \times 10^{20} \text{ cm}^{-3}$  (in Fig. 4.6) generated at maximum compression during the pinch time, are beyond the optimum range of the electron profile (electron density of  $0.1 - 4 \times 10^{19} \text{ cm}^{-3}$ , and electron temperature  $\approx 40 - 90$  eV, as shown in Fig.3.3) making it difficult for lasing in Ne-like Ar with such conditions. Hence, due to this reason, it is reasonable to suggest that a combination of several factors including a smaller current, i.e. 100 kA, and some adjustment of pinch radius and other parameters might lead to option lasing conditions.

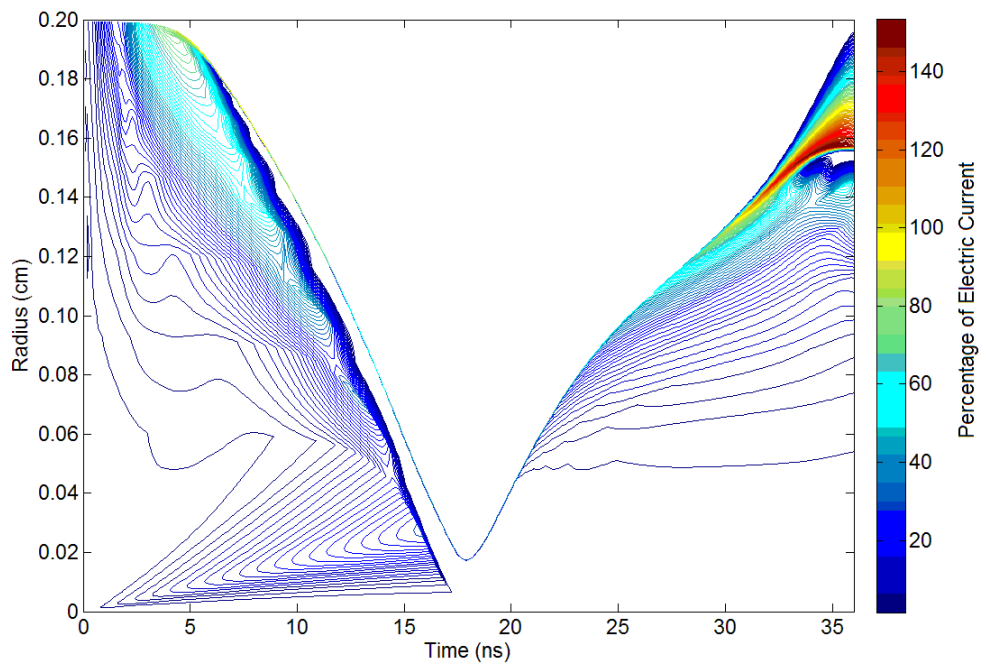


**Figure 4.7** Contour lines of the percentage of electric current (which normalized over 190 kA of peak discharge current) inside the region with radius  $r$  and time  $t$ .

#### 4.4 System Optimization Study of 100 kA Current Peak

The results of the experiment of Gonzalez *et al* [57] as discussed in section 4.3 motivates the suggestion of 100 kA peak current. The investigation of the plasma dynamics in capillary discharge involves many parameters, such as the initial radius  $r_0$ , the initial pressure  $p_0$ , and the current rise time  $T_{1/4}$ . With a high current peak, a larger inner capillary diameter is needed to yield a plasma column sufficient to deliver a higher energy of laser output. A total of 9 simulations at 100 kA peak current, with several current rise times from 50 ns to 100 ns, with varying capillary diameters from 6 mm to 10 mm at various gas filling pressures have been studied. The objective is to determine the optimum laser gain and the trends arising from each input.

Fig. 4.8 (a) shows that, all else being fixed at 100 kA peak current, 50 ns rise time and 6 mm capillary diameter, the pinch time  $t_p$  is tuned by the choice of the initial gas filling pressure  $p_0$ . Fig. 4.8 (b), (c) and (d) respectively show the values of electron density, electron temperature and gain with respect to the time of as a function of initial gas filling pressure. As the initial gas filling pressure is increased, the pinch time shifts gradually to later times and the pinch radius gradually increases; the electron density and electron temperature are decreasing if compared at the respective pinch time. Due to the high velocity compression, among all pressures  $p_0$ , the electron temperature abruptly increases to reach or surpass the optimal values for lasing (50 – 80 eV) as previously discussed in Chapter 3. Also, when the kinetic energy of the shock wave reaches the capillary axis, it causes an abrupt increase in the ion temperature. Overionization of the dense plasma, increased Doppler broadening, and collisional thermalization then result in a decrease in the gain, thus terminating the laser pulse [50].

Most of the maximum gains occur at 2 or 5 ns before the pinch time. The gain remains high if compared with the value of gain (about  $1 \text{ cm}^{-1}$ ) obtained in Chapter 3. This is because the high currents used here are higher than the low current employed in

Chapter 3. This means that there are more electrons than previously which cause more collision excitation processes to occur during the compression. Hence, larger numbers of electrons populate the upper laser level resulting in a larger population inversion.

However, the maximum gain values shown in Fig. 4.8 differ from the values obtained in Fig. 3.3. This is because the gain values shown in Fig. 3.3 were generated from the assumption of time independent collision radiative model and the values obtained can only serve as a guide for the lower limit of the gain. On the other hand, the gain shown in Fig 4.9 (d) was calculated by using time dependent collision radiative model.

From Fig. 4.8 (d), the maximum gain occurs at 2.0 mbar at which a pinch occurs at 65.5 ns with 923  $\mu\text{m}$  diameter of plasma column,  $5 \times 10^{19} \text{ cm}^{-3}$  electron density and 74 eV of electron temperature at the pinch time. The maximum gain occurs at 62 ns with the gain value of 4.16. The value of electron density and temperature during the gain maximum are  $2.42 \times 10^{19} \text{ cm}^{-3}$  and 71 eV.

Calculations [60] show that lowering of gas pressure will lead to a higher gain coefficient. This is because the reduced total gas mass enables compression to smaller volumes (in the radial direction), resulting in a hotter and dense plasma. The increase in temperature increases the pumping rate to the upper laser level, leading to increasing gain. However, this advantage is lost when the pressure is lowered below optimum. In this lower pressure regime, the electron temperature of the pinched plasma becomes too high and it will thermalize the population inversion built between the 3s-2p Ne-like Argon.

The duration of the gain is calculated from the full width half maximum of the gain value. As the capillary pressure increases, the duration of the gain becomes longer. This is because at lower capillary pressure, the plasma gets heated very fast and is unable to sustain the gain as compared to the case of higher capillary pressure.

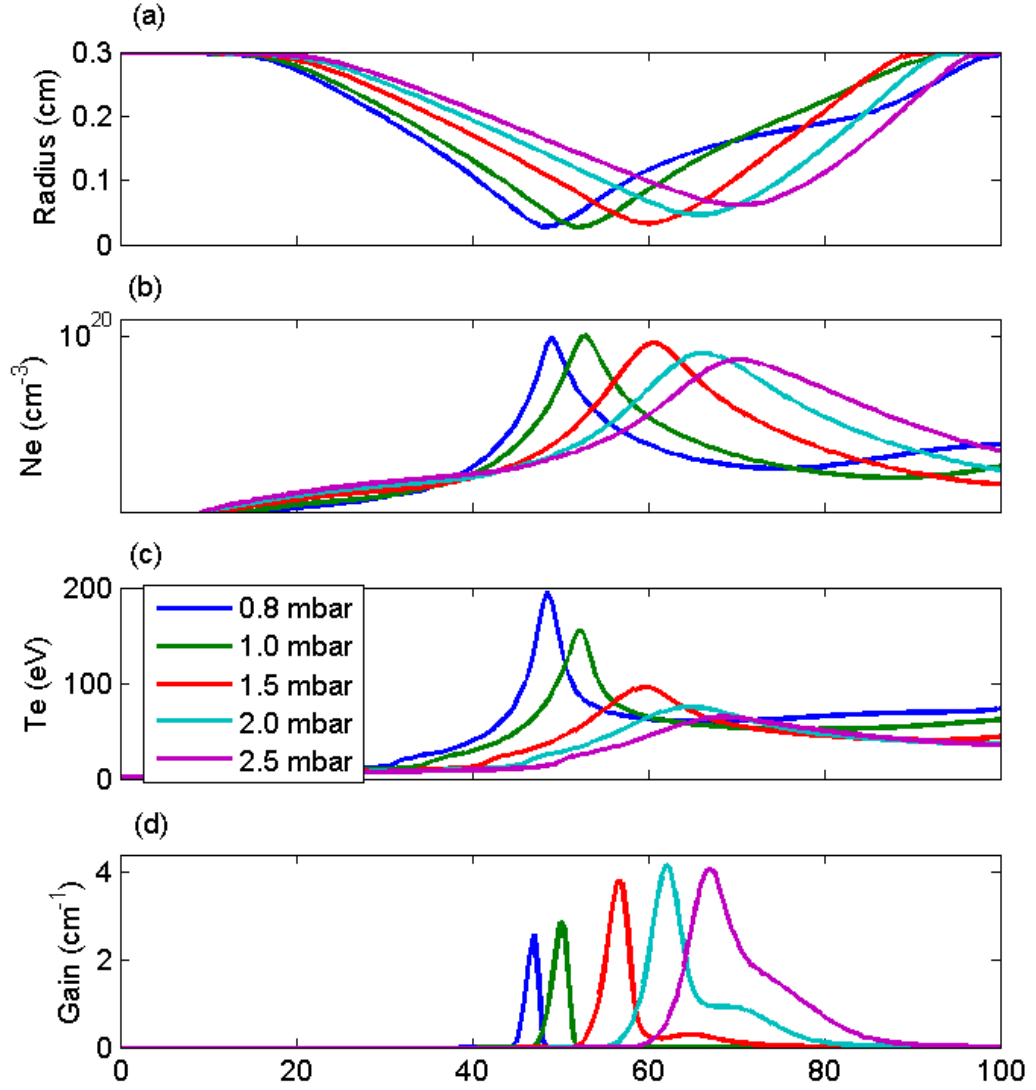


**Figure 4.8** (a) Radial motion of outer plasma mass elements, (b) Temporal evolution of electron temperature, (c) Temporal evolution of electron density (d) Temporal evolution of gain; for various initial gas filling pressures (in mbar) for 100 kA of current peak, 50 ns of current rise time and 6 mm of capillary diameter.

At a capillary pressure of 0.8 mbar, the pinch occurs around the peak of current, but the highest gain among the maximum gain of this configuration happens at capillary pressure of 2.0 mbar which the pinch occurs at 65.5 ns, that is 15.5 ns prior to the current peak. What happens if the rise time of peak current has been changed? Will the pinch occur much later? Will the highest gain among maximum gain happen at the pinch where the current is at its peak?

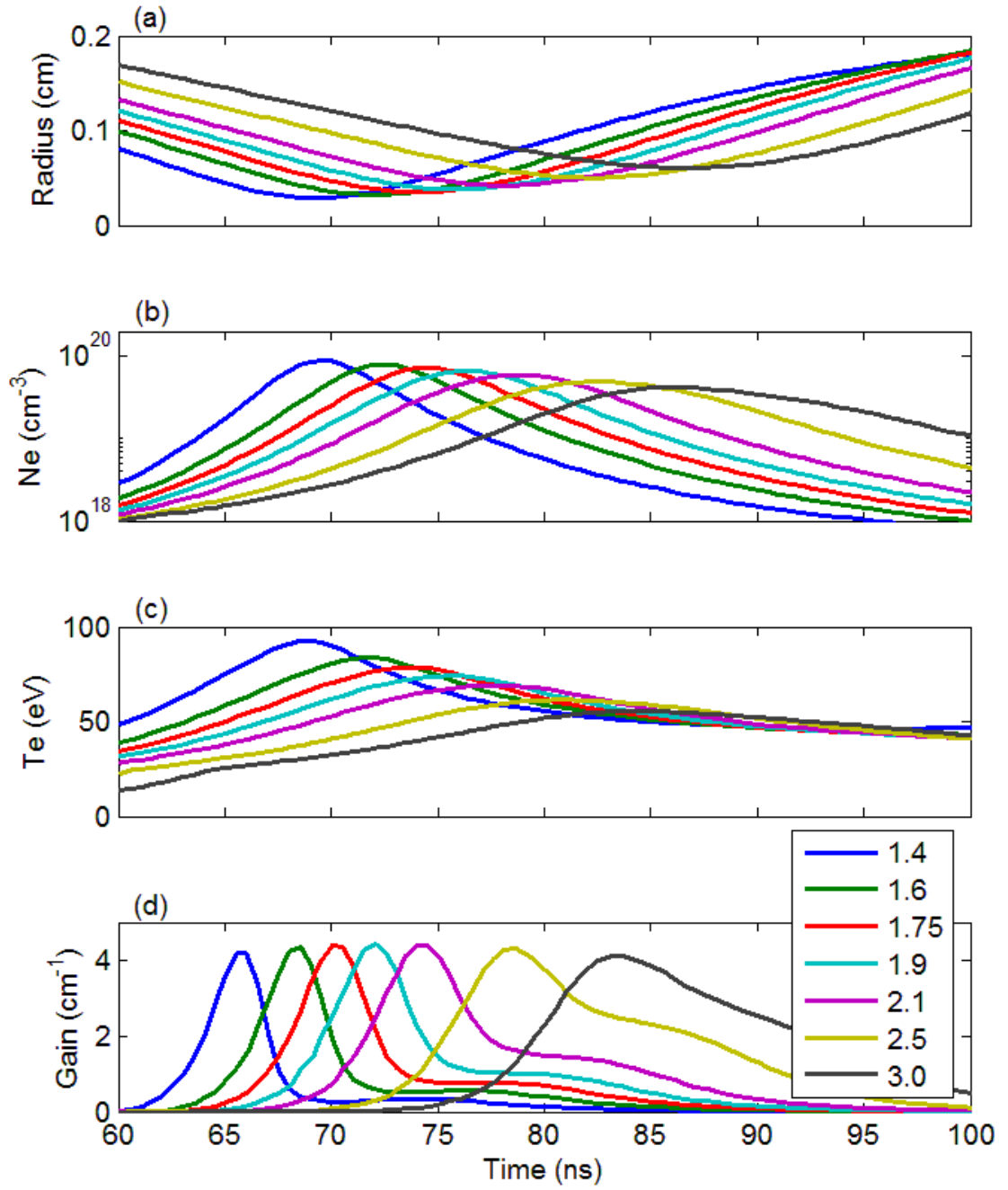
Fig. 4.9 and Fig 4.10 report the study of trend of the 75 ns and 100 ns current rise time, respectively. Fig. 4.9 shows the output parameter of the variation of initial gas filling pressure with fixed inputs of 100 kA peak current, rise time of 75 ns and the diameter of the capillary of 6 mm. At capillary pressure of 1.9 mbar, the pinch pinches at about the peak of current (75 ns) in this configuration and it gives the highest value among the maximum gain values. In fact, the maximum gain of initial gas filling pressure from 1.4 to 2.1 mbar are almost the same.

Fig. 4.10 shows the output parameter of the variation of initial gas filling pressure with fixed inputs of 100 kA peak current, rise time of 100 ns and the diameter of the capillary of 6 mm. At capillary pressure of 3.25 mbar, the pinch pinches at the peak of current, but the highest gain among the maximum gain of this configuration happens at capillary pressure of 2.5 mbar in which the pinch occurs at 93 ns, subsequent to the current peak which occurred 7 ns earlier.

From Fig. 4.8, Fig. 4.9 and Fig. 4.10, the inputs of 100 kA peak current and the diameter of the capillary of 6 mm remain unchanged, while the rise time of peak currents were changed from 50 ns to 75 ns and then to 100 ns. The Table 5.1 is shown the summary of the plasma output during the pinch at 2.5 mbar of the initial gas pressure.

**Table 4.1** The summary of the plasma output during the pinch at 2.5 mbar initial gas filling pressure, 100 kA peak current, 6mm capillary diameter and at the various current rise time.

Current Rise Time (in ns)	<b>50</b>	<b>75</b>	<b>100</b>
Pinch Time, $t_c$ (in ns)	70.5	82	93
Pinch Radius, $r_c$ (in $\mu\text{m}$ )	615	503	532
Electron Density, $N_{e,p}$ (in $\text{cm}^{-3}$ )	$4.0 \times 10^{19}$	$4.9 \times 10^{19}$	$4.2 \times 10^{19}$
Electron Temperature, $T_{e,p}$ (in eV)	63	61	55



**Figure 4.9** (a) Radial motion of outer plasma mass elements, (b) Temporal evolution of electron temperature, (c) Temporal evolution of electron density (d) Temporal evolution of gain; for various initial gas filling pressures (in mbar) for 100 kA of current peak, 75 ns of current rise time and 6 mm of capillary diameter.

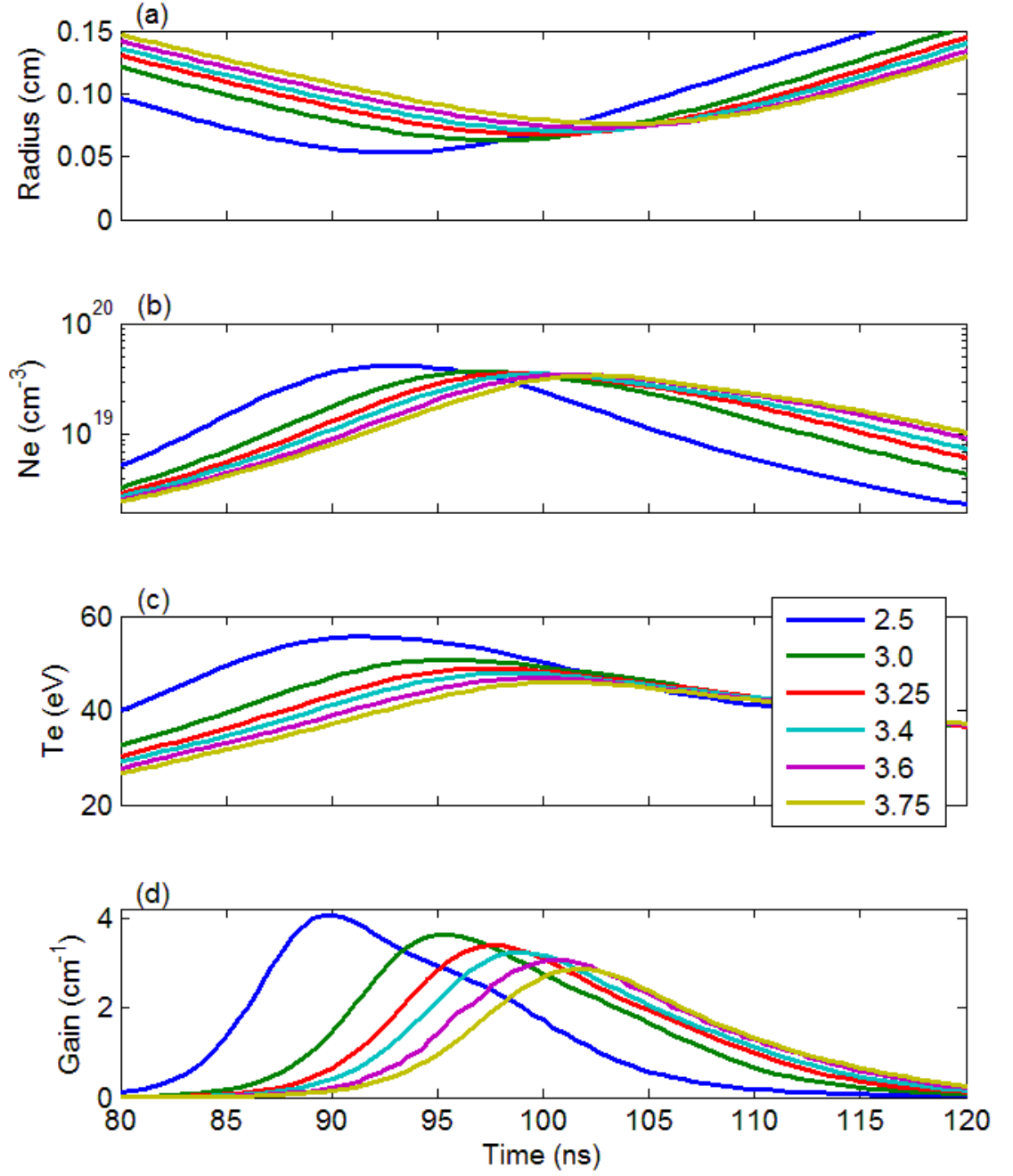


**Figure 4.10** (a) Radial motion of outer plasma mass elements, (b) Temporal evolution of electron temperature, (c) Temporal evolution of electron density (d) Temporal evolution of gain; for various initial gas filling pressures (in mbar) for 100 kA of current peak, 100 ns of current rise time and 6 mm of capillary diameter.

In the case of 100 kA discharge current, 6 mm capillary diameter, 75 ns rise time the maximum gain of  $4.2 \text{ cm}^{-1}$  appears to be insensitive to the gas filling pressure which ranged from  $1.4 \leq p_0 \leq 3.0 \text{ mbar}$  as shown in Fig.4.10 (d).



The system that fulfills the electron profiles (i.e., electron density of  $0.1 - 4 \times 10^{19} \text{ cm}^{-3}$ , and electron temperature  $\approx 40 - 90 \text{ eV}$ , as shown in Fig.3.3) required a rise time of 75 ns and 6 mm capillary diameter. In addition, the range of initial gas filling pressures that required for this simulation is  $1.4 \text{ mbar} < p_0 < 3.0 \text{ mbar}$ .

Next, what are the effects if the capillary diameter is varied? Fig. 4.11 shows the plasma parameters corresponding to the maximum gain of each configuration which Fig. 4.12 shows the gain values and the corresponding gas filling pressure of the capillary for each different configuration. 3 major sets of the capillary diameters, 6 mm (red colour), 8 mm (black colour) and 10 mm (blue colour), were shown in Fig. 4.11 and Fig. 4.12. In each major set, 3 different rise times, 50 ns, 75 ns and 100ns, were studied.

In Fig. 4.11, the rise time of 100 ns always give the highest electron densities and the narrowest range of electron temperatures (on the axis of capillary during the peak of gain) among same set of capillary diameters. Whereas the rise time of 50 ns always give the lowest electron densities and the widest range of electron temperatures (on the axis of capillary during the peak of gain) for same set of capillary diameters. The 6 mm capillary diameter (red colour) usually gave the higher electron densities and narrower range and smaller values of electron temperatures than the other capillary diameters. On the other hand, the 10 mm capillary diameter (blue colour) generally gave lower electron densities with wider range and bigger values of the electron temperatures as opposed to the other capillary diameters.

Fig. 4.12 shows that larger diameters of capillary (10 mm in blue colour) results in narrower ranges of initial gas filling pressure. However, smaller diameters of capillary (6 mm in red colour) gives wider ranges of initial gas filling pressure. The effect of changing the diameter of capillary (the channel radius  $r_0$ ) is not straightforward due to the difficulty in keeping the temperature steady during the radius parameter study. The equilibrium temperature can be estimated by the following simplified equation [61]:

$$\vec{\nabla} \cdot (k \vec{\nabla} T) = S_{\text{diss}}, \quad (4.1)$$

with  $k$  denoting the thermal conductivity and  $T$  the temperature.  $S_{\text{diss}}$  is the power dissipation density, which is given by

$$S_{\text{diss}} = \frac{J^2}{\sigma} \approx \frac{I_{\text{max}}^2}{\pi^2 r_0^2 \sigma}. \quad (4.2)$$

Here,  $\sigma$  is the electrical conductivity,  $J$  the current density,  $I_{\text{max}}$  the current and  $r_0$  the channel radius. In first order, the left hand side of (4.1) is proportional to  $r_0^{-2}$ . Thus, in order to keep  $T$  constant, the right hand side must have the same  $r_0$  dependence. Using (4.2),  $I_{\text{max}}$  should be varied proportional to  $r_0$  to achieve this [61]. However, this does not well describe the selection of input parameters such as initial gas filling pressure.

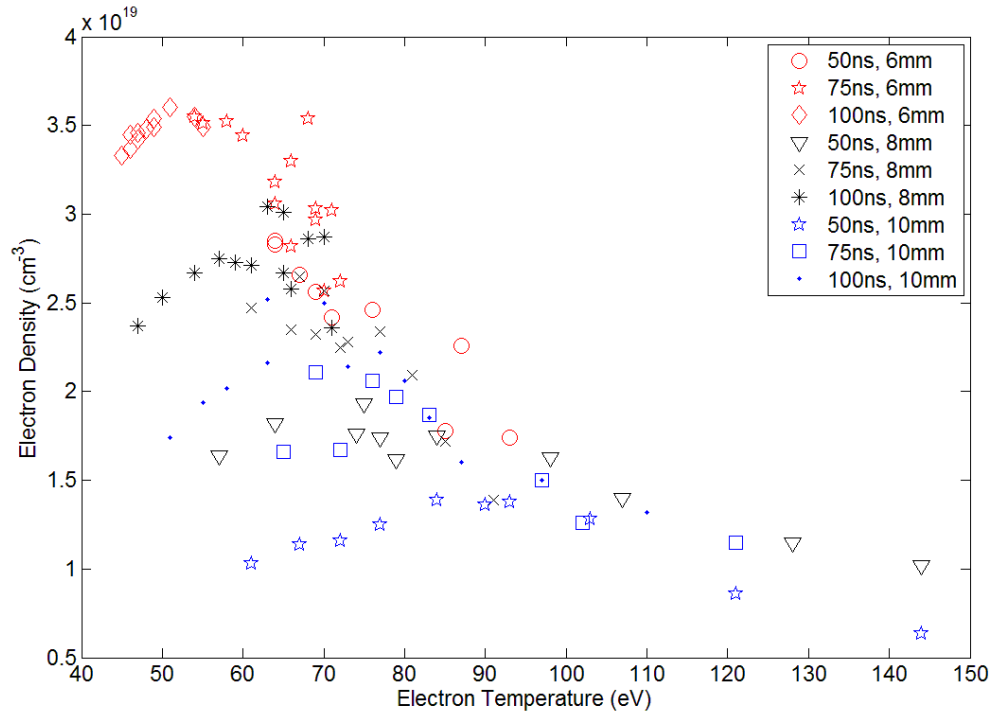


**Figure 4.11** Electron density and temperature at peak of the gain of each configuration.

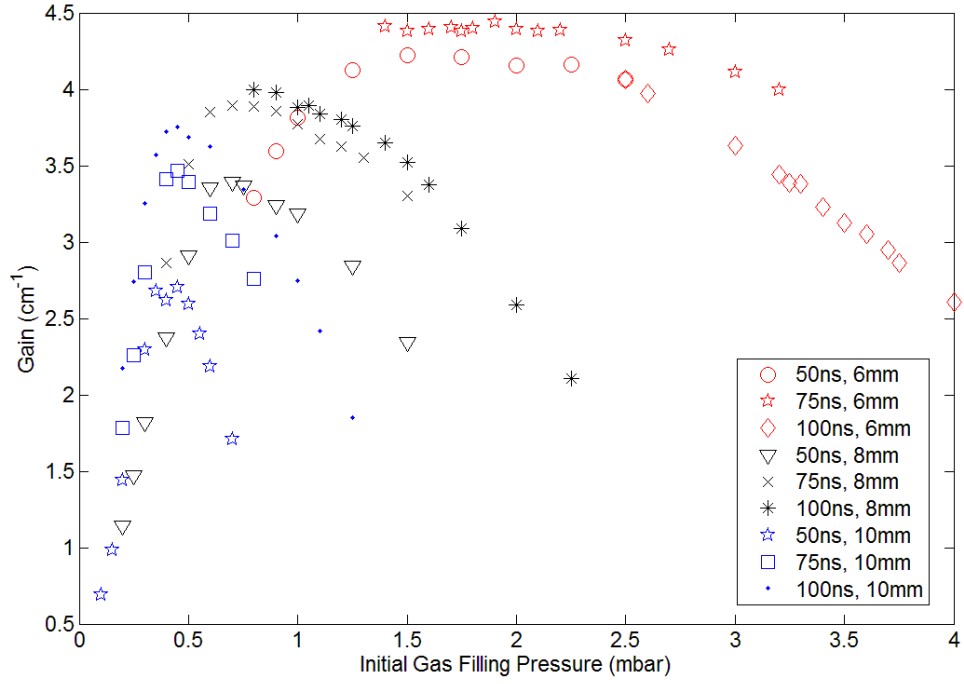


**Figure 4.12** The gain values versus initial gas filling pressure in each configuration.

Further, let us consider a cylindrical column of fully ionized quasineutral plasma, with an axial electric field, producing an axial current density,  $j$ , and associated azimuthal magnetic field,  $B$ . As the current flows through its own magnetic field, a pinch is generated with an inward radial force density of  $\mathbf{j} \times \mathbf{B}$ . In a steady state the balancing forces yield:

$$\bar{\nabla} p = \bar{\nabla} (p_e + p_i) = \mathbf{j} \times \mathbf{B}, \quad (4.3)$$

where  $\bar{\nabla} p$  is the magnetic pressure gradient,  $p_e$  ( $p_i$ ) is the electron (ion) pressure. Then from Maxwell's equation  $\nabla \times \mathbf{B} = \mu_0 \mathbf{j}$  and the ideal gas law  $p = N k T$ , we obtain the Bennett relation

$$2N_l k (T_e + T_i) = \frac{\mu_0}{4\pi} I_{\max}^2, \quad (4.4)$$

where  $N_l$  is the line density at the pinch,  $T_e$  ( $T_i$ ) is the electron (ion) temperature, and  $k$  is the Boltzmann constant. For simplicity, assume that  $T_e = T_i$  and substitute  $N_l = N r^2$  where  $N$  is the number of electrons per volume. Eq. (4.4) can be written as

$$4N_{e,p}r_p^2kT_{e,p} = \frac{\mu_0}{4\pi}I_0^2, \quad (4.5)$$

where subscript  $p$  indicate the values at the pinch. To fulfil the plasma condition, the approximate relations can be written as [56]:

$$N_{e,p}r_p^2 \simeq z^* N_0 r_0^2 = \text{constant}, \quad (4.6)$$

where  $z^*$  is the ion charge. For Ne-like Argon,  $z^* = 8$ . Then Eq. (4.6) can be rewritten as:

$$z^* T_{e,p} \sim \frac{I_{\max}^2}{N_0 r_0^2}. \quad (4.7)$$

The velocity of the shock wave inside the channel can be estimated to be of the order of the Alfvén velocity [62],

$$v_A = \frac{B}{(4\pi\rho_0)^{1/2}}, \quad (4.8)$$

with the magnetic field  $B = \mu I_{\max}/2\pi r_0$  and  $\rho_0 = MN_0/N_A$  where  $M$  is atomic mass and  $N_A$  is the Avogadro constant. Assuming the characteristic time for compression,  $t_c = r_0/v_A$ , we obtain the relation,

$$T_{1/4} = t_c = \frac{2\pi r_0^2 \sqrt{\pi MN_0/N_A}}{\mu I_{\max}}. \quad (4.9)$$

From Eq. (4.6), (4.7) and (4.9), the rough estimation of input parameters of  $I_{\max}$ ,  $T_{1/4}$ ,  $r_0$  and  $p_0$  can be set to obtain the values of  $r_p, N_{e,p}$  as the required plasma parameters.

Consider 100 kA of current as one of the input parameters. From Fig. 4.12, an increase of  $r_0$  decrease the role of dissipative effects decrease (Eq. (4.2)). To maintain the electron temperature within the required range, the range of initial pressure becomes narrower and its values become smaller. However, if  $r_0$  decreases, the initial pressure range becomes wider and the values of pressure have to be bigger (Eq. (4.7)). This is

because the effect of change of radius is faster than the changes of the initial pressure to maintain the electron temperature and the current. The rise time of the current can be estimated in Eq. (4.9). Here, it has been assumed that the pinch always compresses during the peak of the current. To conclude, for each set of initial conditions  $p_0$ ,  $r_0$ ,  $I_{max}$  and  $T_{1/4}$ , the various values of  $r_p$  and  $N_{e,p}$  can be obtained so as to coincide with the plasma conditions that are required.

Hence, in the case 100 kA discharge current, a high gain output can be expected from each capillary diameter and the current rise time. The range of initial gas filling pressures is suggested in this simulation that fulfills the plasma conditions (i.e., electron density of  $0.1 - 4 \times 10^{19} \text{ cm}^{-3}$ , and electron temperature  $\approx 40 - 90 \text{ eV}$ , as shown in Fig.3.3) are shown in Table 5.2.

**Table 4.2** Suggestion of range for the initial gas filling pressures in each capillary diameter.

Capillary Diameter (mm)	<b>6</b>	<b>8</b>	<b>10</b>
Current rise time which high gain output expected (ns)	75	100	100
Initial gas filling pressure which high gain output expected (mbar)	1.9	0.8	0.5
Suggested range for the initial gas filling pressure which fulfills the plasma condition (mbar)	1.4 – 3.0	0.8 – 2.25	0.3 – 1.25

As a summary, the electron profiles (electron density of  $0.1 - 4 \times 10^{19} \text{ cm}^{-3}$ , and electron temperature  $\approx 40 - 90 \text{ eV}$ , as shown in Fig.3.3) were playing role to determine the range of initial gas filling pressure. In order to simulate the profile of the laser intensity for the experiment, the gain still remain as one of the main factors. But not all light beams are amplified and are detected into the CCD signal. Refraction effect due to high electron density gradients around the time of lasing may play a vital role in the amplification process of the laser beam. This factor has been taken into the account in next chapter.

## Chapter 5

### Modelling of Capillary Discharge X-ray Image Output

#### Using a Ray-tracing Code

In the capillary discharge scheme a fast current pulse rapidly separates the plasma column from the capillary walls and compresses it, creating a high temperature plasma column of small diameter and cylindrical symmetry which has been studied in the previous chapters. Under certain plasma conditions (electron density of  $0.1 - 4 \times 10^{19} \text{ cm}^{-3}$ , and electron temperature  $\sim 40 - 90 \text{ eV}$ , as shown in Fig.3.3) the fast capillary-discharge generates amplification of the  $J = 0 - 1$  soft x-ray line of neon-like argon at 46.9 nm.

Soft x-ray lasers have small lateral dimensions in high-density plasmas, resulting in electron density gradients which cause refraction effects to the amplified x-ray radiation. This refraction is responsible for strong optical losses and for a beam intensity distribution dominated by characteristic side lobes with large divergence.

The index of refraction is related to the electron density  $n_e$  through [63]

$$\eta = \sqrt{1 - \frac{n_e}{n_c}}, \quad (5.1)$$

where the critical electron density  $n_c$  is defined as

$$n_c = \frac{4\pi^2 \epsilon_0 m_e c^2}{e^2 \lambda^2} = 5 \times 10^{23} \text{ cm}^{-3}, \text{ (in c.g.s unist)} \quad (5.2)$$

which  $c$  as the speed of light. Here,  $\lambda$  is the laser wavelength of 46.9 nm.

Some previous works describe the beam propagation and amplification in a plasma with various electron densities distributions. London [64] in 1988 analyzed the propagation and amplification of exploding foil x-ray lasers. An analytical 3-dimensional model was approximated to treat parabolic density and gain profile were

calculated along the ray trajectories. The model was later extended to treat constant and quartic gain profile beam patterns. London [64] concluded that the model with parabolic density and gain profile does not agree qualitatively with the experimental data. However, the pattern from a quartic gain profile having a dip in the center of the plasma can produce a profile with off-axis peaks, in better agreement with the experimental data. In addition, the main observed features can be reproduced with a parabolic density profile and a quartic gain profile.

Subsequently, Fill [65] also studied the beam propagation of a ray within a plasma with a density gradient. His analysis has been limited in two dimensions, using Cartesian or cylindrical geometry. Linear, quadratic, exponential, and Gaussian electron density distributions have been considered for plane and curved targets, in which exact solutions of paraxial-ray equations have been derived and have been compared with numerical solutions. Rocca *et al.* [66] used the model and the solution of the parabolic density profile, derived and simplified by London [64], to estimate the electron density in the gain region of a discharge-driven soft x-ray laser. Chilla and Rocca [67] studied the beam optics of a capillary discharge, which has been described by a model with a one-dimensional density gradient, assuming parabolic density profile.

In this chapter, the analysis of the soft x-ray beam propagation and amplification in a plasma of cylindrical geometry for arbitrary gain and density profiles has been studied by using Matlab software (Appendix B). The characteristics of the laser beam intensity distribution of highly saturated capillary discharge 46.9 nm soft x-ray laser are reported. By measuring, in different simulated conditions, the far field intensity distribution of laser beam produced in the elongated capillary channels, an amplification regime has been obtained. The features of laser amplification in the plasma column will be analyzed by comparing the experimental results with theoretical simulations based on two-dimensional ray-tracing code.

## 5.1 Ray Trajectories And Formalism

The ray propagation equation is satisfied the rays propagating across the plasma column [68]:

$$\frac{d}{ds} \left( \eta \frac{d\vec{r}}{ds} \right) = \vec{\nabla} \eta, \quad (5.3)$$

where  $s$  is the arc length of the ray trajectory and  $\eta$  denotes the local refractive index. This ray propagation equation can be solved as a function of path,  $s$ , defined by the cylindrical coordinates,  $r$  is position of the ray in radial direction measured from the centre of capillary axis,  $\theta$  is the angular position of the ray and  $z$  is the capillary length, as shown in Fig. 5.1.

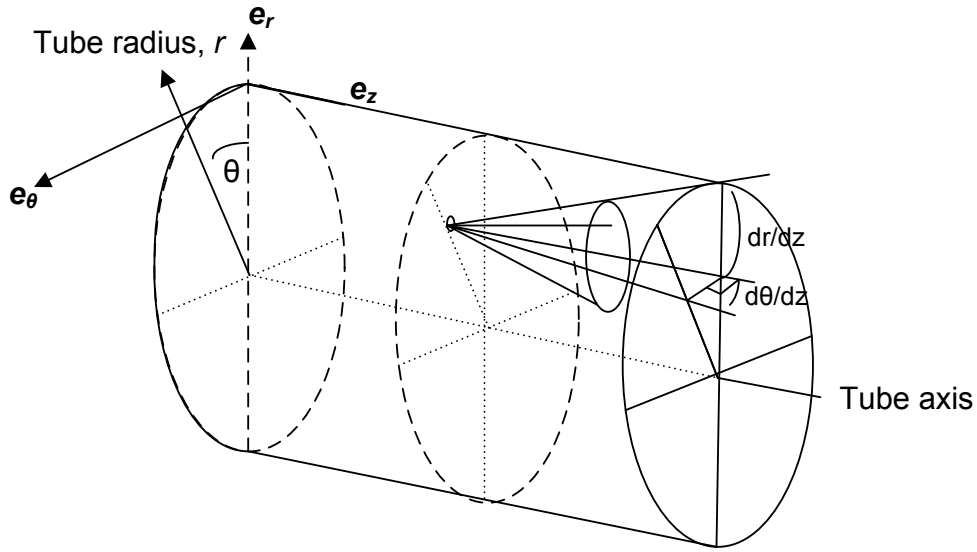


**Figure 5.1** Coordinate definitions for a cylindrical geometry

The paraxial approximation is used, i.e. the angle between the ray and the tube axis is sufficiently small that ( $ds \sim dz$ ). Rays can be launched randomly within certain angles. Rays with too large initial angle will quickly escape from the plasma region and do not contribute to the light emission from the exit plane of the capillary. Also, due to 1-D (radial direction) MHD model which has been studied in previous chapter, the



refractive index is changing only along the radial direction ( $\partial\eta/\partial\theta = 0$  and  $\partial\eta/\partial z = 0$ ), which leads to

$$\frac{d^2 r}{dz^2} = \frac{d}{dr} \ln(\eta), \quad (5.4)$$

$$\frac{dr}{dz} \frac{d\theta}{dz} + r \frac{d^2 \theta}{dz^2} = 0. \quad (5.5)$$

The set of differential equations (Eq. (5.4) and (5.5)) to calculate a particular ray trajectory, have to be solved until the ray exits the plasma. A system with the first order differential equations of Eq. (5.4) and (5.5) can be expressed as,

$$\begin{aligned} \frac{dr'}{dz} &= \frac{1}{\eta} \frac{d}{dr} \eta(r), & \frac{d\theta}{dz} &= -\frac{1}{r} r' \theta', \\ \frac{dr}{dz} &= r', & \frac{d\theta}{dz} &= \theta', \end{aligned} \quad (5.6)$$

which can be numerically solved using the Runge-Kutta method. Considering only the rays with a small angle with the axis ( $ds \sim dz$ ),  $r'$  is the angle between the tangent to the ray and the tube axis in the plane ( $\mathbf{e}_z, \mathbf{e}_r$ ). In the same way,  $\theta'$  is the angle between the tangent to the ray and the tube axis in the plane ( $\mathbf{e}_z, \mathbf{e}_\theta$ ) (Fig. 5.1).

A large number of rays have to be considered to represent the profile for the intensity emitted by the plasma, with  $z$ ,  $r$ , and  $\theta$ . The maximum angle for  $\theta'$  and  $r'$  defines an emission cone are limited by the initial position ( $r_0, \theta_0$ ). These initial values are obtained by taking uniformly distributed random numbers. The angles of emission  $\theta'$  are limited to a range of a few milli-rad and this is because the ratio of length of capillary and the size of radius of capillary is always  $>100:1$ . This number is critical to produce an intense beam laser [19]. The initial radial position  $r$  can vary from 0 to  $R_{\text{tube}}$  (radius of emitted plasma), the initial longitudinal position  $Z$  from 0 to  $Z_{\text{tube}}$  (the length of capillary) and initial angle  $\theta$  ranges from 0 to  $2\pi$ .

Finally the propagation of the ray is calculated using Eq. (5.6). This simulation has to be performed for over  $10^6$  rays where have been distributed uniformly in  $1000 \times 1000$  rays in the x-y plane to model refractive effects. In order to verify the accuracy, a ray-tracing code has been developed. The code was tested against the result of Girard [69].

The electron density for the plasma was given [69] by

$$n_e(r) = \frac{n_0}{2} \left( e^{-((r-r_0)/a)^2} + e^{-((r+r_0)/a)^2} \right) \quad (5.7)$$

where  $n_0$  is the maximum density,  $a$  is the profile width and  $r_0$  is the Gaussian central radius with  $n_0 = 10^{26} \text{ m}^{-3}$ ,  $r_0 = a = 3 \times 10^{-4} \text{ m}$  as shown in Fig. 5.2. Here, the electron density profile shows a dip in the centre of the axis.

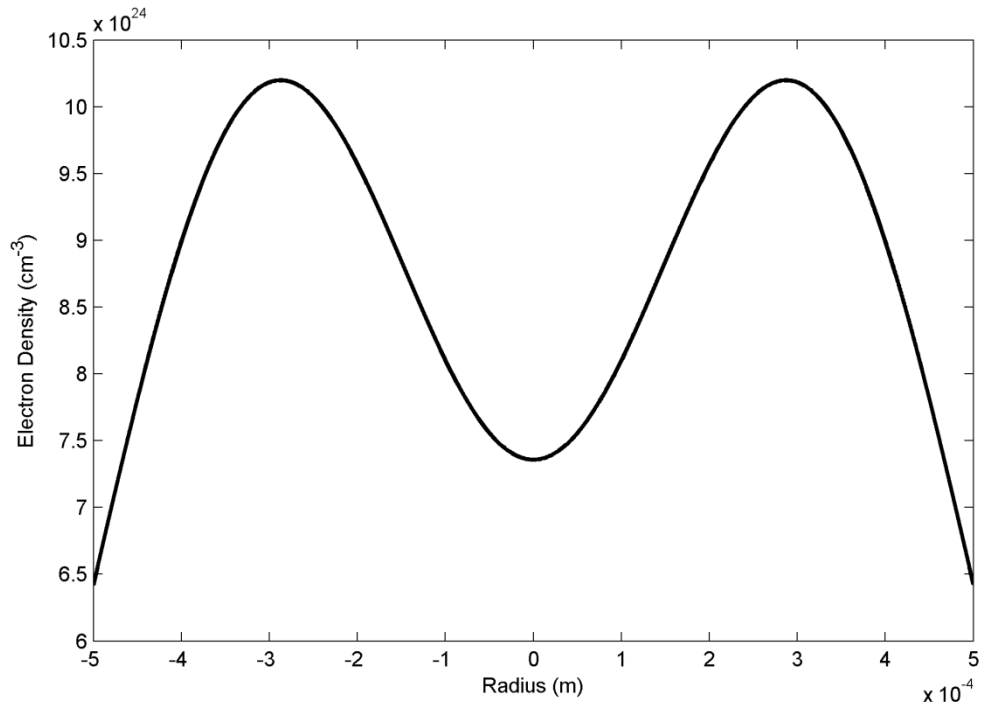


**Figure 5.2** Electron profile from Eq. (5.7).

Fig.5.3 shows some typical ray trajectories which have been generated using the ray-tracing program for the electron density profile according to Eq. (5.7) or Fig. 5.2. The capillary tube was 60 cm long with a diameter of 1 mm following Girard [69]. Each

launched point had 3 randomly chosen launch angles,  $\theta'$ , i.e 1, 0 and -1 mrad. These are denoted by the upper, middle and lower line in each of the launch points in Fig. 5.3. It can be observed that refraction bended the rays in a direction opposite to the direction of the electron density gradient. The effects of refraction are significant for plasmas at high electron densities and high gradients. Rays launched within the hollow of the electron density and at small angles ( $\theta'$  in between -1 to 1 mrad), would remain within the 'hollow' region.

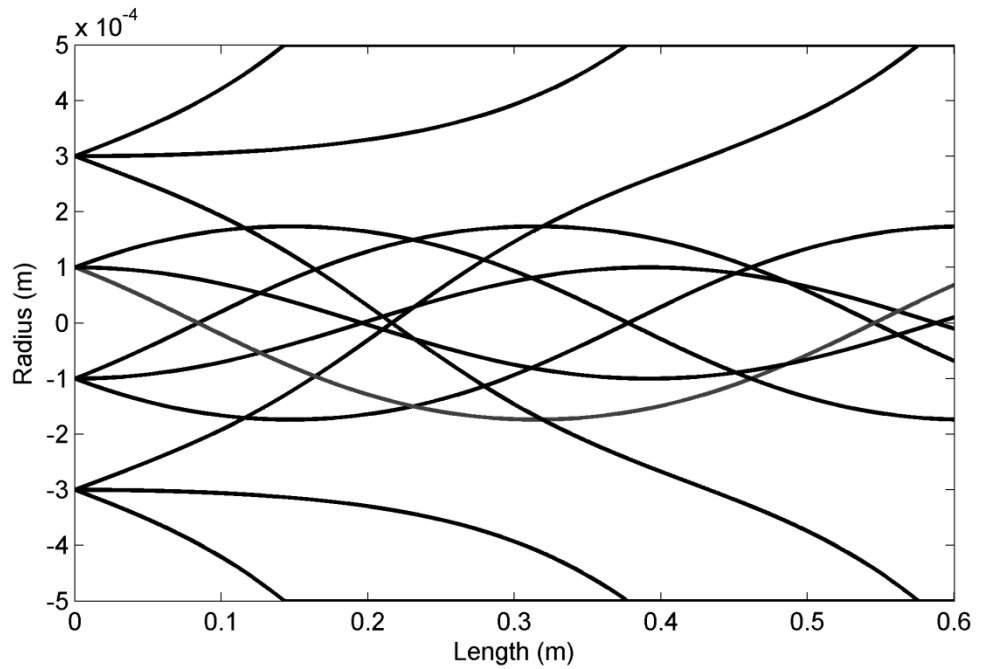


**Figure 5.3** Ray trajectories obtained from the electron profile, Eq. (5.7).

During propagation within the plasma, each ray would be positioned at its own  $r$ ,  $\theta$ ,  $r'$  and  $\theta'$  at every step size of  $z$  due to the effect of the electron density gradient. When the rays exit the plasma at the end of the capillary, with no more influence from the electron density gradient, the ray would just move along a straight line according to last values of  $r'$  and  $\theta'$ .

However, in imaging of soft x-ray laser, the generation of laser intensity is an important calculation to predict the output of the experiments. The electron density

gradient and the gain profile have always to be taken into account in the evaluation of the laser intensity.

## 5.2 Geometry of Code

The ray tracing Matlab code developed in Appendix A is to calculate the ray trajectories and laser intensities along the three axes, i.e in  $r$ ,  $\theta$  and  $z$  direction. This ray tracing code works as a post-processor to the Helios-CR MHD code which gives the temporal and spatial evolution of the gain, the electron density and plasma width in the radial direction.

Fig. 5.4 depicts the code geometry. The initial rays are launched on an equally spaced grid in the first cell, consisting of  $1000 \times 1000$  rays in the x-y plane. The values of  $r_0$  and  $\theta_0$  corresponding to each grid point is determined and the range of  $r'$  and  $\theta'$  are identified. Subsequent position of the rays for every step size of  $z$  are numerically solved using the Runge-Kutta method.

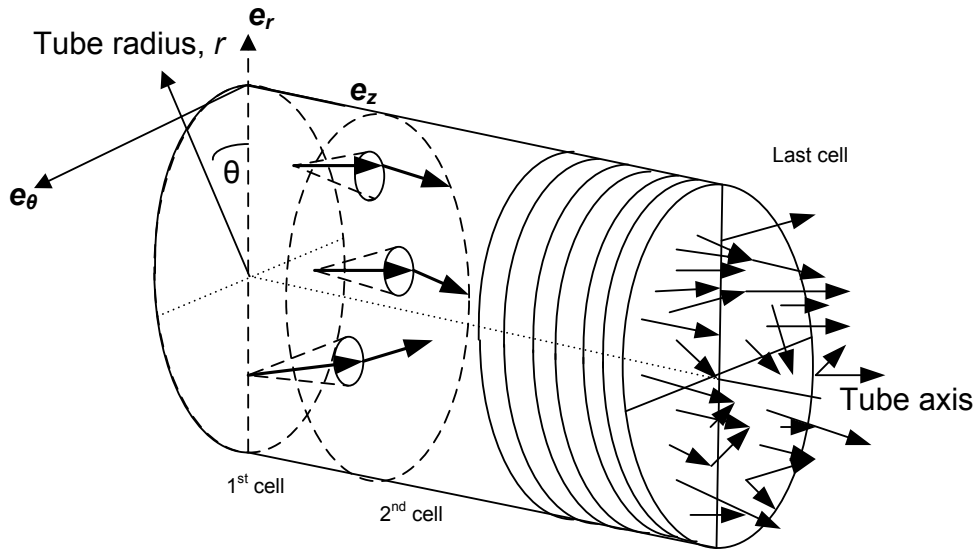


**Figure 5.4** The geometry of the code. The plasma is divided into cells along the propagation axis.

The intensity is amplified as the ray propagates through the gain regions. The amplifying formula is [70]

$$I = \frac{j}{g} (e^{g_0 \Delta z} - 1), \quad (5.8)$$

where  $g_0$  is small-signal gain,  $\Delta z$  is the ray path in each cell and  $j$  is the plasma emissivity. Eq. (5.8) is valid in the first cell only, where the rays are launched. The emissivity  $j$  is generally assumed to be homogeneous along the  $z$ -axis [70]. Hence,

$$j = N_u h\nu_0 \frac{r^2}{4\pi (\Delta z)^2} A_{ul}. \quad (5.9)$$

The emissivity depends on the population of the upper level  $N_u$ , the laser photon energy  $h\nu_0$ , the radius  $r$  of the region, and the Einstein coefficient for spontaneous emission  $A_{ul}$  between the two lasing levels. The emission is then amplified along the trajectory [71] via:

$$I(z + \Delta z) = \left( \frac{z}{z + \Delta z} \right)^{1/2} e^{g(z)\Delta z} I(z) \quad (5.10)$$

where  $I(z)$  and  $g(z)$  represent the ray intensity and the gain profile, respectively, along the ray trajectory. The gain profile is

$$g(z) = \frac{g_0}{1 + \frac{I(z)}{I_{sat}}}, \quad (5.11)$$

where  $I_{sat}$  is the value of the saturation intensity. For efficient extraction of the energy stored in the laser medium it is desirable to operate in conditions such as to saturate the gain. The saturation is commonly quantified in the x-ray laser literature in terms of the gain-length product necessary for saturation of the gain medium. This parameter is highly dependent on the geometry of the plasma column and on the effects of refraction. The saturation intensity depends only on a few basic atomic parameters [72]. Here,

$$I_{sat} = \frac{(A_u \times h\nu)}{\sigma_{stim}}, \quad (5.12)$$

where  $A_u$  is the total upper laser level depopulation rate,  $h\nu$  is the laser photon energy and  $\sigma_{stim}$  is the stimulated emission cross section. Atomic model calculations [3] of gain saturation for the 46.9 nm line of Ne-like Ar give  $\sigma_{stim} \sim 7.8 \times 10^{-15} \text{ cm}^2$  and  $A_u \sim 1.3 \times 10^{11} \text{ s}^{-1}$  and with these the saturation intensity is  $I_{sat} \sim 6.8 \times 10^7 \text{ W/cm}^2$ .

The model is used to simulate the performance of a pinhole imaging system by only transmitting the rays falling on the pinhole and then calculating intensity distribution on a detector plane placed at a chosen distance away from the pinhole. The modelled detector is a grid of cells similar in size as the pixels of the CCD, and the number of rays striking each pixel of the detector is counted. The grid pitch is adjusted to get good statistics on the counts. The intensity distribution on the detector can be displayed as a contour plot, or as radial intensity profiles by making a plot of the counts in each of the pixels on a straight line passing through the centre of the detector.

### 5.3 Numerical Results and Discussion

The electron density profile considered in section 5.1 was generated by an analytic expression, Eq. (5.7). However, in the following discussion, the electron density profile follows Fig. 5.5 which was generated from the dynamics of the capillary plasma column previously discussed in chapter 3. The measurements discussed below were conducted using 20 cm long capillaries of 3 mm diameter filled with 0.15 mbar of pure argon gas, excited by a current pulse of 16 kA peak current having a first half cycle duration of about 50 ns at the maximum compression of the plasma.

To illustrate the operation of the ray-tracing program, Fig. 5.6 shows ray trajectories launched from an arbitrary point  $4 \times 10^{-3} \text{ cm}$  from the axis along various angles. The rays encounter the electron density profile during propagation. And, the

simulated calculation in Fig 5.6 has been extrapolated to the capillary length of 20 cm in order to show the refraction effects. In Fig. 5.5, the electron density profile is concentrated in between -0.26 mm to 0.26 mm and electron density profile is symmetrical along radial direction. When the rays are launched at angles of 1 and 2 mrad, the rays quickly escape from the plasma region. On the other hand, rays launched at 0, -1 and -2 mrad are refracted within the region of -0.26 mm to 0.26mm which is also the high electron density gradient region.

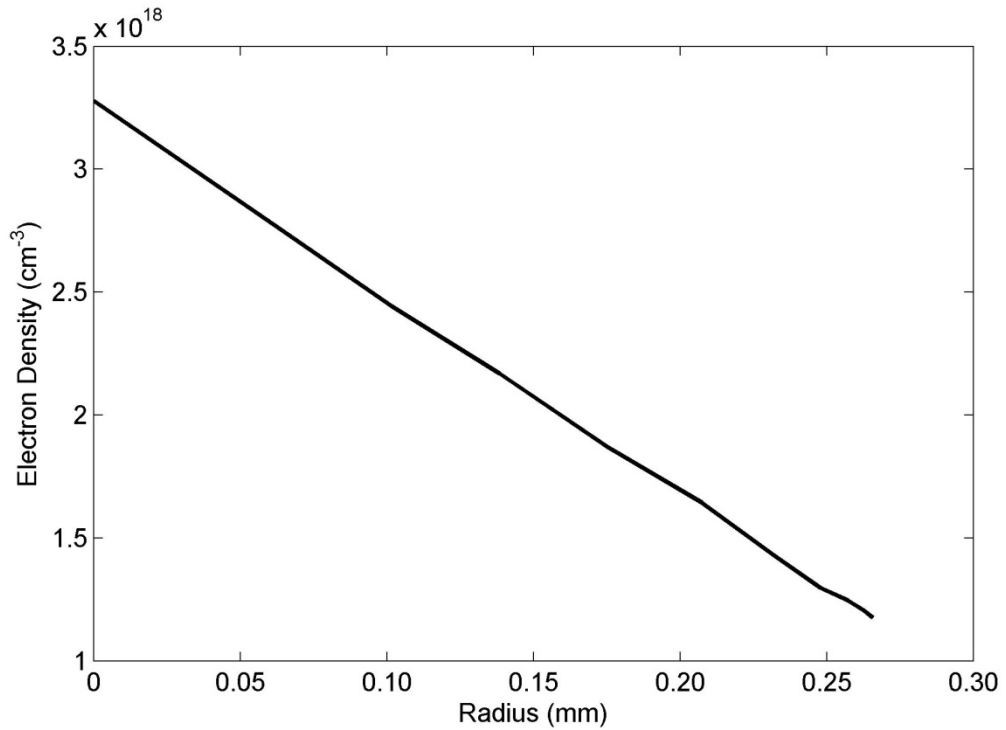


**Figure 5.5** Electron density profile at maximum compression by current pulse of 16 kA peak current having rise time about 50 ns with 20 cm long capillaries of 3 mm diameter filled with 0.15 mbar of pure argon gas.

The range of initial launch angle is determined by the size of plasma column, see Fig. 5.7. If the full diameter of the capillary is considered, the maximum range of the launch angle would be 15 mrad. However, the range of initial launch angle will be reduced due to the diminished radius of plasma column. So, in the case of electron density profile in Fig. 5.5, the size of plasma is 0.026 cm and the length of the capillary

is 20 cm. Hence, the maximum range of the launch angle is restricted to 2.6 mrad. Due to the complexity of the effect of refraction, twice the width of the initial launched angle is used to minimize the rays missing out from the region of high electron density profile. Hence, we use a 4 mrad range of initial launch angle.

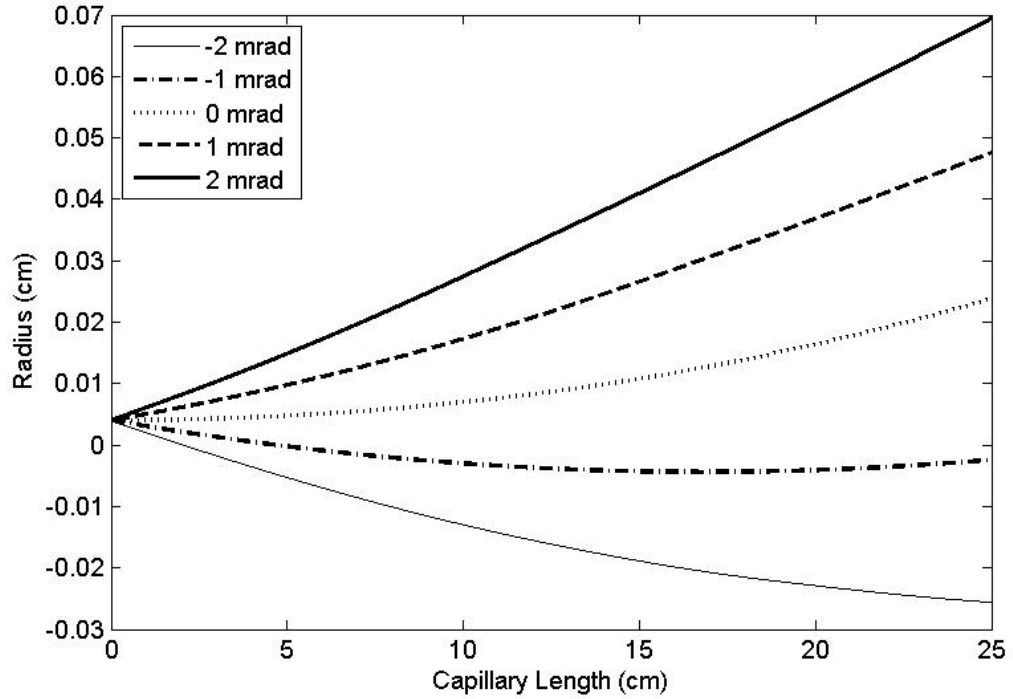


**Figure 5.6** Ray trajectories with simulated electron density profile for propagation along  $z$  at the initial point of  $4 \times 10^{-3}$  cm at various launching angles.

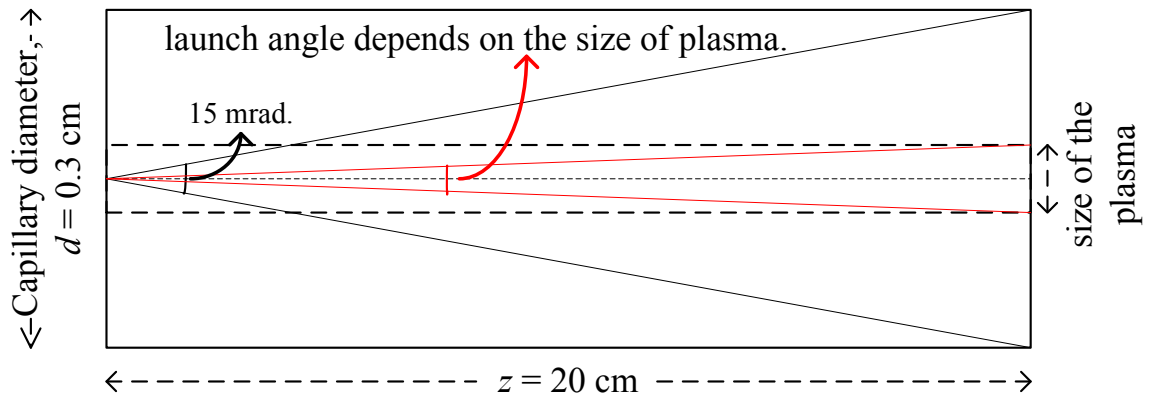


**Figure 5.7** Determination of initial launch angle.



Also, since the high gain region is focused between -0.26 to 0.26 mm in Fig. 5.8, the gain drops tremendously once the rays propagate out of this region. For example, the ray launched at an angle of 2 mrad is saturated much earlier than other rays in Fig. 5.9, resulting in a much lower intensity. The intensity also gets saturated after traversing 8 cm along the length of the capillary beyond which the ray exits the plasma column. Note that the intensity of the ray launched at 1 mrad is similar to the intensity of the ray launched at 2 mrad, but the ray's intensity is slightly higher than the ray launched at 2 mrad. This is because the ray launched at 1 mrad remains in the region of high gain longer than the ray launched at 2 mrad. The intensities of the rays launched at 0 and -1 mrad are about the same with the intensity of the ray without refraction effects. This implies that the rays do not experience refraction effects after propagating down the 20 cm long capillary and the rays largely remain within the high gain region. For the ray launched at -2 mrad, its intensity is not as high as the ray launched at 0 and -1 mrad because for most of its path the ray is in the region of 0.10 to 0.25 mm where the gain is has a negative gradient.

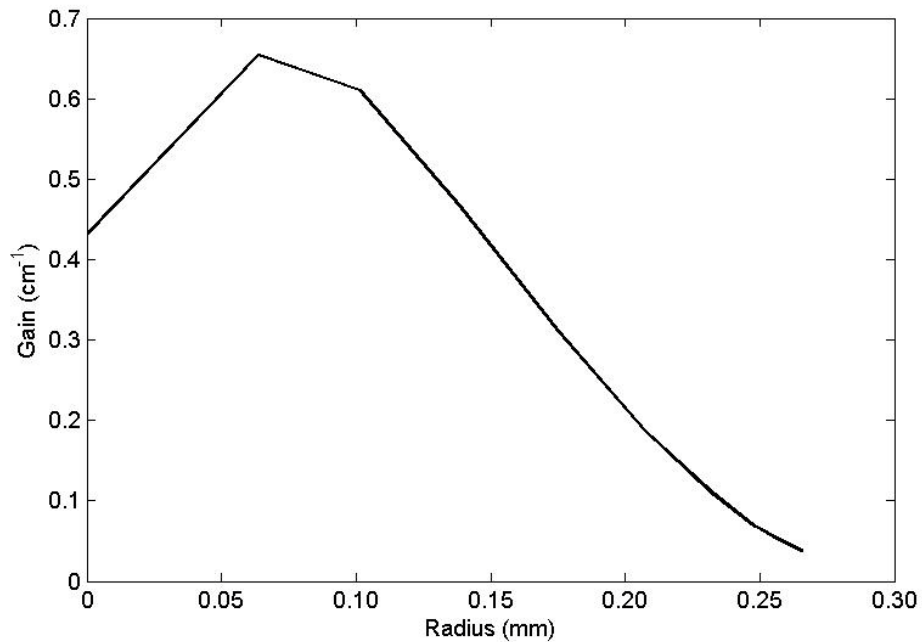


**Figure 5.8** Gain profile at maximum compression by current pulse of 16 kA peak current having rise time about 50 ns with 20 cm long capillaries of 3 mm diameter filled with 0.15 mbar of pure argon gas.

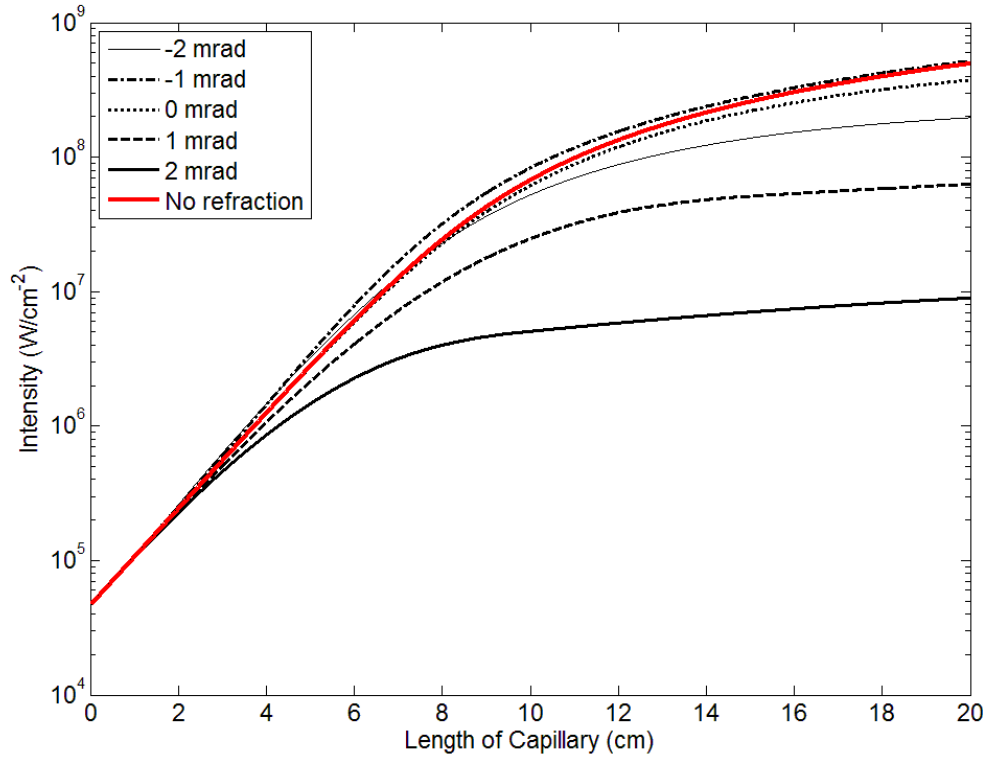
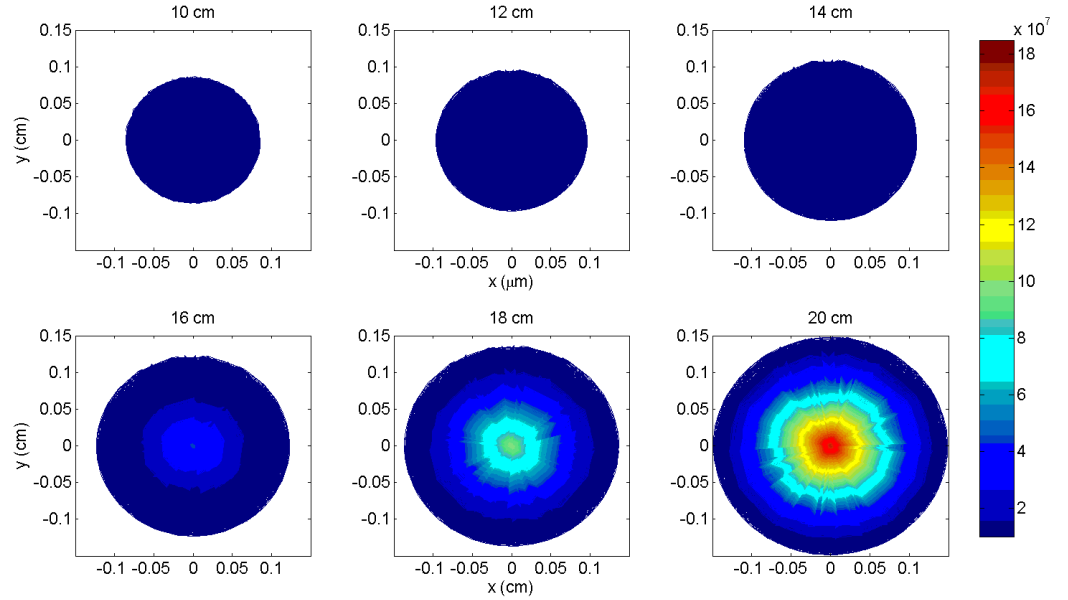


**Figure 5.9** Integrated intensity obtained as a function of  $z$ . Rays are launched at the time of pinch. The red bold solid curve is obtained with the same code but without refraction effects.

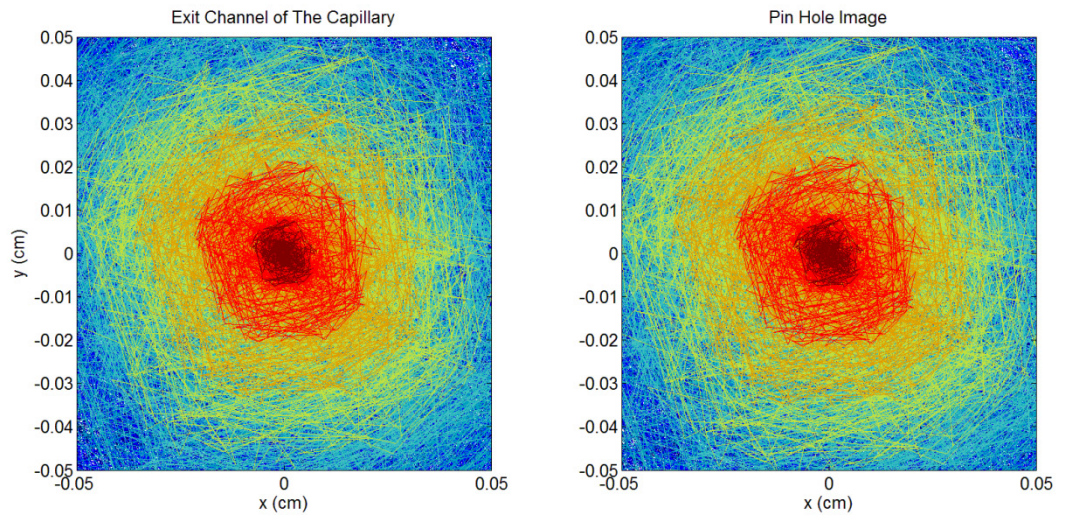
Fig. 5.9 shows that the intensities of the rays which were refracted out of the plasma region at the end of 20 cm length of the capillary were 1 or 2 orders of magnitude lower than the intensities of the rays which were concentrated inside the plasma column.

Fig. 5.10 shows cross-sectional images of plasma column at various lengths along the capillary. For the capillary length of 10 cm, the intensity of inner zone plasma is about  $10^7$  W/cm<sup>2</sup>, while the intensity of outer zone plasma is about  $10^6$  W/cm<sup>2</sup>. The difference between the inner and outer zones was only 1 order of magnitude. In Fig. 5.10, this difference was not detectable due to the intensity was normalized from scale intensity of 20 cm capillary long. As the capillary lengthens, the cross sectional image area of plasma column increase. The intensity at the centre of plasma column also increases exponentially, whereas the intensity of the outer region of the plasma column grows linearly after 10 cm capillary length.

Fig. 5.11 shows the images of plasma column at the exit of the capillary and pinhole. The figure has been cropped to focus on the central  $0.1 \times 0.1 \text{ cm}^2$  region. The distance between the pinhole and the exit of the capillary is 1 cm. So the divergence of the rays is not critical at the pinhole. Hence, images from both points look similar.



**Figure 5.10** The image of the plasma column at various different lengths along the 20 cm long capillary.



**Figure 5.11** The images of the plasma column in the exit of the capillary and the pinhole.

In Chapter 3 it was mentioned that the size of plasma column during maximum compression in the simulation was greater than that of the experiment because only the FWHM radiating region of the plasma column was measured in the experiment. Here, the FWHM radiating region of the plasma column was calculated, and then it should be smaller than the actual size of plasma column. In the Helios-CR calculation, the size of plasma column was about  $520\text{ }\mu\text{m}$  (in diameter). In Fig. 5.10 and Fig 5.11, the size of radiating region was simulated about  $400\text{ }\mu\text{m}$  (in diameter) which is in reasonable agreement with the estimation from experiment.

#### 5.4 Analysis of Capillary Discharge Soft X-ray Laser Experiments

In this section the theoretical tools developed in the previous section are used to analyze experimental results of amplification at 46.9 nm in Ne-like argon in the plasma column of a compressional capillary discharge.

Fig. 5.12 (Fig. 5.13) shows the comparison of the experimental data and simulation data from 3 mm diameter capillary, excited by a current pulse of 16 kA (19 kA) peak current having a first half cycle duration of about 50 ns. In Fig. 5.12, the optimum intensity of this configuration occurred at 0.18 mbar of initial gas filling pressure in the experimental observation. For initial gas filling pressures lower than 0.11 mbar, the plasma move too quickly, causing the ions to over-heat and since the  $\text{Ar}^{8+}$  population is not sustainable, so the intensity dropped tremendously. Conversely, at initial gas filling pressure higher than 0.28 mbar, the plasma moves too slowly and the ions become under-heated and  $\text{Ar}^{8+}$  population are not able to be produced, so the intensity also drops tremendously.

In Fig. 5.12, on the other hand, showed the integrated intensity of the 46.9 nm Ne-like Ar line as a function of the initial gas filling pressure for three different time delays, i.e. 2, 6 and  $12\text{ }\mu\text{s}$  at 16 kA peak current. The prepulse current was set at 16 A

for all the experiments. Comparison of the experimental results in Fig. 5.12 show that the optimum gas filling pressure is affected by the choice of the prepulse time delay. Specially, the optimum gas filling pressures increase with increasing time delay, which is shown in Table 5.1. At high prepulse time delay the intensity-pressure curve flattens. These shifts are due to the effect of time delays of prepulse current to the absorption of the laser output by the plasma plume, which is ejected out of capillary, and also to the changes in the pressure in the capillary channel during the prepulse [18]. The effects of the time delays of prepulse current on the ion density distribution and electron temperature were not taken into consideration in this work. The uniform distribution of ion density and electron temperature were only taken into account in simulation regime. Hence, the shifts of optimum initial gas filling pressures due to the effect of prepulse were not detectable in simulation calculation. However the shape of the intensity prediction was given a good agreement compared to the experiment of the prepulse current's time delay of 2  $\mu$ s.

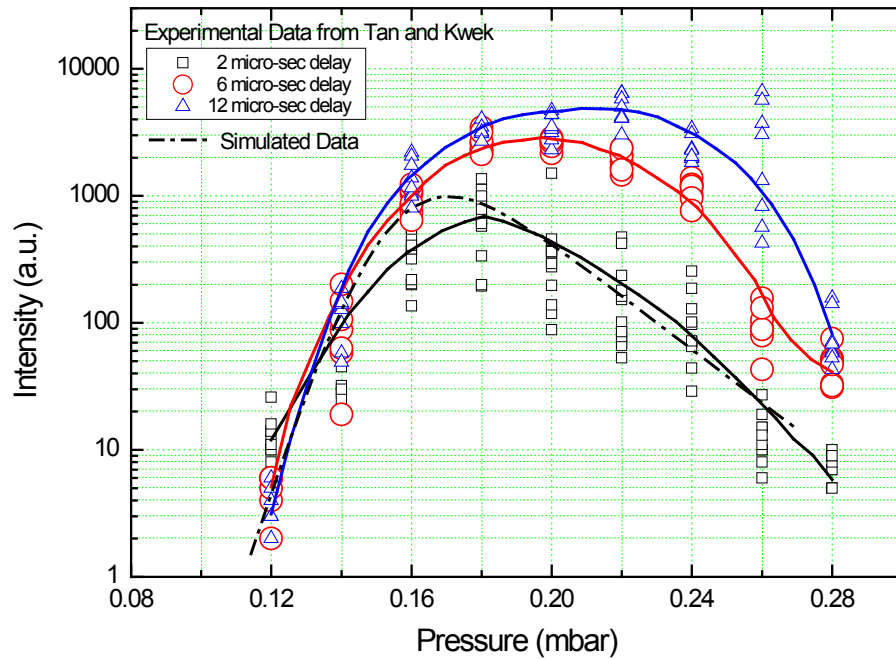


**Figure 5.12** Comparison experiment at data and the simulation in a 3 mm diameter capillary excited by current pulse of 16 kA peak current having a first half cycle duration of about 50 ns. The full line is meant to guide the eye.

**Table 5.1** The prepulse time delay that corresponding to optimum initial gas filling pressure.

Prepulse Time Delay ( $\mu s$ )	2	4	6
Optimum Initial Gas Filling Pressure (mbar)	0.18	0.20	0.22

At 19 kA peak current, however, the dependence of intensity on pressure shows a discrepancy with respect to the experimental results, as shown in Fig. 5.13. A possible reason for the discrepancy is that the experimental intensity output was measured from 12  $\mu s$  time delay of 16 A prepulse current. Unfortunately, laser intensities for smaller time delays were not collected in the experiment. So, in analogy with the prediction of Fig. 5.12, we conjecture that the simulated laser intensity output may agree more closely if compared to the experimental intensity output for reduced time delay of the 16 A prepulse current. However, the influence of prepulse current is critical in experimental [18] setup. Incorporation of the effects of prepulse into the MHD model is an open problem for future study.

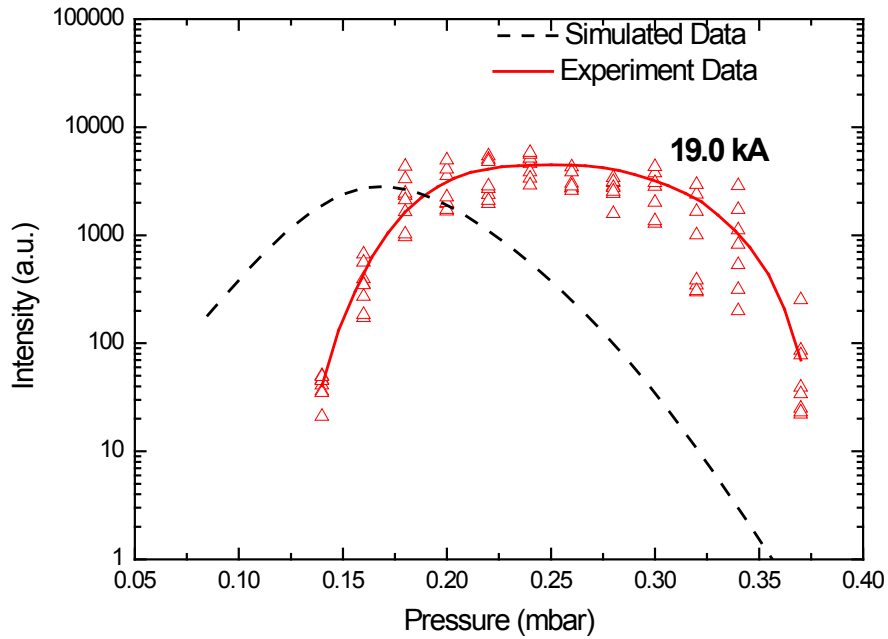


**Figure 5.13** Comparison data of the experiment and the simulation in 3 mm in diameter capillary, excited by current pulse of 19 kA peak current having a first half cycle duration of about 50 ns.

As conclusion, a ray tracing code has been developed to consider refractive effects on photon propagation in cylindrical capillary discharge plasma where radial electron density exists. A refracting system described by Girard [69] was chosen to verify the code developed by the author and the preliminary results have been presented in section 5.1.

The propagation of a ray during the maximum compression of the initial inputs of 16 kA maximum current load with the rise time of 50 ns, 3 mm size of capillary diameter, 20 cm of capillary length filled with 0.15 mbar Argon gas has been studied. The refraction effects of the differences of the initial launch angles have been also explained based on the electron density profile and gain profile. The effect of refraction was not so critical in a high electron density profile. However, for electron densities the rays escaped out of the plasma column due to refraction effect, causing a reduction in the intensity of 1 or 2 orders magnitude of lower than the intensity of the rays within the plasma column.

The cross sectional images of the capillary at different lengths of the column were shown. The numerical pinhole images have been obtained using the same imaging set-up as in experiment [18]. Finally, the comparison data of the experiment and the simulation in 3 mm in diameter capillary, excited by a current pulse of 16 kA and 19 kA peak current having a first half cycle duration of about 50 ns have been performed and, showing a reasonable agreement with experimental data.

## Chapter 6

### Modelling of a Nitrogen X-ray Laser Pumped By Capillary Discharge

#### 6.1 Introduction

In previous chapters, successfully modeled capillary discharge of  $\text{Ar}^{8+}$  ion gas leading to lasing at 46.9 nm wavelength was presented. The simulation gave good agreement with experimental results. In view of this success, we are interested to apply the simulation to the study of the capillary discharge of hydrogen-like nitrogen ions. This system is of interest because the 13.4 nm laser line has industrial application. Section 6.2 discusses the ionization processes leading to the generation of the  $\text{N}^{6+}$  ion. Section 6.3 investigates the prediction of Vrba [73] that lasing action leading to 13.4 nm wavelength line can be produced for a specific configuration.

#### 6.2 Principle of Recombination Pumping

In general, a capillary-discharge establishes a hot ionized plasma in a long narrow cylinder. During the pinch plasma expansion, non-equilibrium under-cooled plasma produce recombination pumping of hydrogen-like ions inside the capillary. If the recombination pumping scheme is applied to a capillary filled with nitrogen gas, the excited hydrogen-like nitrogen ion ( $\text{N}^{6+}$ ) will be created:



From the upper level of the Balmer alpha transition  $n = 3 \rightarrow n = 2$ , the required excited state  $\text{N}^{6+}$  will be formed, and 13.4 nm lasing wavelength may expect to be produced. Due to this reason, the recombination pumping needs to be efficiently excited to the upper laser level, and yield a high concentration of fully stripped ions  $\text{N}^{7+}$ . A high electron density is also required.



The fractional abundance of charged states is evaluated using steady-state ionization model by using the PrismSPECT [46] code. The results are shown in Fig. 6.1. To obtain a hydrogen-like nitrogen state ( $N^{6+}$  or N VII) the equilibrium nitrogen plasma must be heated to a temperature of about 80 eV. The ionization population fraction is determined in the range  $T_e \sim 1-10000$  eV for a given electron number density,  $N_e \sim 1.0 \times 10^{18} \text{ cm}^{-3}$ , which has been chosen for this study. The temperature range of H-like ionization state is approximately between 50 – 400 eV. A prevailing concentration of fully stripped  $N^{7+}$  (or N VIII) ions is formed if the plasma electron temperature exceeds 150 eV.

It should be remembered that the steady-state ionization model neglects the time dependence. During pinch compression, the plasma is heated and gets cooled during the pinch decay. In order to obtain fully stripped  $N^{7+}$  (or N VIII) ions during pinch compression, the electron temperature should be higher than that assigned for equilibrium plasma, in this case,  $>150$  eV [73].

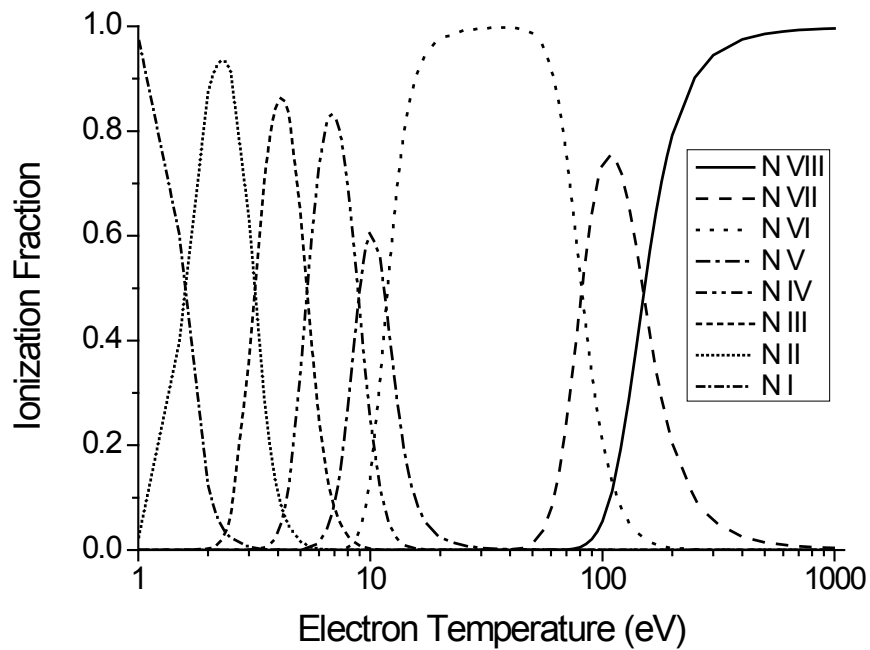


**Figure 6.1** Temperature dependences of nitrogen ionization fractions evaluated according to PrismSPECT code for initial nitrogen atom density  $N_0 = 1 \times 10^{18} \text{ cm}^{-3}$ .

### 6.3 A Case Study

A critique of the work of Vrba *et al.* [73] has been done for the nitrogen level dynamics. They reported that the core electron temperature was 150 eV and the electron density was of the order of  $1.5 \times 10^{20} \text{ cm}^{-3}$  by using MHD and the FLY atomic code [74]. However, when parameter inputs similar to Vrba were used in the Helios-CR code, no gain was detected. To investigate the veracity of the Helios-CR code an experiment of Kampel [75] has been examined.

In the work of Kampel [75], the possibility of realizing a  $H_\alpha$  nitrogen recombination laser ( $3 \rightarrow 2$  transition) at wavelength of 13.4 nm was examined, using a capillary discharge Z pinch. The experiment was conducted with 60 kA load peak current and 70 ns rise time to generate a Z-pinch plasma in a 90-mm-long and 5-mm-diameter capillary. An initial gas filling pressure of 0.6 Torr was applied inside the capillary.

Fig. 6.2, 6.3 and 6.4 are the results obtained from Helios-CR simulation. Fig. 6.2 shows the time dependence of the capillary current (dashed line) and trajectories of nitrogen plasma elements inside the capillary. In the early stages ( $t < 20$  ns) the plasma does not compress immediately due to the fact that the plasma pressure exceeds other forces. However, the plasma is constrained by the rigid wall of the capillary. Both the initial filling pressure and Joule heating are the main contributors to the pressure in the outer zones of the plasma. Generally, the current tends to flow in the outer part of the cylindrical plasma, and Joule heating occurs due to the current passing through the plasma. This heating results in an increase in pressure which can be sufficiently high for the outer regions of the plasma to initially expand before being accelerated inward by the magnetic piston.

When the discharge current has reached a value such that the magnetic pressure exceeds the thermal pressure (i.e., for  $t > 25$  ns), the plasma is compressed inward

toward the axis. At the same time, a vacuum region starts to form near the wall and a converging shock wave is developed at 25 ns which propagates from the wall to the channel axis (see Fig. 6.3). The shock waves eventually meet at the axis, and are subsequently reflected. During compression, the plasma becomes hotter due to Joule and shock heating, and the thermal pressure increases, essentially ionizing the nitrogen. The time of the first contraction or pinching of the plasma was about 53 ns (as shown in Fig. 6.2).

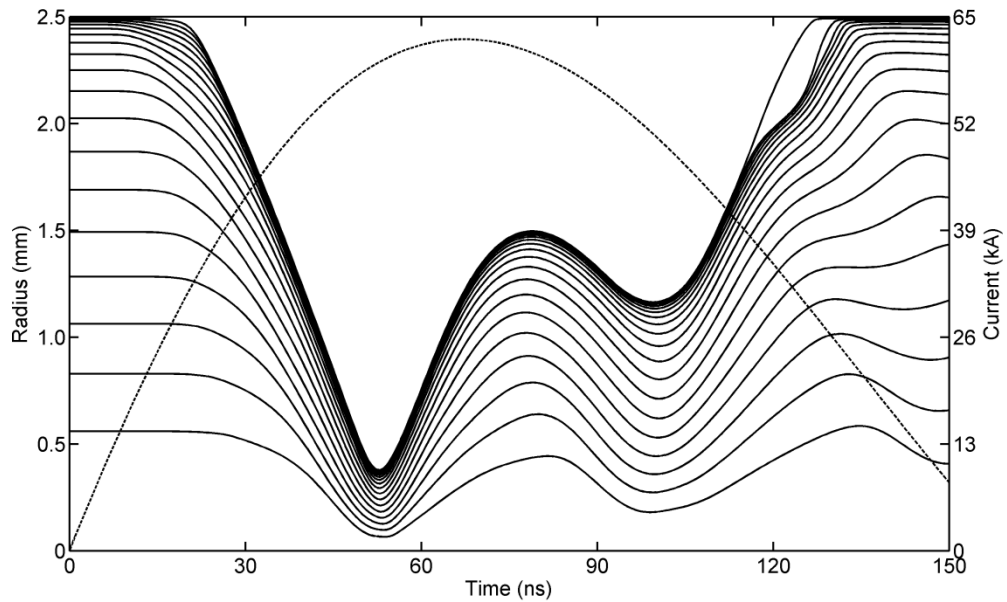


**Figure 6.2** Time dependence of the capillary current (dashed line) and trajectories of nitrogen plasma elements inside the capillary which simulated from Helios-CR code.

Before the time 70 ns, when the total current has been increasing to the maximum value, the discharge current is high and the Lorentz force dominates. Thus, the compression phase ceases. When the thermal pressure balances the magnetic pressure, the plasma reaches maximum compression and then expands. During the compression, the plasma has been finally produced to high density and temperature plasma on the axis (as shown in Fig. 6.3). At  $t = 53$  ns, the temperature  $T_e$  reaches the value of 95 eV and should rapidly cool down. The value of electron density  $N_e$  at the

pinch is about  $2 \times 10^{19} \text{ cm}^{-3}$ . However, after compression the shock wave gets reflected from the axis to the wall of plasma column. Hence it heats up again to 90 eV for electron temperature during the second pinch at about 100 ns.

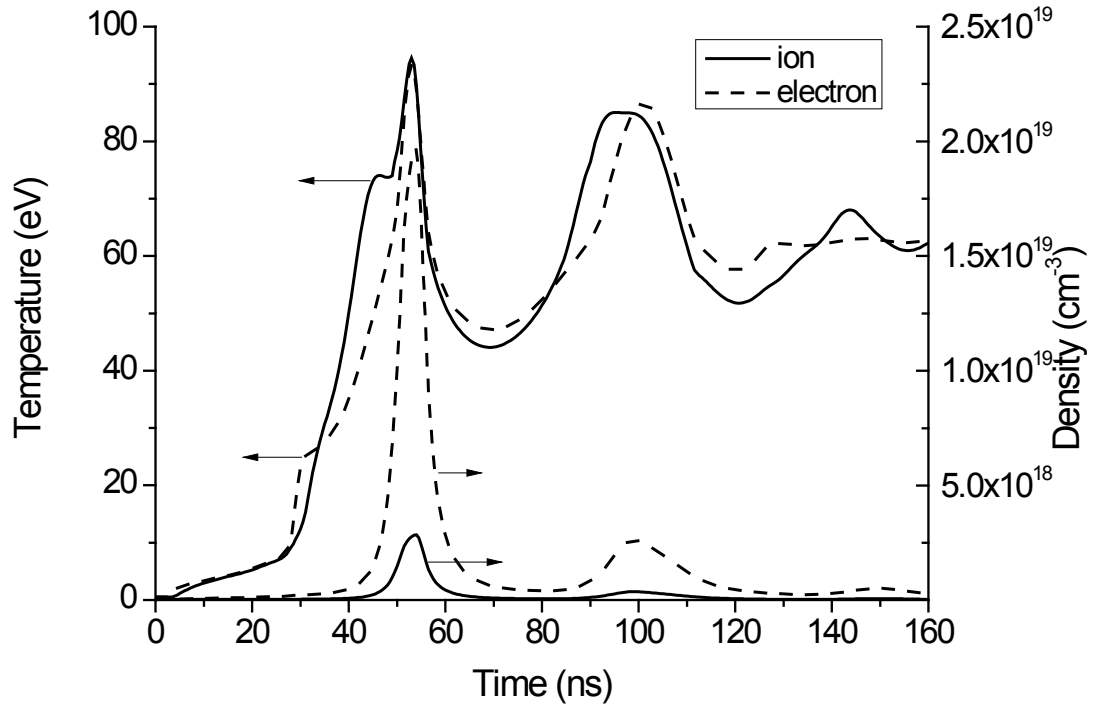


**Figure 6.3** The evolution of core temperatures and densities of ion and electron simulated from Helios-CR code.

In any event, the results shown in Fig. 6.3 indicate that the electron temperature and density do not fulfil the requirements as suggested as Vrba [73] (i.e. electron temperature of 150 eV and electron density of  $10^{20} \text{ cm}^{-3}$ ). Hence, it is unlikely that laser action may occur under the condition given by Vrba [73].

Quick changes of electron temperature during the plasma pinch and decay lead to ionization and excitation non-equilibrium. Substantial changes of ionization of nitrogen were found at different time (see Fig. 6.4). At the pinch time of 53 ns, the inner region of the plasma has 80% of  $\text{N}^{5+}$ , the middle region of the plasma has 80% of  $\text{N}^{6+}$  and outer region of the plasma has about 95% of  $\text{N}^{7+}$ . Hence, multiple ionizations

happen at the same time in different zones. These happen because different zones have different electron densities. Especially low electron density ( $10^{14} \text{ cm}^{-3}$ , in this case) usually occurs at outer zones, making nitrogen ions easier to become fully stripped ( $\text{N}^{7+}$ ) at such densities. The electron temperature of 95 eV does not fall into the ion abundance, unlike in the case of argon, so the ionization bottleneck of nitrogen also does not exist. That means that for slightly different electron densities, the multiple ionizations can easily occur for the nitrogen case. So, with such instability of ionization regime,  $\text{H}_\alpha$  nitrogen recombination laser ( $3 \rightarrow 2$  transition) at wavelength of 13.4 nm can be very hard to produce.

The above arguments can be proved with the experiment in Kampel [75] and it is shown in Fig. 6.5 and Fig. 6.6. Fig. 6.5 showed the time-resolved fast x-ray diode (XRD) with different filters which emitted x-ray radiation (photons above 300 eV). The pinch emission was measured through on-axis and off-axis pinholes. In Fig. 6.5, the filtered XRD signals (left axis) and the current measurements (right axis) are shown for different shots. The measurement was taken from an initial gas pressure of 0.6 Torr of  $\text{N}_2$  molecules.

The filtered XRD measured only photons with energy above 300 eV, therefore the signals correspond only to highly ionized ions. The XRD signal began only when the inward-moving pressure wave reaches the capillary centre at first pinch in Fig. 6.2 and an expanding shock wave is formed. The second pinch time also predicted in Fig. 6.2.

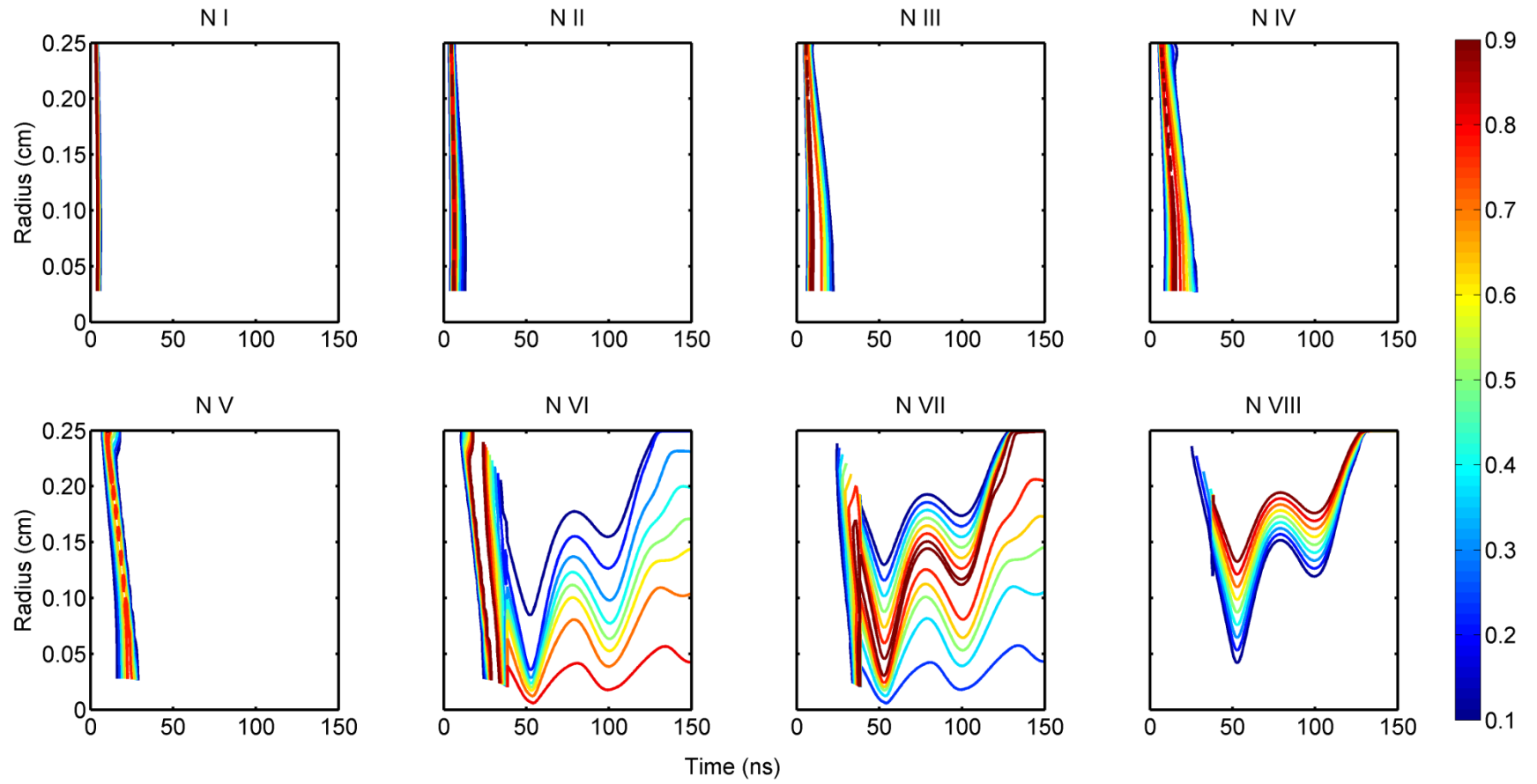


**Figure 6.4** Temporal and spatial evolution of ionization fraction of nitrogen simulated from Helios-CR code.

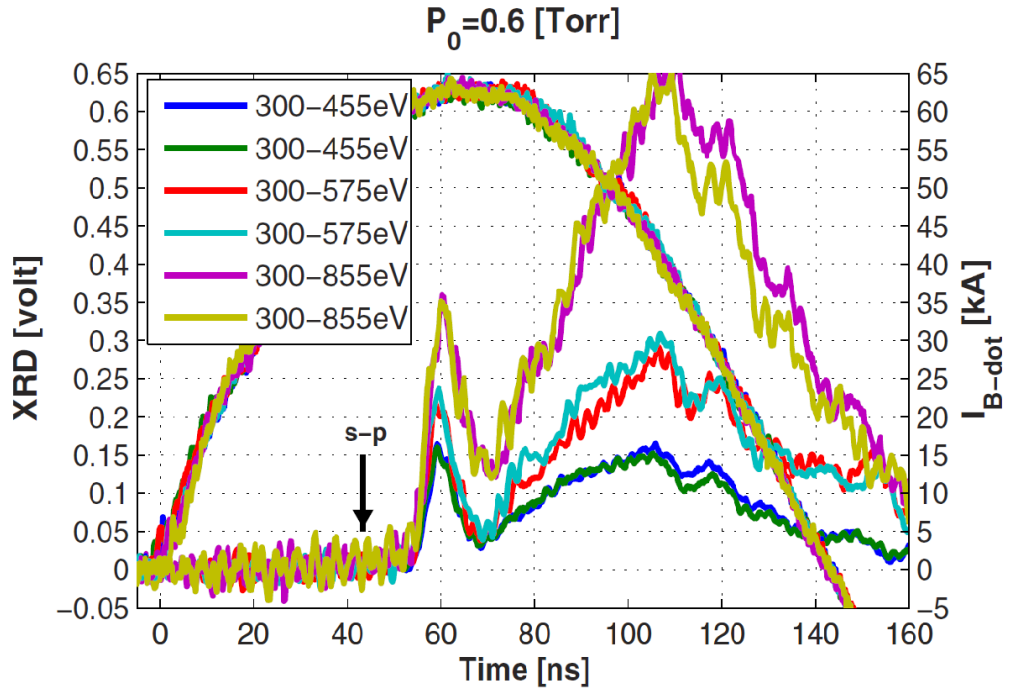


**Figure 6.5** XRD signals (left axis) and current measurements (right axis) are shown as a function of the time. The legend shows the filter transmission energy (300 – 455 eV Ti, 300 – 575 eV Cr, and 300 – 855 eV Ni). Here the measurement with the initial pressures of  $N_2$  molecules of 0.6 Torr which extracted from Ref. [75].

Fig. 6.6 showed four measured spectra with different initial gas pressures. The H-like nitrogen lines and the recombination spectra of H-like and fully stripped nitrogen were observed (which were predicted in Fig. 6.4). There are many lines that were not identified. These lines probably originate from the cathode and anode ablation at late times due to the time-integrated measurement. This ablation plasma, which consists of 70% tungsten and 30% copper, has many lines in the measured area, especially at  $\lambda = 3 - 10$  nm, where there are few nitrogen lines [75].

The wavelength spectrum can be divided into three different sections:  $\lambda > 11$  nm,  $3 < \lambda < 11$  nm, and  $\lambda < 3$  nm. The spectrum at wavelengths above 11 nm consists mostly of Li-like nitrogen lines, from a relatively cold plasma. This was expected in time-integrated measurements. The “broad” line observed at  $\lambda = 14 \pm 1$  nm is composed of Li-like, He-like, and H-like nitrogen lines.

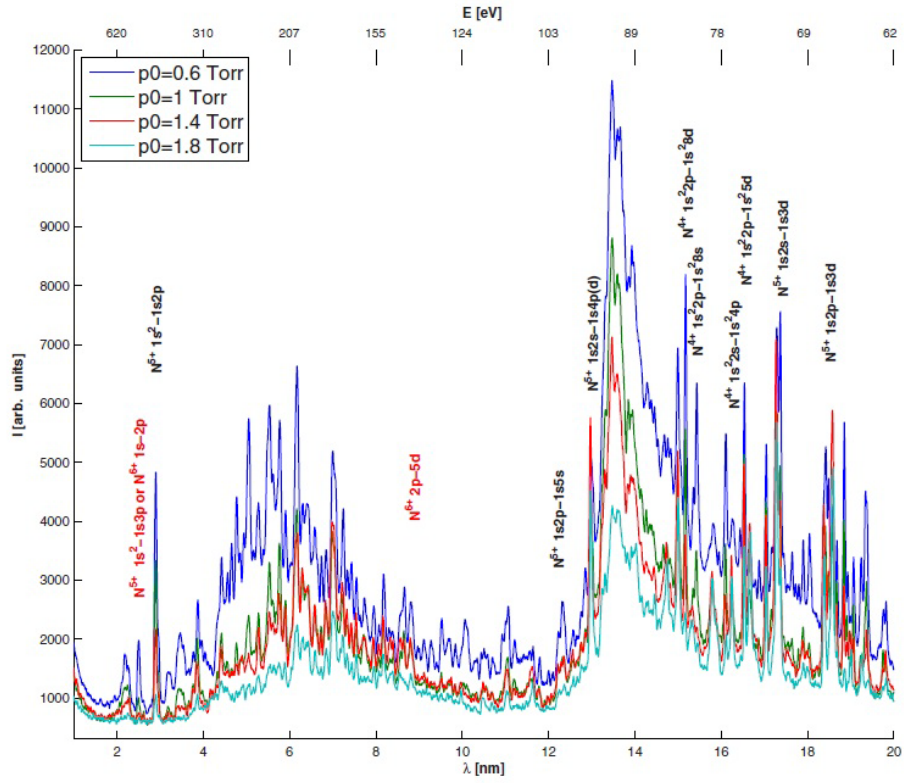


**Figure 6.6** Time-integrated transmission grating spectroscopy results at four different initial gas densities, 0.6, 1.0, 1.4, and 1.8 Torr. Bottom  $x$  axis is the spectrum wavelength  $\lambda$  in nanometers. The Top  $x$  axis is the spectrum wavelength  $E$  in eV, extracted from Ref. [75].

Since there was no continuum radiation emitted at wavelengths above 9 nm (see Fig. 6.6) the measured spectrum at wavelengths 3 – 11 nm was not related to bremsstrahlung radiation. This spectrum corresponds to line emissions from the electrodes' ablated materials and to photo-recombination of fully stripped nitrogen to H-like nitrogen at the second level ( $n = 2$ ,  $\lambda = 7.3$  nm). This was evident in the measurement at initial gas pressure of 0.6 Torr.

The spectrum at wavelengths below 3 nm gives most of the information about the ionization abundance of the nitrogen plasma. In this region only nitrogen lines exist and accordingly the interpretation is straightforward. In these wavelengths, the filtered XRD signals were used to measure the ionization abundance dynamics, as well as to estimate the electron temperature.



Kampel [75] suggested the required plasma condition, that the pinch electron temperature needs to reach about 140 eV and the pinch electron density to be about  $5 - 10 \times 10^{20} \text{ cm}^{-3}$ . The demonstrated pinch electron temperature reported was less than 100 eV. This agrees with our simulation. In this work, Kampel's suggestions were tested, but the  $H_\alpha$  nitrogen recombination laser ( $3 \rightarrow 2$  transition) at wavelength of 13.4 nm was not obtainable even the required plasma condition has been achieved. The main reason was the population inversion of  $3 \rightarrow 2$  transition at wavelength of 13.4 nm was not produced in PrismSPECT. So, lasing at 13.4 nm wavelength using excited hydrogen-like nitrogen ion ( $N^{6+}$ ) by a capillary discharge was not achieved and this contradicted Vrba's result [73].

## Chapter 7

### Conclusion

In this work, the capillary discharge soft x-ray laser was modeled. Chapter 1 introduced the various types of short wavelength electromagnetic radiation sources which was followed in Chapter 2 by a consideration of the concepts underlying the laser, i.e., recombination pumping and collisional pumping. The theory of the capillary-discharge x-ray laser was given since it provided the basis for the simulation investigation of the type of x-ray laser considered in this thesis. In addition background theory for the numerical modelling of a capillary-discharge soft x-ray laser was described.

A numerical study of a capillary discharge Neon-like Argon x-ray laser was reported in Chapter 3. Specifically, the soft x-ray laser was modeled using a one-dimensional single-fluid magneto-hydrodynamics (MHD) model, with separate electron and ion temperatures. The MHD equations were solved by the Lagrangian cylindrical geometry approach. The effects of 4 input parameters (the capillary radius  $r_0$ , initial argon gas filling pressure  $p_0$ , discharge current peak value  $I_{max}$  and its quarter period  $T_{1/4}$ ) on the electron density and electron temperature were studied. Initially, the behaviour of plasma dynamics for a capillary discharge (preliminary case study) with a peak current of 16 kA, a diameter capillary of 3 mm and 0.15 mbar initial gas filling pressure have been presented in Chapter 3. This configuration produced 70 eV electron temperature and  $3 \times 10^{18} \text{ cm}^{-3}$  electron density at the pinch and these fulfill the required electron profiles (i.e. the electrons have to be in the temperature range of 40 – 90 eV and with a number density range of  $1 - 40 \times 10^{18} \text{ cm}^{-3}$ ) in order to obtain lasing action. Comparison of simulation results was made to the experiments of Tan and Kwek [18], Rocca [50], Niimi [51] and Heinbuch [52] which showed good agreement with the

experiments. These agreements led a confident foundation to understanding the laser system and to further optimize the laser conditions.

Hence, the effect of each input parameter in the optimization of the system has been analyzed in Chapter 4. Due to this, the influence of the changes of peak current from 13.5 kA to 19 kA on the choice of the initial gas filling pressures have been studied. The simulation range of the initial gas filling pressures obtained agreed well with the experimental results. Consequently, the effects of the current rise time and the changes of the capillary radius were further analyzed in the study of optimization at 100 kA peak current. Combinations of the input parameters leading to optimized gain profile were suggested for this laser system.

Subsequently, the effects of refraction on the output intensity were studied. So the intensity output was modelled with ray tracing code in Chapter 5. In addition, the numerical images of the plasma column at different lengths along the capillary and at the pinhole have been obtained. The diameter of the radiating plasma and laser intensity has been estimated which agreed well with the experimental results.

In view of the success of the modelling on neon-like argon laser system, we applied the simulation to study the capillary discharge of hydrogen-like nitrogen in Chapter 6. The simulated results agreed well with experimental data of Kampel [75] in contrast to the conjecture of Vrba [73]. A simulation was performed to test Kampel's suggestion that lasing action at 13.4 nm wavelength should occur at 150 eV electron temperature. We found that the  $H_{\alpha}$  nitrogen recombination 13.4 nm laser line cannot be realized even though the required plasma condition has been achieved due to insufficient inversion population ( $3 \rightarrow 2$  transition) for the hydrogen-like nitrogen ion ( $N^{6+}$ ).

## **Appendix**

- A. Published Work
- B. Ray-tracing Code
- C. The Derivation of The Energy Balance with Thermal Diffusion for Electrons and Ions
- D. The Derivation of The Magnetic Field Transport and Diffusion Equation

## **A. Published Work**

1. Teh C. P., Bernardine R. W., and Kwek K. H. (2009) Computational modelling of A Fast Capillary Discharge Soft X-ray Laser. In Yahya Abu Hasan, Norhashidah Mohd. Ali and Ahmad Izani Md. Ismail (eds) 5<sup>th</sup> Asian Mathematical Conference Proceedings (Volume II), June 2009, pp 473 - 479. ISBN: 978-967-5417-54-2.
2. Teh C. P., Wong B. R., and Kwek K. H. (2012) Modelling of fast capillary-discharge for soft x-ray lasers. In Luis Bilbao, Fernando Minotti and Hector Kelly (eds) 14th Latin American Workshop on Plasma Physics (LAWPP 2011), 20-25 November 2011, Journal of Physics: Conference Series **370**, pp 012036. doi:10.1088/1742-6596/370/1/012036 (IOP Publishing).

# COMPUTATIONAL MODELING OF A FAST CAPILLARY DISCHARGE SOFT X-RAY LASER

<sup>1</sup>Teh Chew Peng, <sup>2</sup>Bernardine Renaldo Wong Cheng Kiat and <sup>1</sup>Kwek Kuan Hiang

<sup>1</sup> Department of Physics, University of Malaya, 50603 Kuala Lumpur.

<sup>2</sup> Institute of Mathematical Sciences, University of Malaya, 50603 Kuala Lumpur.  
e-mail: tcp5441@perdana.um.edu.my

**Abstract.** *In this work we present the results of the numerical investigations of the one-dimensional single-fluid magneto-hydrodynamics (MHD) model, with separate electron and ion temperatures, of a capillary discharge collisional soft x-ray laser. The MHD equations are solved by the Lagrangian cylindrical geometry approach. The effects of the gas filling pressure and discharge current on the plasma densities and temperatures, and implosion-pinch phase for soft x-ray lasing conditions have been analyzed. The results are compared with experimental measurements of the operating pressure ranges.*

## 1 Introduction

Soft x-ray lasers are invaluable tools for studying high-density plasmas and permitting one to see smaller features in microscopy, to write finer patterns in lithography and to generate shorter pulses. These lasers have applications for the materials science community, both inside and outside the laboratory, by supplying detailed information about the atomic structure of new and existing materials. These in turn lead to new scientific understandings, perhaps through surface science, chemistry and physics, providing feedback to the enabling technologies. Development of soft x-ray spectral region is presently in a rapid growth and interchange among science and technology.

In 1984, soft x-ray lasers were first demonstrated in plasmas generated by powerful laser drivers in large laboratories [1, 2]. However, the large pump lasers for this kind of soft x-ray laser experiments are only available at a few large laser facilities in the world due to their large size, complexity, and extremely high cost. Therefore the demonstration of a capillary discharge soft x-ray laser operating in the transition of Ne-like ions by Rocca *et al* [3] in 1994 opened the possibility to develop compact, efficient and simpler soft x-ray laser. This similar demonstration had then been only repeated by Ben-kish *et al* [4] in 2001, followed by the work of Niimi *et al* [5] and Tomassetti *et al* [6] in the following year. The quest for improving these systems still continues by parallel efforts involving theory and computer simulations of the experiments to understand the laboratory observation and to optimize the resulting energy density. Even after more than a decade, systems with improved performance and efficiency are still being reported [7].

In this paper, the capillary discharge soft x-ray laser described by Tan and Kwek [8] is modeled using two-temperature, one dimensional single-fluid magneto-hydrodynamics (MHD) equations. The details of the governing equations and the computational simulation will be applied and shown. The model was then utilized to numerically evaluate the time and radial dependences of capillary plasma characteristics of fast capillary discharges with current rise time of around 35 ns and peak currents ranging between 9 to 19 kA in a capillary 3 mm in diameter filled with pre-ionized argon gas. The results were then compared with experimental data [8] from different initial argon filled pressures for a set of the discharge currents. The effects of the gas filling pressure and discharge current on the plasma densities and temperatures, during implosion-pinch phase for soft x-ray lasing conditions were analyzed. Optimal discharge parameters and plasma conditions have been computed.

## 2 Physical model

### 2.1 Magneto-hydrodynamics model

The one dimensional single-fluid MHD model is based on the method of describing the Z-pinch discharge plasma as a hydro-magnetic fluid. The basic MHD equations used are depicted below.

The continuity equation (mass conservation) is given by

$$\frac{\partial \rho}{\partial t} + \nabla \cdot (\rho \mathbf{u}) = 0, \quad (1)$$

where  $\rho$  is mass density and  $\mathbf{u}$  is the plasma fluid velocity. Generally, in any steady state process, the rate at which mass enters a system is equal to the rate at which mass leaves the system. In this system, the continuity equation is automatically satisfied.

The momentum conservation equation is solved in the one-fluid approximation where the plasma electrons and ions are assumed to flow together as a single fluid. The momentum equation is governed by

$$\rho \frac{\partial \mathbf{u}}{\partial t} = -\nabla(P_e + P_i + P_r + q) - \mathbf{J} \times \mathbf{B} \quad (2)$$

where  $P_e$ ,  $P_i$  and  $P_r$  are the thermal pressures due to electrons, ions and radiation, respectively,  $\mathbf{B}$  is the magnetic field induced by the axial current and  $\mathbf{J}$  is the axial component of the electric current density. Here,  $q$  is the von Neumann artificial viscosity [9] which is included in the equation of motion to handle shocks.

The energy balance for electrons and ions are described by

$$C_{v,e} \frac{\partial T_e}{\partial t} = V \nabla \cdot (\kappa_e \nabla T_e) + \frac{V \eta}{(4\pi)^2} |(\nabla \times \mathbf{B})|^2 - \left( \frac{\partial E_e}{\partial V} + P_e \right) \frac{\partial V}{\partial t} - \frac{(T_e - T_i)}{t_{eq}} + R_{Abs} - R_{Emis}, \quad (3)$$

$$C_{v,i} \frac{\partial T_i}{\partial t} = V \nabla \cdot (\kappa_i \nabla T_i) - \left( \frac{\partial E_i}{\partial V} + P_i \right) \frac{\partial V}{\partial t} + \frac{(T_e - T_i)}{t_{eq}} - q \frac{\partial V}{\partial t}. \quad (4)$$

where  $C_v$ ,  $T$ ,  $E$ ,  $P$  and  $\kappa$  are, respectively, the specific heat, temperature (in eV), specific internal energy, pressure and thermal conductivity [10], of the electrons ( $= e$ ) and ions ( $= i$ ). While  $V$  is the specific volume, the second term is the joule heating term,  $\eta$  is defined as the plasma electrical resistivity [11],  $R_{Abs}$  and  $R_{Emis}$  are the radiation absorption and emission terms [12], and  $t_{eq}$  is the electron-ion collisional coupling term.

The difference between the temperature diffusion equations for the electrons and ions is the absence of the Joule heating term in the ion equation. Since the currents are mainly due to the lighter electrons, the energy is transferred to ion through the collision specified by the term involving  $t_{eq}$ .

The magnetic field transport and diffusion equation reads

$$\frac{\partial \mathbf{B}}{\partial t} = \frac{\eta}{4\pi} (\nabla \cdot \nabla) \mathbf{B} - (\nabla \cdot \mathbf{u}) \mathbf{B}. \quad (5)$$

This equation is obtained using Maxwell equations and generalized Ohm's law with the time variation of the electric field being neglected [13].

## 2.2 Coupled rate equation of the plasma

The non-local thermal equilibrium (non-LTE) atomic level population density of excited levels in ion species is coupled by the various atomic processes occurring in the plasma. We adopted the collisional-radiative model to obtain the population. The rate equation for atomic level  $i$  can be written as:

$$\frac{dn_i}{dt} = -n_i \sum_{i \neq j}^{N_L} W_{ij} + \sum_{i \neq j}^{N_L} n_j W_{ji} \quad (6)$$

where  $W_{ij}$  and  $W_{ji}$  represent the depopulating and populating rates between levels  $i$  and  $j$ ,  $n_i$  is the number density of level  $i$ , and  $N_L$  is the total number of levels in the system. For upward transitions ( $i < j$ ),

$$W_{ij} = \begin{cases} n_e C_{ij} + B_{ij} \bar{J}_{ij} & \text{(excitations)} \\ n_e \gamma_{ij} + \beta_{ij} + \Omega_{ij} & \text{(ionizations)} \end{cases} \quad (7)$$

while for downward transitions ( $i > j$ ),

$$W_{ji} = \begin{cases} n_e D_{ji} + A_{ji} + B_{ji} \bar{J}_{ij} & \text{(deexcitations)} \\ n_e^2 \delta_{ji} + n_e (\alpha_{ji}^{RR} + \alpha_{ji}^{DR}) & \text{(recombinations)} \end{cases} \quad (8)$$

where  $n_e$  is the electron density;  $\bar{J}_{ij}$  is the frequency-averaged mean intensity of the radiation field over a line profile;  $C_{ij}$ ,  $\gamma_{ij}$ ,  $D_{ij}$ , and  $\delta_{ji}$  are rate coefficients for collisional excitation, ionization, deexcitation, and recombination;  $A_{ji}$ ,  $B_{ij}$  and  $B_{ji}$  are Einstein coefficients for spontaneous emission, and stimulated absorption and emission;  $\gamma_{ij}$  is the photoionization rate;  $\gamma_{ji}$  is the autoionization rate;  $\alpha_{ji}^{RR}$  is the radiative recombination rate coefficient; and  $\alpha_{ji}^{DR}$  is the dielectronic recombination rate coefficient [14 – 17].

### 3 Numerical Solution

#### 3.1 Lagrangian grid structure

These MHD equations have been adopted in the Lagrangian reference frame [18, 19] using the specific volume expression, that is, a frame moving with the fluid at velocity  $u$ . The geometry is cylindrical with symmetry in the  $\theta$  and  $z$  directions. The position of each cell and the velocity on cell boundary are determined by

$$\frac{dr}{dt} = u. \quad (9)$$

All dynamical values in the equations evolve as a function of position  $r$  from the capillary axis at a time  $t$ . Zoning can be adjusted in such a way that the initial length of a zone differs from one region to the next. Mass conservation in this Lagrangian code assumes that no mass crosses between zones, so that within every zone of the grid

$$dm = \rho(r)\pi r dr. \quad (10)$$

This also implies that element masses do not change during the simulation. Considering an element with initial boundaries  $r_{oi}$  and  $r_{oi-1}$  and initial density  $\rho_{oi}$ , the mass is given by

$$m_i = \rho_{oi}\pi(r_{oi}^2 - r_{oi-1}^2). \quad (11)$$

Physically,  $m$  is the amount of mass per radian per cm in the plasma.

The boundaries move in response to forces. The mass density at any time is related to the boundary positions by

$$\rho_i = \frac{m_i}{\pi(r_i^2 - r_{i-1}^2)}. \quad (12)$$

The average radius corresponds to the center-of-mass coordinate. Assuming a uniform density, the average of a cylinder element is related to the boundary radii by

$$R_i = \sqrt{\frac{r_i^2 + r_{i-1}^2}{2}}. \quad (13)$$

#### 3.2 Numerical method

Equations (1) – (5) represent a set of five nonlinear coupled partial differential equations in five unknowns. These equations can be changed to Lagrangian frame of reference by using eqn. (10).  $m$  is now an independent Lagrangian variable and  $r$  becomes a dependent variable. Hence, we now write the system of equations in terms of  $m$ . The equations were solved numerically in a manner similar to the methods of Ref. 20. The scheme entailed dividing the plasma into  $N$  zones and then finite differencing the equations [21], using implicit numerical solution to find  $B$ ,  $T_e$  and  $T_i$ , and an explicit solution to find  $u$  and  $r$ . Both  $r$  and  $u$  are defined at the grid nodes (cell boundary) while  $B$ ,  $T_e$  and  $T_i$  are defined at the cell centres located midway between the grid nodes. Each cell or zone is split into two subzones based on the midpoint of each cell.

To initialize the calculation, various initial and boundary conditions are given to the code. These will be discussed in next section. The code begins by dividing the plasma into  $N$  radial zones. Then the mass of each zone,  $m$ , is determined (eqn. (11)), and the sub-zonal masses are defined as half the zonal mass. The nodal mass is defined as the sum of the neighbouring sub-zonal masses. The nodal, zonal and sub-zonal masses all remain fixed throughout the calculation.

The basic steps of the procedure are first to calculate the velocity  $u$  from eqn. (2), then calculating the radius  $r$  from (9). Equations (3) – (5) are next solved to find  $B$ ,  $T_e$  and  $T_i$ . Then the variables are shifted and the algorithm repeats, calculating new values in terms of the previous ones. The time steps  $\Delta t$  are not constant but instead are allowed to vary subject to constraints. The stability requirement for this scheme is given approximately by the Courant-Friedrichs-Lewy (CFL) hydrodynamics stability condition in [21].

#### 3.3 Boundary conditions

The boundary conditions which have been applied to the hydrodynamic equations (1) – (5) correspond to the simplest approximation of capillary discharge x-ray lasers, that is, if we let  $r_0$ , the radius of the capillary (the outer boundary) and no particle moves through the plasma-vacuum interface, we have

$$\left[ \frac{\partial}{\partial r} T_e \right]_{r=r_0} = \left[ \frac{\partial}{\partial r} T_i \right]_{r=r_0} = 0, \quad (14)$$



$$u(r_0) = 0, \quad (15)$$

and the magnetic field at the outer boundary is constrained by the Biot-Savart law:

$$B(r_0) = \frac{0.2I(t)}{r_0}, \quad (16)$$

$$I(t) = I_0 \sin(\omega t). \quad (17)$$

The boundary conditions at axis are

$$\left[ \frac{\partial}{\partial r} T_e \right]_{r=0} = \left[ \frac{\partial}{\partial r} T_i \right]_{r=0} = 0, \quad (18)$$

$$u(0) = 0, \quad (19)$$

and

$$B(0) = 0. \quad (20)$$

### 3.4 Initial conditions

Using the general physical model outlined in section 2, we can simulate the discharge channel with specific values of the controlling parameters. The parameters of a working discharge x-ray laser reported in Ref. 8 are used. Here the radius of the capillary has been fixed at 0.15 cm and current rise time is about 35 ns. For this basic situation, the filling pressures and the current profiles are varied to investigate the impact of these variations on the plasma. Initially, the pre-ionized plasma is assumed to be uniformly distributed with  $T_e = T_i = 1 \text{ eV}$ .

For the simulations, we use the HELIOS-CR code described in Ref. 22. It is a modeling platform that can handle LTE and non-LTE plasmas in one dimension.

## 4 The control parameters

The capillary is prefilled with neutral Argon to a certain initial filling pressure. In this study, the pressure range is from 0.09 mbar to 0.45mbar. The initial ion density can be written as

$$n_i = P_0 N_a \times 41.1 \times 10^{-6} \text{ (in cm}^{-3}\text{)}, \quad (21)$$

where  $P_0$  denotes the initial gas filling pressure and  $N_a$  is the Avogadro's number. In this case, the capillary channel is prefilled with pre-ionized gas of uniform density and temperature. However, the comparison between theory and experiment are less straightforward. This is because the experimental parameters involved pre-pulse current in which the distribution of the ion density and number of density are non-uniform.

The peak discharge currents are varied from 9 kA to 19 kA and  $2 / \tau = 140 \text{ ns}$  is used. There are the typical values used in the laser of Ref. 8.

## 5 Result and discussion

Figure 1 presents the calculated results for a capillary discharge with a peak current of 16 kA and 0.25 mbar gas filling pressure. The zone boundary position of this configuration is illustrated in Fig. 1a. The dotted line represents the discharge current. Figure 1b shows contour plots of the logarithm of the electron density measured in  $\text{cm}^{-3}$  while Figure 1c shows the electron temperature measured in eV. These figures also provide quantitative information about the distribution of the plasma parameters inside the channel at different times. Some characteristics features are discussed below.

The dynamics of Z-pinch plasma can be described by the balance between the thermal pressure and the magnetic pressure or so called the magnetic piston as described by Eqn. (2). In the early stages ( $t < 18.5 \text{ ns}$ ) the plasma does not compress immediately but actually tries to expand due to the fact that the plasma pressure exceeds other forces. However, this expansion is constrained by the rigid wall of the capillary. The pressure in the outer zones of the plasma is due to both the initial filling pressure and Joule heating. Generally, the current tends to flow in the outer part of the cylindrical plasma, and Joule heating occurs due to current passing through the plasma. This heating results in an increase in pressure which can be sufficiently high for the outer regions of the plasma to initially to expand before being accelerated inward by the magnetic piston.

When the discharge current has reached a value such that the magnetic pressure is larger than the thermal pressure ( $t > 18.5 \text{ ns}$ ), the plasma is compressed inward onto the axis. At the same time, a shock wave is formed which propagates towards the channel axis. The shock waves eventually meet at the axis, and are subsequently reflected. During compression, the plasma becomes hotter due to Joule and shock heating, and the thermal pressure increases. Although, after the time 35 ns, when the total current has dropped from the maximum value,

the discharge current is still high, and the Lorentz force can still dominate. Thus, the compression continues. When the thermal pressure balances the magnetic pressure, the plasma stagnates ( $t \approx 40$  ns) and then expands ( $t > 40$  ns).

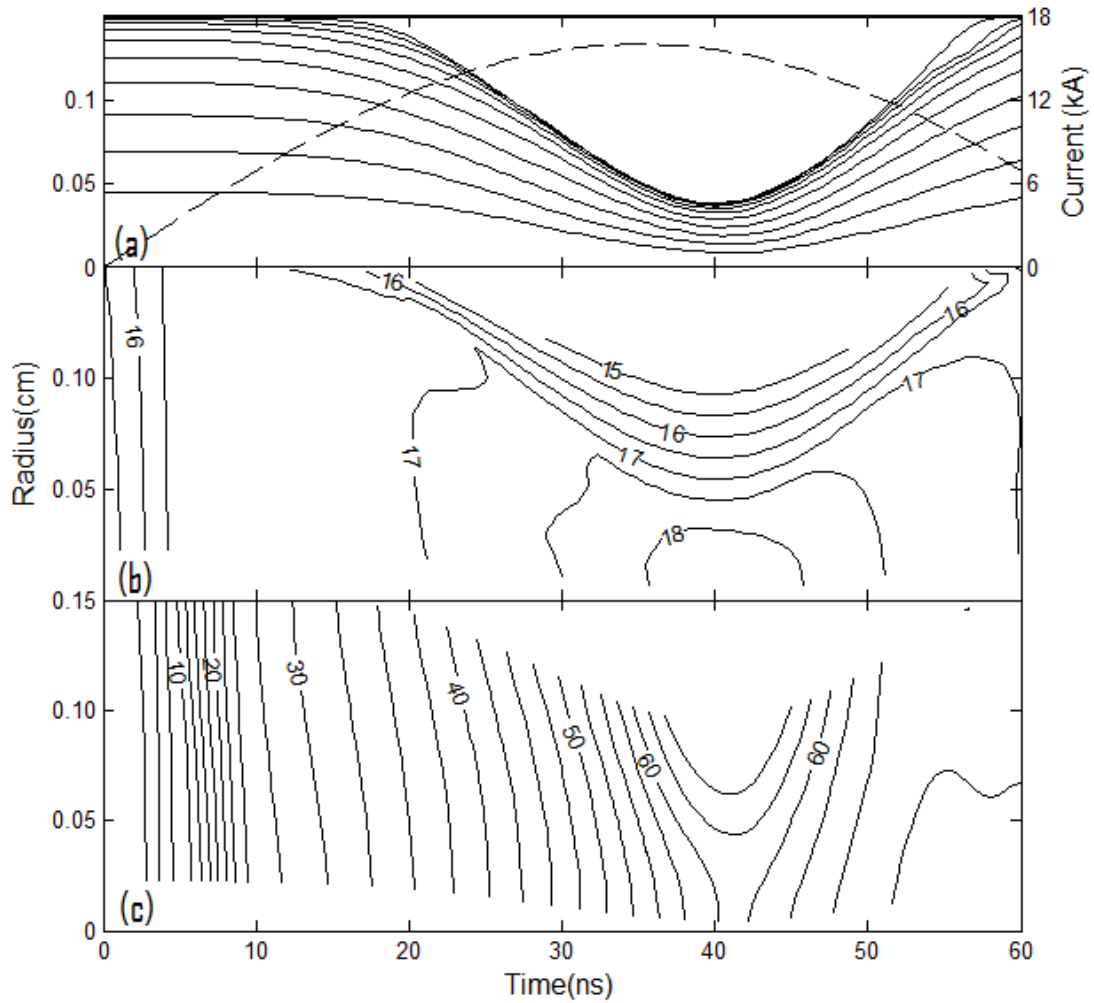


Figure 1. Basic parameters of discharge in capillary with diameter of 3 mm filled with argon at a pressure 0.25 mbar for  $I_0 = 16$  kA and rise time 35 ns. (a) The plasma time-space flow diagram; the dotted line corresponds to the discharge current at outer boundary; (b) contour lines of the decimal logarithm of the electron density measured  $\text{g/cm}^3$  on the  $(t, r)$  plane; (c) contour lines of the electron temperature (measured in eV).

The collisions between particles in the plasma transfer energy from particle to particle in a random fashion, thereby thermalizing the plasma and ionizing the atoms. The level of ionization is set by the electron temperature of the plasma and the atomic binding energies. Generally, multiple ionization states are formed, each with its own characteristic emission lines, leading to a rich complex of lines. By carefully controlling the temperature and density of the plasma, the population of specific ionization species can be preferentially established. Generally, such high temperatures and densities are established at or close to pinch radius.

In Ne-like schemes, the plasma tends to readily adopt the Ne-like stage in plasma. This is because they are very stable, closed-shell ions. They maintain their stability even when faced with temporal, spatial, and other changes and is known as ionization bottlenecks. Under certain plasma conditions (electron density of  $1-5 \times 10^{18} \text{ cm}^{-3}$ , and electron temperature  $60-80$  eV) [23, 24], collisional electron impact excitation of the ground state Ne-like ions produces a population inversion between the  $3p$  ( $J=0$ ) and the  $3s$  ( $J=1$ ) levels resulting in amplification at the 46.9 nm.

### 5.1 Effect of Initial Filling Pressure

From the MHD simulation, the pressure range that gives the electron densities and temperatures that fulfilled the plasma conditions for lasing is between 0.17 to 0.33 mbar. In the case of the peak current fixed at 16 kA, when the initial filling pressure is increased, the magnetic piston leaving the capillary wall is delayed and the stagnation time shifts gradually to the later times. This results in higher electron density and lower electron temperature during pinch time in higher gas filling pressures. Initial gas filling pressures below this range were not selected due to the plasma being overheated. On the other hand, initial gas filling pressures higher than this range were also not selected because the plasma temperature is too low.

These results have been compared with the experimental data from Ref. 8, as reproduced in Fig. 2, which show that lasing actions occur between 0.12 to 0.28 mbar. Here, the solid line is used to guide the eye. However, from our MHD simulation, we determine that the range of gas filling pressures for lasing actions fulfilling plasma condition is between 0.17 to 0.33 mbar (the range bordered by dashed lines). Experimentally, lasing action occurs at lower pressures as compared to our simulation results. This may be due to the fact that the simulation model does not include pre-ionization due to the application of a pre-pulse current.

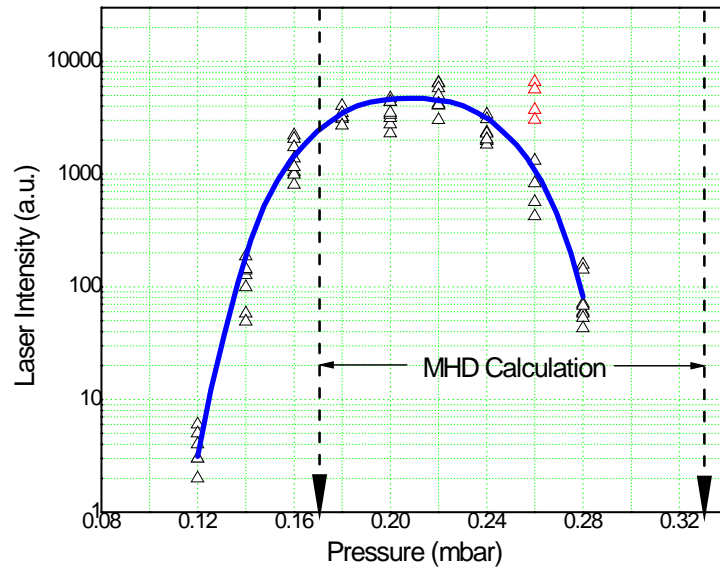


Figure 2. Comparison between experimental data and simulation data. The main discharge current is 16 kA.

### 5.2 Effect of Main Discharge Current

Simulations were also carried out for different peak discharge current ranging from 9 kA to 19 kA. The initial gas filling pressure has been fixed to 0.15 mbar and all other parameters remain the same. The results show that for higher discharge current, the compression by the magnetic piston is more severe. This gives rise not only to higher electron temperature, but also higher density. Overheating of the plasma occurs so that the condition suitable for lasing is destroyed. In order to lower down the electron temperature, higher initial gas filling pressure needed for high discharge current in order to fulfill the plasma conditions. The comparison of the ranges of initial filling pressure for 10.5 kA, 16 kA and 19 kA are shown in Table 1.

Table 1. Comparison between experimental data and simulation data with different discharge peak currents.

Peak of Discharge Current, $I_0$ (kA)	Simulation Pressure Range (mbar)	Experiment Pressure Range (mbar)
10.5	0.10 – 0.15	0.09 – 0.16
16.0	0.17 – 0.33	0.12 – 0.28
19.0	0.23 – 0.41	0.14 – 0.37

## 6 Conclusion

The preliminary results from an MHD modeling of a fast capillary discharge for soft x-ray lasers have been compared with experiment results. In order to get better agreement with respect to experimental data, the MHD should include pre-pulse of the current.

## 7 Acknowledgments

This work has been supported by the Postgraduate Research Fund (PPP) Project No. PS307/2008C, the MOSTI Research grant Grant No. 04-01-03SF0202 and the Fundamental Research Grant Scheme (FRGS), Grant No. FP072/2007C.

## 8 References

1. D.L. Matthews, P.L. Hagelstein, M.D. Rosen, M.J. Eckart, N.M. Ceglio, A.U. Hazi, H. Medeck, B.J. MacGowan, J.E. Trebes, B.L. Whitten, E.M. Campbell, C.W. Hatcher, A.M. Hawryluk, R.L. Kauffman, L.D. Pleasance, G. Rambach, J.H. Scofield, G. Stone, and T.A. Weave, *Phys. Rev. Lett.* **54** 110 (1985)
2. S. Suckewer, C.H. Skinner, H. Milchberg, C. Keane, and D. Voorhees, *Phys. Rev. Lett.* **55** 175 (1985)
3. J.J. Rocca, V.N. Shlyaptsev, F.G. Tomaselli, O.D. Cortazar, D. Hartshorn, and J.L.A. Chilla, *Phys. Rev. Lett.* **73** 2192 (1994)
4. A. Ben-Kish, M. Shuker, R.A. Nemirovsky, A. Fisher, A. Ron and J.L. Schwob, *Phys. Rev. Lett.* **87** 015002-1-4 (2001)
5. G. Niimi, Y. Hayashi, N. Sakamoto, M.K. Nakajima, A. Okino, M. Watanabe, K. Horioka and E. Hotta, *IEEE Trans. Plasma Sci.* **30** 616–21 (2002).
6. G. Tomassetti, A. Ritucci, A. Reale, L. Piliadino, L. Reale, A.V. Kukhlevsky, F. Flora, L. Mezi, J. Kaiser, A. Faenov and T. Pikuz, *Eur. Phys. J. D* **19** 73–7 (2002).
7. S. Heinbuch, M. Grisham, D. Martz and J. J. Rocca, *Opt. Express* **13** 4050–5 (2005).
8. C.A. Tan and K.H. Kwek, *Phys. Rev. A* **75** 043808 (2007).
9. J. von Neumann and R.D. Richtmyer, *J. Applied Phys.* **21** 232 (1950).
10. L. Spitzer, *Physics of Fully Ionized Gases*, 2<sup>nd</sup> ed. (Interscience, New York, 1962).
11. S.V. Dresvin, *Physics and Technology of Low Temperature Plasmas* (Iowa State University Press, 1977).
12. J.J. MacFarlane, *Comp. Phys. Comm.* **56** 259 (1989).
13. N.H. Burnett and A.A. Offenberger, *J. Appl. Phys.* **45** 2155 (1974).
14. A.C. Kolb and R.W.P. McWhirter, *Phys. Fluids* **7** 519 (1964)
15. C. Colombant and G.F. Tonon, *J. Appl. Phys.* **44** 3524 (1973)
16. N. Nakano and H. Kuroda, *Phys. Rev. A* **27** 2168 (1983)
17. D. Mihalas and B. Weibel-Mihalas, *Foundations of Radiation Hydrodynamics* (Dover, New York, 1999)
18. Y.B. Zel'dovich and Y.P. Raizer, *Physics of Shock Waves and High-Temperature Hydrodynamics Phenomena* (Academic, New York, 1966) Vol 1.
19. J.D. Jackson, *Classical Electrodynamics* (Wiley, New York, 1975).
20. K.V. Roberts and D.E. Potter, *Methods in Computational Physics*, edited by B. Alder, S. Fernbach and M. Rotenberg (Academic, New York, 1970) Vol 9.
21. R.D. Richtmyer and K.W. Morton, *Difference Methods for Initial Value Problems*, 2<sup>nd</sup> ed. (Interscience, New York, 1967).
22. J.J. MacFarlane, I. E. Golovkin, and P. R. Woodruff, *Journal of Quantitative Spectroscopy and Radiative Transfer* **99** 381 (2006).
23. V.N. Shlyaptsev, J.J. Rocca, and A.L. Osterheld, *Proc. SPIE Int. Soc. Opt. Eng.* **2520** 365 (1995)
24. D.E. Kim, D.S. Kim, and A.L. Osterheld, *J. Appl. Phys.* **84** 5862 (1998)

# Modeling of fast capillary-discharge for soft x-ray lasers

C P Teh<sup>1,2</sup>, B R Wong<sup>2</sup> and K H Kwek<sup>1</sup>

<sup>1</sup>Department of Physics, University of Malaya, 50603 Kuala Lumpur, Malaysia

<sup>2</sup>Institute Mathematical Sciences, University of Malaya, 50603 Kuala Lumpur, Malaysia

E-mail: tcp5441@um.edu.my

**Abstract.** In this work we present the results of the numerical investigations of the one-dimensional single-fluid magneto-hydrodynamics (MHD) model, with separate electron and ion temperatures, of a capillary-discharge collisional soft x-ray laser. The MHD equations are solved by the Lagrangian cylindrical geometry approach. The effects of the gas filling pressure on the plasma densities and temperatures, and implosion-pinch phase for soft x-ray lasing conditions have been analyzed. The results are compared with experimental measurements of the operating pressure ranges.

## 1. Introduction

Soft x-ray lasers are invaluable tools for studying high-density plasmas and permitting one to see smaller features in microscopy, to write finer patterns in lithography and to generate shorter pulses. These lasers have applications for the materials science community, both inside and outside the laboratory, by supplying detailed information about the atomic structure of new and existing materials. These in turn lead to new scientific understandings, perhaps through surface science, chemistry and physics, providing feedback to the enabling technologies. Development of soft x-ray spectral region is presently in a rapid growth and there is much interplay between the science associated technologies.

In 1984, soft x-ray lasers were first demonstrated in plasmas generated by powerful laser drivers in large laboratories [1, 2]. However, the large pump lasers used for this kind of soft x-ray laser experiments are only available at a few large laser facilities in the world due to their large size, complexity, and extremely high cost. Therefore the demonstration of a capillary discharge soft x-ray laser operating in the transition of Neon (Ne)-like ions by Rocca *et al* [3] in 1994 opened the possibility to develop compact, efficient and simpler soft x-ray laser. This similar demonstration had then been only repeated by Ben-kish *et al* [4] in 2001, followed by the work of Niimi *et al* [5] and Kukhlevsky *et al* [6] in the following year. The quest for improving these systems still continues by parallel efforts involving theory and computer simulations of the experiments to understand the laboratory observation and to optimize the resulting energy density. Even after more than a decade, systems with improved performance and efficiency are still being reported [7].

In this paper, the capillary discharge soft x-ray laser described by Tan and Kwek [8] is modeled using two-temperature, one dimensional single-fluid magneto-hydrodynamics (MHD) equations. The details of the governing equations and the computational simulation will be applied and shown. The model was then utilized to numerically evaluate the time and radial dependences of capillary plasma characteristics of fast capillary discharges with current rise time of around 50 ns and peak currents 16 kA in a capillary 3 mm in diameter filled with pre-ionized argon (Ar) gas. The results were then

compared with experimental data [8] from different initial argon filled pressures. The effects of the gas filling pressure on the plasma densities and temperatures, during implosion-pinch phase for soft x-ray lasing conditions were analyzed.

## 2. Magneto-hydrodynamics model

The basic MHD equations used are described below. The continuity equation (mass conservation) is given by

$$\frac{\partial \rho}{\partial t} + \nabla \cdot (\rho \mathbf{u}) = 0,$$

where  $\rho$  is mass density and  $\mathbf{u}$  is the plasma fluid velocity. Generally, in any steady state process, the rate at which mass enters a system is equal to the rate at which mass leaves the system. In this numerical scheme, the continuity equation is automatically satisfied.

The momentum conservation equation is solved in the one-fluid approximation where the plasma electrons and ions are assumed to flow together as a single fluid. The momentum equations is governed by

$$\rho \frac{d\mathbf{u}}{dt} = -\nabla (P_e + P_i + q) - \mathbf{J} \times \mathbf{B},$$

where  $P_e$  and  $P_i$  are the thermal pressure due to electrons and ions, respectively,  $\mathbf{B}$  denotes the magnetic field induced by the axial current and  $\mathbf{J}$  is the axial component of the electric current density. Here,  $q$  is the von Neumann artificial viscosity. The artificial viscosity, which is included in the equation of motion to handle shocks, effectively smoothes the shock over a small number of zones.

The energy balance for electrons and ions is described by

$$C_{v,e} \frac{dT_e}{dt} = V \nabla \cdot (\kappa_e \nabla T_e) + \psi_{joule} - \left( \frac{dE_e}{dV} + P_e \right) \frac{dV}{dt} - \frac{(T_e - T_i)}{t_{eq}},$$

$$C_{v,i} \frac{dT_i}{dt} = V \nabla \cdot (\kappa_i \nabla T_i) - \left( \frac{dE_i}{dV} + P_i \right) \frac{dV}{dt} + \frac{(T_e - T_i)}{t_{eq}}.$$

where  $C_{v,\alpha}$ ,  $T_\alpha$ ,  $E_\alpha$ ,  $P_\alpha$  and  $\kappa_\alpha$  are, respectively, the specific heat, temperature (in eV), specific internal energy, pressure and thermal conductivity, of the electrons ( $\alpha = e$ ) and ions ( $\alpha = i$ ). While  $V$  is the specific volume,  $\psi_{joule}$  is joule heating term and  $t_{eq}$  is the electron-ion collisional coupling term.

The difference between the temperature diffusion equations for the electrons and ions is the absence of the Joule heating term in the ion equation. Since the currents are mainly due to the lighter electrons, the energy is transferred to the ions through the collision specified by the term involving  $t_{eq}$ .

The magnetic field transport and diffusion equation reads

$$\frac{d\mathbf{B}}{dt} = \frac{\eta}{4\pi} (\nabla \cdot \nabla) \mathbf{B} - (\nabla \cdot \mathbf{u}) \mathbf{B},$$

where  $\eta$  is defined as the plasma electrical resistivity. This equation is obtained using Maxwell equations and generalized Ohm's law neglecting the time variation of the electric field [9].

These MHD equations have been adopted in the Lagrangian reference frame using the specific volume expression. The position of each cell and the velocity on cell boundary are determined by

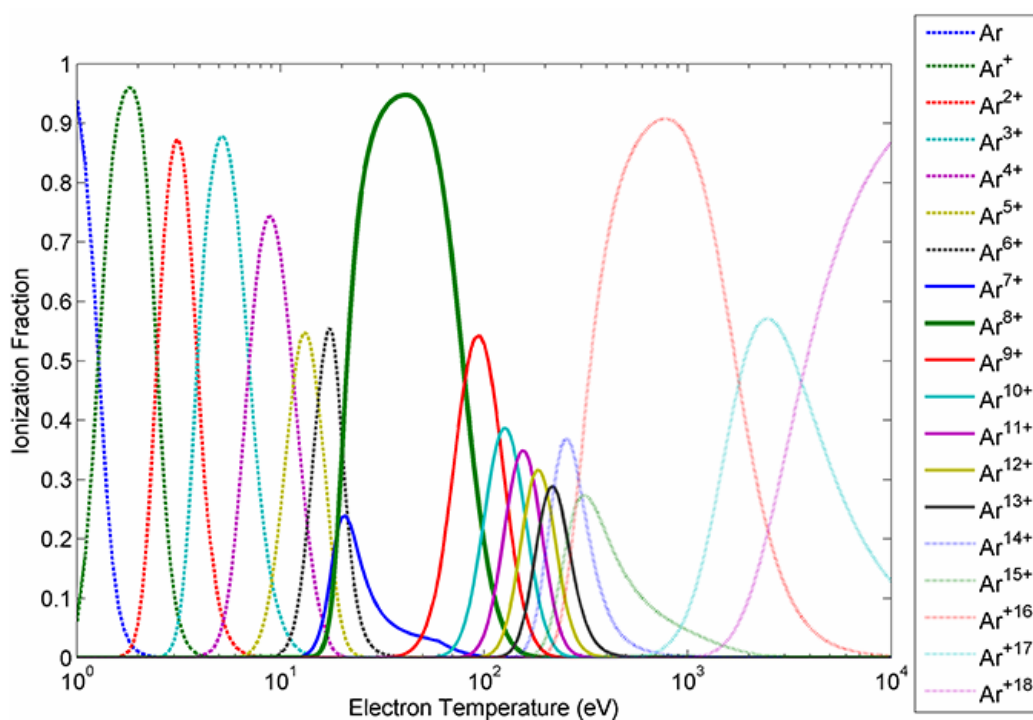
$$\frac{dr}{dt} = u.$$

All dynamical values in the equations evolve as a function of position  $r$  from the capillary axis at a time  $t$ .

### 3. The requirement characteristic of populations and gains in neon-like argon

As a first estimation of absolute gain of this transition, the fractional abundance of charge states is evaluated using steady-state ionization model.

The atomic physics PrismSPECT code [10] solves the equation of state and provides radiative properties for plasma in local thermodynamic equilibrium (LTE) state. The ionization population fractions in the range  $T_e \in 1 - 1000$  eV for a given electron density  $N_e \sim 2.0 \times 10^{18} \text{ cm}^{-3}$  are depicted on the figure 1. This value has been chosen because of the value of the pinch electron density of the case study will be studied in next section. The maximum ionization population fraction of neon-like  $\text{Ar}^{8+}$  ion,  $f^{8+} \approx 0.95$  is accomplished at temperature  $T_e \approx 40$  eV. The temperature range of Ne-like ionization state is approximately between 10 – 200 eV. It should be kept in mind that the steady-state ionization model does not depend on ionization dynamics, namely, ionization plasma history.



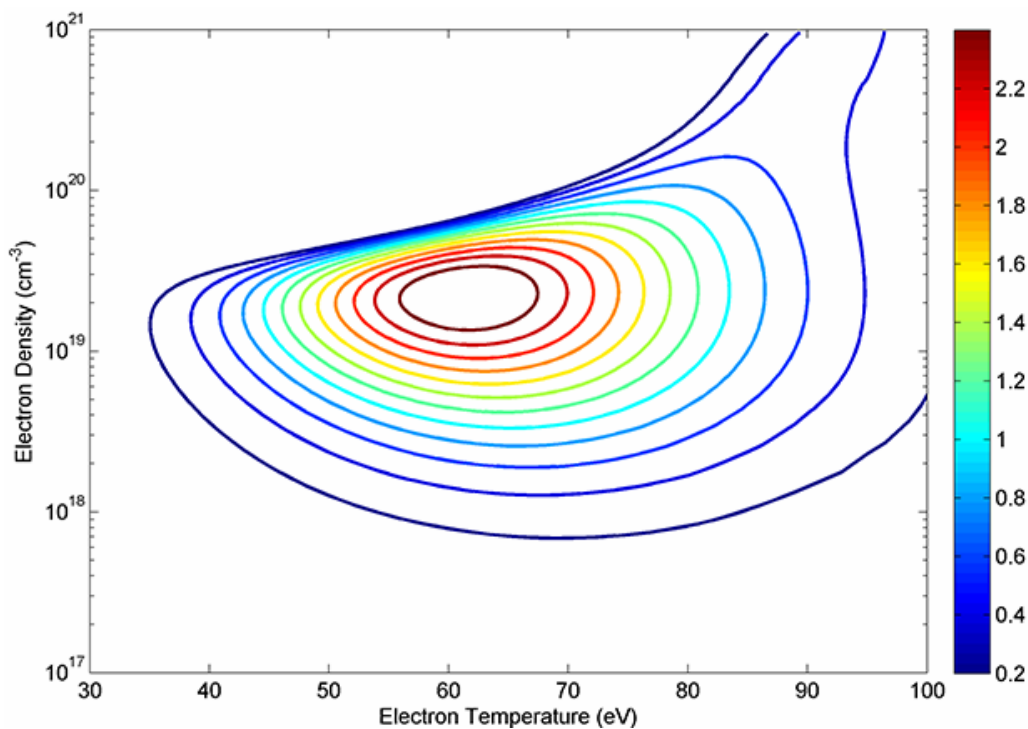
**Figure 1.** Argon ionization fractions dependences on plasma electron temperature for atom density  $N_0 = 2 \times 10^{18} \text{ cm}^{-3}$ .

Figure 2 presents a contour plot of gain against  $N_e$  and  $T_e$  computed using steady-ion ionization model. The effect of reabsorption of the resonance radiations on the distribution of population density of excited-states has been neglected (optically-thin plasma assumption). It has been assumed that  $T_e = T_i$ . This assumption generally sets the upper limit of gain in capillary-discharge.

Figure 2 indicates that a large gain formed for  $N_e \approx 2 \times 10^{18} \text{ cm}^{-3}$ . For the regime  $N_e > 10^{20} \text{ cm}^{-3}$ , collisional depopulation exceeds the radiative decay rates. Hence, the populations become distributed according to the Boltzmann distribution function and the collisional quench of the population inversion occurs (i.e., unsuitable gain regime). Although, the fractional abundance of Ne-like Ar becomes a maximum at  $T_e \approx 40$  eV using the steady-state approximation for ionization model, the optimum regime of gain is approximately at  $T_e \approx 60$  eV, as shown in figure 2. This fact shows a mismatch between electron temperature that maximizes gain and fractional abundance of Ne-like Ar ion, in which is a general problem of Ne-like x-ray lasers [11]. The mismatch arises because the excitation energy into the  $n = 3$  levels is typically three-quarters of the ionization energy and thus a

temperature which gives large ground-state excitation rates will lead to large ionization rates if the electron density is sufficient (the relaxation time for the ionization balance  $\sim 10^{11} n_e^{-1}$ ) [12].

The collisions between particles in the plasma transfer energy from particle to particle in a random fashion, thereby heating the plasma and ionizing the atoms. Generally, multiple ionization states are formed, each with its own characteristic emission lines, leading to a rich spectrum of lines. By carefully controlling the temperature and density of the plasma, the population of specific ionization species can be preferentially established. Generally, such high temperatures and densities are established at or close to pinch radius.



**Figure 2.** The contour of gain in  $3p\ ^1S_0 - 3s\ ^1P_1$  transition as function of the electron temperature and density.

Under certain plasma conditions (electron density of  $0.1 - 4 \times 10^{19} \text{ cm}^{-3}$ , and electron temperature  $\approx 40 - 90 \text{ eV}$ , as in results from figure 2), collisional electron impact excitation of the ground state Ne-like ions produces a population inversion between the  $3p\ (J=0)$  and the  $3s\ (J=1)$  levels resulting in amplification at the  $46.9 \text{ nm}$  wavelength.

#### 4. Results and discussion

Using the general physical model outlined in section 2, the discharge channel can be simulated with specific values of the controlling parameters. The parameters of a working discharge x-ray laser reported in reference [8] are used. Here the radius of the capillary has been fixed at  $0.15 \text{ cm}$ , and current rise time is about  $50 \text{ ns}$ . For this basic situation, the filling pressures and the current profiles are varied to investigate the impact of these variations on the plasma. Initially, the pre-ionized plasma is assumed to be uniformly distributed with  $T_e = T_i = 1 \text{ eV}$ . For the simulations, we use the HELIOS-CR code described in reference [13]. It is a modeling platform that can handle LTE and non-LTE plasmas in one dimension. The peak discharge current  $16 \text{ kA}$  is used in this paper. These are the typical values used in the laser of reference [8].

Figure 3 presents the calculated results for a capillary discharge with a peak current of  $16 \text{ kA}$  and  $0.15 \text{ mbar}$  gas filling pressure. The temporal evolution of the trajectories of argon plasma elements



inside the channel of this configuration is illustrated in figure 3(a). The blue line represents the discharge current. Figure 3(b) shows contour plots of the logarithm of the electron density measured in  $\text{cm}^{-3}$  while figure 3(c) shows the electron temperature measured in eV. These figures also provide quantitative information about the distribution of the plasma parameters inside the channel at different times. Some characteristics features are discussed below.

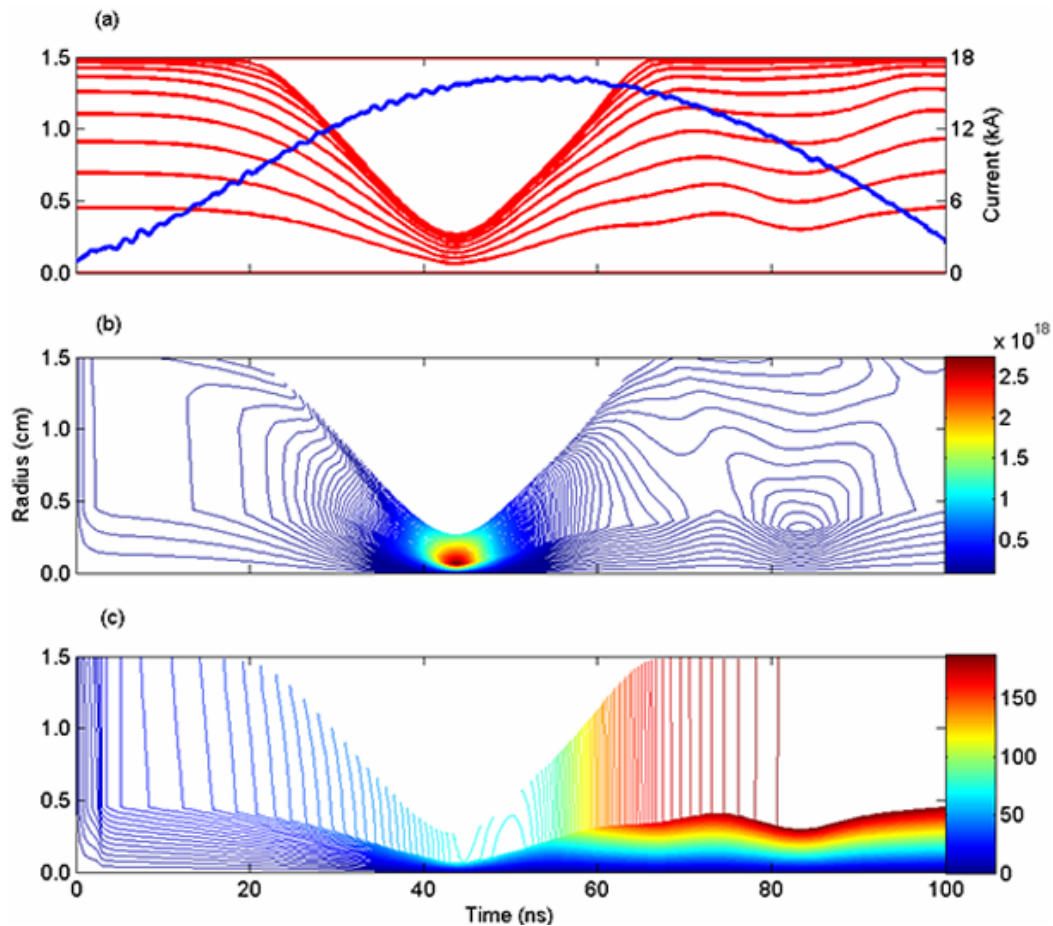


**Figure 3.** Basic parameters of discharge in capillary with diameter of 3 mm filled with argon at a initial gas filling pressure of 0.15 mbar for  $I_0 = 16$  kA and rise time 50 ns. (a) The plasma time-space flow diagram; blue line corresponds to the discharge current at outer boundary; (b) contour lines of the decimal logarithm of the electron density (measured  $\text{cm}^{-3}$ ) on the  $(t, r)$  plane; (c) contour lines of the electron temperature (measured in eV).

The dynamics of a Z-pinch plasma can be described by the balance between the thermal pressure and the magnetic pressure. In the early stages ( $t < 20$  ns) the plasma is not compressed immediately but actually tries to expand due to the fact that the plasma pressure exceeds other forces. However, this expansion is constrained by the rigid wall of the capillary. The pressure in the outer zones of the plasma is due to both the initial filling pressure and Joule heating. Generally, the current tends to flow in the outer part of the cylindrical plasma, and Joule heating occurs due to current passing through the plasma. This heating results in an increase in pressure which can be sufficiently high for the outer regions of the plasma to initially expand before being accelerated inward by the magnetic piston.

When the discharge current has reached a value such that the magnetic pressure is larger than the thermal pressure ( $t > 20$  ns), the plasma is compressed inward onto the axis. At the same time, a

vacuum region appears near the wall and a converging shock wave is formed which propagates towards the channel axis. The shock waves eventually meet at the axis, and are subsequently reflected. During compression, the plasma becomes hotter due to Joule and shock heating, and the thermal pressure increases. Although, before the time 50 ns, when the total current has been increasing towards the maximum value, the discharge current is high, and the Lorentz force dominates. Thus, the compression stops. When the thermal pressure balances the magnetic pressure, the plasma stagnates ( $t \approx 43.5$  ns) and then expands ( $t > 43.5$  ns). During the compression, a high density and temperature plasma on the axis is produced, as shown in figure 3(b) and 3(c). The temperature  $T_e$  reaches the value of 70 eV and continues to heat up to 160 eV during the expansion phase. This is because the inner zones of plasma continue to compress again after the first pinch. The value of electron density  $N_e$  at the pinch is about  $3 \times 10^{18} \text{ cm}^{-3}$ . A hot plasma core with the radial dimension  $r_{core} = 0.266$  mm and central mass density  $\rho_{core} = 1.22 \times 10^{-4} \text{ g/cm}^3$  is formed.

At the stage of expansion the MHD instabilities may break the uniformity of the plasma column, leading to turbulent mixing, enhanced heat transport and resistance. However, from the theory of the classical pinch effect, MHD instabilities begin to evolve when the expansion velocity begins to decrease [14]. If the lasing occurs during the few first nanoseconds after the reflection of the shock wave, MHD instabilities have no time to evolve. The validity of this description of the plasma behavior in the capillary discharge ends at the moment when the diverging shock wave reaches the capillary wall.

The time dependence of small signal gain factor  $G$  is determined by the time dependences of both laser level populations  $n_{3p\ 3S^1}^{8+}$  and  $n_{3s\ 3P^0}^{8+}$ . In this case above (a non-ablating alumina capillary with radius  $r_0 = 1.5$  mm filled with initial gas filling pressure of 0.15 mbar, current pulse with  $T_{1/4} = 50$  ns and current peak value  $I_{max} = 16$  kA) the gain factor has a shape of very short peak with maximum value  $G(t_G) = 0.8 \text{ cm}^{-1}$  at the time  $t_G = 44.5$  ns (see figure 4). The peak value of gain is achieved during the pinch time.

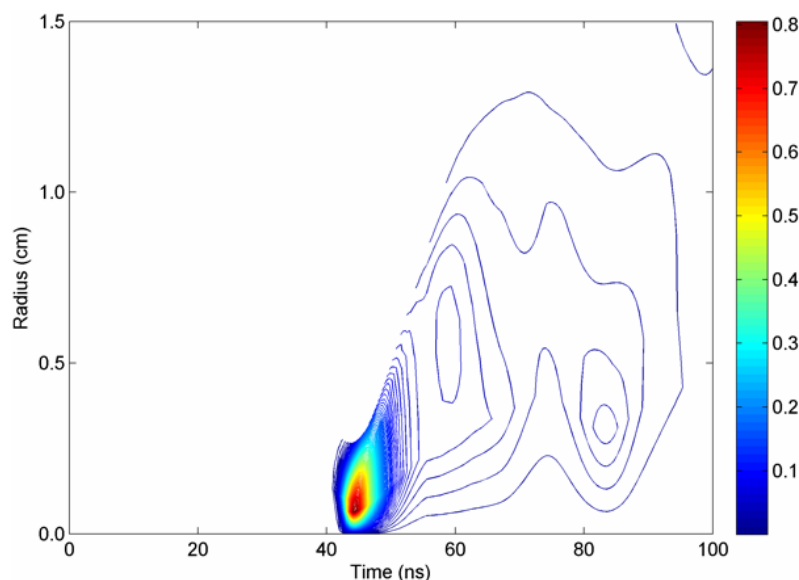


**Figure 4.** The spatial and temporal evolution of gain

## 5. Comparison with experiments

The simulations of the capillary discharge dynamics for  $r_0 = 1.5$  mm,  $T_{1/4} = 50$  ns,  $I_{max} = 16$  kA and various initial gas filling pressure  $p_0$  of argon have been performed here. For given capillary radius  $r_0$  and current waveform, the peak value of gain factor  $G(t_G)$  may be expressed as a function of the

initial gas filling pressure (see figure 5). The gain curve shows that the measurable gain factor for  $r_0 = 1.5$  mm,  $T_{1/4} = 50$  ns,  $I_{max} = 16$  kA is found in the pressure range  $0.11 \text{ mbar} < p_0 < 0.29 \text{ mbar}$ .

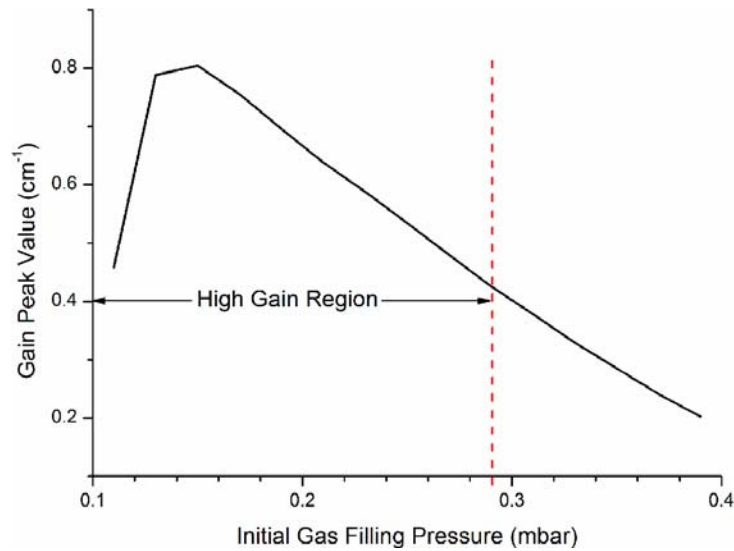


**Figure 5.** Dependence of gain factor peak value on the initial gas filling pressures.

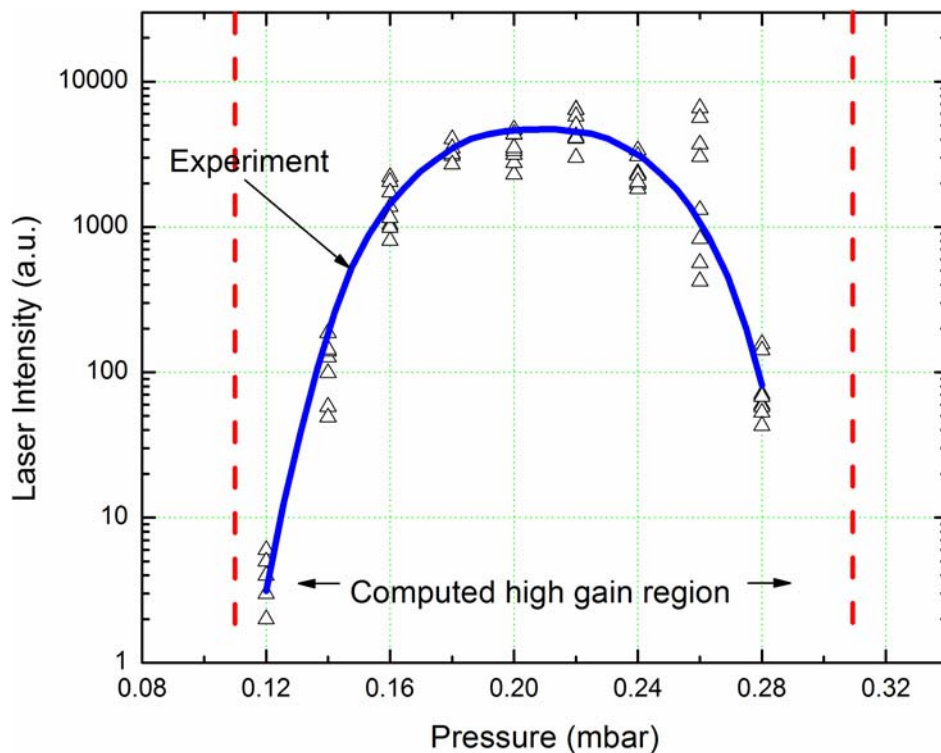


**Figure 6.** Comparison between experimental data and simulation data. The main discharge current is 16 kA.

From the MHD simulation, the electron densities and temperatures that fulfilled the plasma conditions and high gain factors obtained are in between 0.11 to 0.29 mbar. These results have been further computed which included refraction effect due to electron density gradient. The simulation output of the intensity are compared with the experimental data [8] shown in figure 6. The dotted lines

are the range of gas filling pressures that are computed by MHD simulation. The soft x-ray lasers (experimental data) have been produced in the range of 0.12 to 0.28 mbar (the solid line) which show good agreement if compare to simulation data.

## 6. Conclusions

The results from an MHD modeling of a fast capillary-discharge for soft x-ray lasers have been compared with experiment results. The effects of the gas filling pressure on the plasma densities and temperatures, and implosion-pinch phase for soft x-ray lasing conditions resulting in high gain factors have been analyzed. Our findings indicate that the simulations performed gave reasonably good agreement with experiment.

## Acknowledgements

This work has been supported in part by the Postgraduate Research Fund (PPP) Project No. PS330/2009C and in part by University of Malaya Grant RG031/09AFR.

## References

- [1] Matthews D L *et al.* 1985 Demonstration of a soft x-ray amplifier *Phys. Rev. Lett.* **54** 110
- [2] Suckewer S, Skinner C H, Milchberg H, Keane C and Voorhees D 1985 Amplification of stimulated soft x-ray emission in a confined plasma column *Phys. Rev. Lett.* **55** 1753
- [3] Rocca J J, Shlyaptsev V, Tomasel F G, Cortázar O D, Hartshorn D and Chilla J L A 1994 Demonstration of a Discharge Pumped Table-Top Soft-X-Ray Laser *Phys. Rev. Lett.* **73** 2192
- [4] Ben-Kish A, Shuker M, Nemirovsky R A, Fisher A, Ron A and Schwob J L 2001 Plasma Dynamics in Capillary Discharge Soft X-Ray Lasers *Phys. Rev. Lett.* **87** 015002
- [5] Niimi G, Sakamoto N, Nakajima M, Hayashi Y, Watanabe M, Okino A, Horioka K and Hotta E 2002 Study of low current capillary discharge for compact Soft x-ray laser. *AIP Conf. Proc.*: AIP) pp 103-6
- [6] Kukhlevsky S V, Ritucci A, Kozma I Z, Kaiser J, Shlyaptseva A, Tomassetti G and Samek O 2002 Atomic Model Calculations of Gain Saturation in the 46.9 nm Line of Ne-like Ar *Contrib. Plasm. Phys.* **42** 109-18
- [7] Heinbuch S, Grisham M, Martz D and Rocca J J 2005 Demonstration of a desk-top size high repetition rate soft x-ray laser *Opt. Express* **13** 4050
- [8] Tan C A and Kwek K H 2007 Influence of current prepulse on capillary-discharge extreme-ultraviolet laser *Phys. Rev. A* **75** 043808
- [9] Burnett N H and Offenberger A A 1974 Magnetohydrodynamic behavior of a laser-heated solenoid *J. Appl. Phys.* **45** 2155-62
- [10] MacFarlane J J, Golovkin I E, Woodruff P R, Welch D R, Oliver B V, Mehlhorn T A and Campbell R B 2003 *Inertial Fusion Sciences and Applications* (American Nuclear Society)
- [11] Holden P B and Pert G J 1996 Long-wavelength, prepulsed driving as a means to greatly increase the gain in low-Z Ne-like XUV lasers *J. Phys. B: At. Mol. Phys.* **29** 2151
- [12] Whitten B L, London R A and Walling R S 1988 Scaling of neonlike lasers using exploding foil targets *J. Opt. Soc. Am. B* **5** 2537-47
- [13] MacFarlane J J, Golovkin I E and Woodruff P R 2006 HELIOS-CR - A 1-D radiation-magnetohydrodynamics code with inline atomic kinetics modeling *J. Quant. Spectrosc. Radiat. Trans.* **99** 381-97
- [14] Vrba P, Vrbová M, Bobrova N and Sasorov P 2005 Modelling of a nitrogen x-ray laser pumped by capillary discharge *Cent. Eur. J. Phys.* **3** 564-80

## B. Ray- Tracing Code

```
clear;

tic;
f = fopen('data/data16kA_019mbar.txt');

fid6 = fopen('z20_111207.txt','w');

data = fscanf(f, '%13e\t%13e\t%13e\t%13e',[4,11]);

radius = data(1,:);
gain    = data(2,:);
Nu      = data(3,:);
Ne      = data(4,:);

h = 2e-3;%rough one, suppose 1e-5
zc = 20.0;% in cm
am = 0.15; %in cm
len = zc/h;

xstart = -radius(11);
xend = radius(11);
xih = (xend - xstart)/1000;

ystart = -radius(11);
yend = radius(11);
yih = (yend - ystart)/1000;

yi = zeros(1001,1);
for i = 251:500
    xi = xstart +(i-1)*xih;
    ii = i
    for j = 1:1001
        yi(j) = ystart +(j-1)*yih;
        if(yi>0.0)
            if(xi>0.0)
                di(j) = tan(yi(j)/xi);
            end
            if(xi==0.0)
                di(j) = pi/2.0;
            end
            if (xi<0.0)
                di(j)=pi+tan(yi(j)/xi);
            end
        else
            if(xi>0.0)
                di(j) = 2*pi + tan(yi(j)/xi);
            end
            if(xi==0.0)
                di(j) = 3.0*pi/2.0;
            end
            if(xi<0.0)
                di(j) = pi + tan(yi(j)/xi);
            end
        end
    end
end
```

```

matlabpool open;
[r0, z6,x116,v116,x226,v226,iten16,Gs16] = ...
parrk_111207(len,zc,xi,yi,di,h,am,radius,gain,Nu, Ne);
matlabpool close;

for ijk = 1:1001

fprintf(fid6,'%12.5e\t%12.5e\t%12.5e\t%12.5e\t%12.5e\t%12.5e\t%12.5e\t
\r\n',...
        r0(ijk),
x116(ijk),v116(ijk),x226(ijk),v226(ijk),iten16(ijk),Gs16(ijk));
end

end

fclose(fid6);

toc;

function [r0,z6,x116,v116,x226,v226,iten16,Gs16] = ...
parrk_111207(len,zc,xi,yi,dij,h,am,radius,gain,Nu, Ne)

parfor j =1:1001
    ri = sqrt(xi*xi+yi(j)*yi(j));
    di = dij(j);
    k= randi([1 101]);
    ddi = -((am+ri)/zc)+(k-1)*1.5e-4;
    rip = tan(ddi);
    [r0(j),z6(j),x116(j),v116(j),x226(j),v226(j),iten16(j),Gs16(j)]
= ...

rk4ode_111207(@func1,@func2,len,0,zc,ri,rip,di,ddi,h,am,radius,gain,Nu,
Ne);

end
end

function [r0,z6,x116,v116,x226,v226,iten16,Gs16]...
= rk4ode_111207(f1, f2, l,a, b, x10, xd10, x20, xd20, h, am,
r,gain,Nu,Ne)
% Solution of 2nd order ODE using Runge-Kutta 4th order
% with constant step size. ODE solved is converted to
% two 1st order equations. The RHS of the system is
%     dv1/dt = f1(t, x, v)
%     dx1/dt = v1
% See for example rhs_smd.m for forced spring-mass-damper
%
% USAGE: [t, x, v] = rk4ode2(func,a,b,x0,xd0,h)
%
% input  func = name of external function to evaluate the RHS
%         of the ODE (eg 'rhs_smd')
%         a, b = limits of integration
%         x0   = initial condition (position)
%         xd0  = initial condition (velocity)
%         h    = stepsize
%
% output [t, x, v] = solution vectors

```

```

t0 = a;
v10 = xd10;
v20 = xd20;
r0 = x10;

i = 1;
g = fp(r, gain, abs(x10));
j_const = 1.9766866e-9;
I_sat = 6.8e7; %in unit of W/cm^2
Gs=g;
Nui = fp(r, Nu, abs(x10));
if (x10==0.0)
    x10=1e-10;
end
Jp = j_const * Nui * x10*x10/(h*h);
iten0 = (Jp/g)*(exp(g*h)-1);

while t0 < b

    k1x1 = v10;
    k1v1 = feval(f1, t0 , x10 , v10 , r ,Ne);

    k2x1 = v10+k1v1*h/2;
    k2v1 = feval(f1, t0+h/2, x10+k1x1*h/2 , v10+k1v1*h/2,r,Ne );

    k3x1 = v10+k2v1*h/2;
    k3v1 = feval(f1, t0+h/2, x10+k2x1*h/2 , v10+k2v1*h/2,r,Ne );

    k4x1 = v10+k3v1*h;
    k4v1 = feval(f1, t0+h , x10+k3x1*h , v10+k3v1*h,r,Ne );

    i = i+1;
    t1 = t0 + h;

    x11 = x10 + (k1x1 + 2*k2x1 + 2*k3x1 + k4x1)*h/6;
    if (x11>=am)
        x11 = am;
    end
    if (x11<=0)
        x11 = 0.0;
    end

    Gi = fp(r, gain, abs(x11));
    Gs = Gi/(1+(iten0/I_sat));
    if(t0==0.0)
        t0=h;
    end
    iten1 = sqrt(t0/t1)*iten0*exp(Gs*h);

    v11 = v10 + (k1v1 + 2*k2v1 + 2*k3v1 + k4v1)*h/6;

    k1x2 = v20;
    k1v2 = feval(f2, t0 , x20 , v20 , x11, v11);

    k2x2 = v20+k1v2*h/2;
    k2v2 = feval(f2, t0+h/2, x20+k1x2*h/2 , v20+k1v2*h/2, x11, v11);

    k3x2 = v20+k2v2*h/2;
    k3v2 = feval(f2, t0+h/2, x20+k2x2*h/2 , v20+k2v2*h/2, x11, v11);

```

```

k4x2 = v20+k3v2*h;
k4v2 = feval(f2, t0+h , x20+k3x2*h , v20+k3v2*h , x11, v11);

x21 = x20 + (k1x2 + 2*k2x2 + 2*k3x2 + k4x2)*h/6;

v21 = v20 + (k1v2 + 2*k2v2 + 2*k3v2 + k4v2)*h/6;

t0 = t1;
x10 = x11;
v10 = v11;
x20 = x21;
v20 = v21;
iten0 = iten1;
end

z6=t0;
x116=x10;
v116=v10;
x226=x20;
v226=v20;
iten16=iten0;
Gs16=Gs;
end

function [N] = fp(r_in, N_in, r)

nn = length(r_in);
if(r<=r_in(1))
    m1 = (N_in(2)-N_in(1))/(r_in(2)-r_in(1));
    N = (m1*r)-(m1*r_in(1))+N_in(1);
end
if(r>=r_in(nn))
    m = (1e-10-N_in(nn))/(0.15-r_in(nn));
    N = (m*r)-(m*r_in(nn))+N_in(nn);
end
if((r>=r_in(1))&&(r<=r_in(nn)))
    for i = 1:nn-1
        if(r>=r_in(i))
            ii = i;
        end
    end
    m = (N_in(ii+1)-N_in(ii))/(r_in(ii+1)-r_in(ii));
    N = (m*r)-(m*r_in(ii))+N_in(ii);
end
end
end

```



### C. The Derivation of The Energy Balance with Thermal Diffusion for Electrons and Ions

The conservation of electron and ion energy,

$$\frac{\partial e_e}{\partial t} = V \nabla \cdot (\kappa_e \nabla T_e) + V \mathbf{J} \cdot (\eta \mathbf{J}) - \frac{\partial E_e}{\partial t} - P_e V \bar{\nabla} \cdot \mathbf{u} - \frac{\partial e_e}{\partial T_e} \frac{(T_e - T_i)}{t_{eq}} + R_{Abs} - R_{Emis}, \quad (C.1)$$

$$\frac{\partial e_i}{\partial t} = V \nabla \cdot (\kappa_i \nabla T_i) - \frac{\partial E_i}{\partial t} - P_i V \bar{\nabla} \cdot \mathbf{u} + \frac{\partial e_i}{\partial T_i} \frac{(T_e - T_i)}{t_{eq}}, \quad (C.2)$$

and equations of state ( $\alpha = e, i$ )

$$e_\alpha = \frac{RT_\alpha}{(\gamma - 1)}, \quad (C.3)$$

$$p_\alpha V = RT_\alpha, \quad (C.4)$$

where  $e_\alpha$  is internal energy and temperature (in eV) of the electrons ( $\alpha = e$ ) and ions ( $\alpha = i$ ) and  $R$  is the gas constant. In Eq. (C.1) and Eq. (C.2), the term of  $V \bar{\nabla} \cdot \mathbf{u}$  can be replaced by  $\frac{\partial V}{\partial t}$  from the conversation of mass. Using (C.3) to expand  $\partial e_e / \partial t$  gives

$$\frac{\partial e_e}{\partial t} = \frac{\partial e_e}{\partial T_e} \frac{\partial T_e}{\partial t} = \frac{R}{\gamma - 1} \frac{\partial T_e}{\partial t} = C_{v,e} \frac{\partial T_e}{\partial t}. \quad (C.5)$$

Additional,  $\mathbf{J}$  has been defined in Eq. (D.2). So the Eq. (C.1) yield

$$\begin{aligned} C_{v,e} \frac{\partial T_e}{\partial t} = & V \nabla \cdot (\kappa_e \nabla T_e) + \frac{V \eta}{(4\pi)^2} |(\nabla \times \mathbf{B})|^2 - \left( \frac{\partial E_e}{\partial V} + P_e \right) \frac{\partial V}{\partial t} \\ & - C_{v,e} \frac{(T_e - T_i)}{t_{eq}} + R_{Abs} - R_{Emis}. \end{aligned} \quad (C.6)$$

A similar equation results for ion temperature  $T_i$ ,

$$C_{v,i} \frac{\partial T_i}{\partial t} = V \nabla \cdot (\kappa_i \nabla T_i) - \left( \frac{\partial E_i}{\partial V} + P_i \right) \frac{\partial V}{\partial t} + C_{v,i} \frac{(T_e - T_i)}{t_{eq}} - q \frac{\partial V}{\partial t}. \quad (C.7)$$

## D. The Derivation of The Magnetic Field Transport and Diffusion Equation

From Ohm's Law

$$\eta \mathbf{J} = \mathbf{E} + \mathbf{u} \times \mathbf{B}, \quad (\text{D.1})$$

Maxwell's equations,

$$\vec{\nabla} \times \mathbf{B} = 4\pi \mathbf{J} + \frac{1}{c^2} \frac{\partial \mathbf{E}}{\partial t}, \quad (\text{D.2})$$

$$\vec{\nabla} \times \mathbf{E} = -\frac{\partial \mathbf{B}}{\partial t}; \quad (\text{D.3})$$

The assumption has been made that the wave velocity  $\mathbf{u}$  is much less than  $c$ , so that the displacement current in Eq. (D.2) can be neglected. Eq. (D.1) can be expanded to

$$\eta (\vec{\nabla} \times \mathbf{J}) = (\vec{\nabla} \times \mathbf{E}) + [\vec{\nabla} \times (\mathbf{u} \times \mathbf{B})]. \quad (\text{D.4})$$

Substitute Eq. (D.2) and Eq. (D.3) into Eq. (D.4),

$$\frac{\eta}{4\pi} (\vec{\nabla} \times (\vec{\nabla} \times \mathbf{B})) = -\frac{\partial \mathbf{B}}{\partial t} + [\vec{\nabla} \times (\mathbf{u} \times \mathbf{B})]. \quad (\text{D.5})$$

Using vector calculus identities, Eq. (D.5) can be expanded to

$$\frac{\eta}{4\pi} [\vec{\nabla} (\vec{\nabla} \cdot \mathbf{B}) - (\vec{\nabla} \cdot \vec{\nabla}) \mathbf{B}] = -\frac{\partial \mathbf{B}}{\partial t} + [(\vec{\nabla} \cdot \mathbf{B}) + (\mathbf{B} \cdot \vec{\nabla})] \mathbf{u} - [(\vec{\nabla} \cdot \mathbf{u}) + (\mathbf{u} \cdot \vec{\nabla})] \mathbf{B}, \quad (\text{D.7})$$

In the cylindrical geometry,  $\mathbf{B} = B\mathbf{e}_\theta$ ,  $\mathbf{J} = J\mathbf{e}_z$ ,  $\mathbf{E} = E\mathbf{e}_z$ , and  $\mathbf{u} = u\mathbf{e}_r$ , and so we obtain the magnetic field diffusion equation as reads,

$$\frac{\partial \mathbf{B}}{\partial t} = \frac{\eta}{4\pi} (\nabla \cdot \nabla) \mathbf{B} - (\nabla \cdot \mathbf{u}) \mathbf{B}. \quad (\text{D.8})$$

## References

1. D. L. Matthews, P. L. Hagelstein, M. D. Rosen, M. J. Eckart, N. M. Ceglio, A. U. Hazi, H. Medeck, B. J. MacGowan, J. E. Trebes, B. L. Whitten, E. M. Campbell, C. W. Hatcher, A. M. Hawryluk, R. L. Kauffman, L. D. Pleasance, G. Rambach, J. H. Scofield, G. Stone, and T. A. Weaver, "Demonstration of a Soft X-Ray Amplifier," *Phys. Rev. Lett.* **54**, 110 (1985).
2. H. I. Smith, and F. Cerrina, "X-ray Lithography for ULSI Manufacturing," *Micro lithography World* **Winter** 10 (1997).
3. D. Attwood, *Soft X-Rays and Extreme Ultraviolet Radiation: Principles and Applications* (Cambridge University Press Cambridge, 1999).
4. C. G. Wahlström, J. Larsson, A. Persson, T. Starczewski, S. Svanberg, P. Salières, P. Balcou, and A. L'Huillier, "High-order harmonic generation in rare gases with an intense short-pulse laser," *Phys. Rev. A* **48**, 4709 (1993).
5. J. J. Macklin, J. D. Kmetec, and C. L. Gordon, "High-order harmonic generation using intense femtosecond pulses," *Phys. Rev. Lett.* **70**, 766 (1993).
6. C. G. Durfee, S. Backus, M. M. Murnane, and H. C. Kapteyn, "Ultrabroadband phase-matched optical parametric generation in the ultraviolet by use of guided waves," *Opt. Lett.* **22**, 1565-1567 (1997).
7. R. Dendy, *Plasma Physics: An Introductory Course* (Cambridge University Press, 1993).
8. J. M. Bridges, C. L. Cromer, and T. J. McIlrath, "Investigation of a laser-produced plasma VUV light source," *Appl. Opt.* **25**, 2208-2214 (1986).
9. N. M. Ceglio, "Revolution in X-ray optics," *J. X-ray Sci. Technol.* **1**, 7-78 (1989).
10. M. A. Klosner, H. A. Bender, W. T. Silfvast, and J. J. Rocca, "Intense plasma discharge source at 13.5 nm for extreme-ultraviolet lithography," *Opt. Lett.* **22**, 34-36 (1997).
11. J. J. Rocca, V. Shlyaptsev, F. G. Tomasel, O. D. Cortázar, D. Hartshorn, and J. L. A. Chilla, "Demonstration of a Discharge Pumped Table-Top Soft-X-Ray Laser," *Phys. Rev. Lett.* **73**, 2192 (1994).
12. J. Goodberlet, S. Basu, M. H. Muendel, S. Kaushik, T. Savas, M. Fleury, and P. L. Hagelstein, "Observation of gain in a recombining H-like boron plasma," *J. Opt. Soc. Am. B* **12**, 980-986 (1995).
13. M. A. Klosner, and W. T. Silfvast, *Opt. Lett.* **23**, 1609 (1998).
14. Martin C Richardson, Andrew F. Vasil'ev, Steve E. Grantham, Kai Gabel, and Masataka Kado, "Development of x-ray microscopy systems based on laser plasma sources," in *Applications of Laser Plasma Radiation*, M. C. Richardson, ed. (SPIE Proc., 1994), p. 97.
15. R. C. Elton, *X-Ray Lasers* (Academic, 1990).

16. J. J. Rocca, "X-ray Laser: 1996," in *IOP Conf. Ser.*, S. Svanberg, and C.-G. Wahlstrom, eds. (IOP, Bristol, 1996), p. 176.
17. J. J. MacFarlane, I. E. Golovkin, and P. R. Woodruff, "HELIOS-CR - A 1-D radiation-magnetohydrodynamics code with inline atomic kinetics modeling," *J. Quant. Spectrosc. Radiat. Trans.* **99**, 381-397 (2006).
18. C. A. Tan, and K. H. Kwek, "Influence of current prepulse on capillary-discharge extreme-ultraviolet laser," *Phys. Rev. A* **75**, 043808 (2007).
19. W. T. Silfvast, *Laser Fundamentals* (Cambridge University Press, 1996).
20. R. W. P. McWhirter, and A. G. Hearn, "A Calculation of the Instantaneous Population Densities of the Excited Levels of Hydrogen-like Ions in a Plasma," *Proc. Phys. Soc.* **82**, 641 (1963).
21. S. Suckewer, and P. Jaeglé, "X-Ray laser: past, present, and future," *Laser Phys. Lett.* **6**, 411 (2009).
22. M. J. Seaton, "Radiative recombination of hydrogenic ions," *Mon. Not. R. Astron. Soc.* **119**, 81 (1959).
23. M. J. Seaton, "The Impact Parameter Method for Electron Excitation of Optically Allowed Atomic Transitions," *Proc. Phys. Soc.* **79**, 1105 (1962).
24. N. H. Burnett, and P. B. Corkum, "Cold-plasma production for recombination extremeultraviolet lasers by optical-field-induced ionization," *J. Opt. Soc. Am. B* **6**, 1195-1199 (1989).
25. Y. Nagata, K. Midorikawa, S. Kubodera, M. Obara, H. Tashiro, and K. Toyoda, "Soft-x-ray amplification of the Lyman-  $\alpha$  transition by optical-field-induced ionization," *Phys. Rev. Lett.* **71**, 3774 (1993).
26. P. Bogen, H. Conrads, G. Gatti, and W. Kohlhaas, "Continuum Radiation Source of High Intensity," *J. Opt. Soc. Am.* **58**, 203-206 (1968).
27. J. J. Rocca, O. D. Cortázar, F. G. Tomasel, and B. T. Szapiro, "Efficient generation of highly ionized calcium and titanium plasma columns for collisionally excited soft-x-ray lasers in a fast capillary discharge," *Phys. Rev. E* **48**, R2378 (1993).
28. J. J. Rocca, O. D. Cortazar, B. Szapiro, K. Floyd, and F. G. Tomasel, "Fast-discharge Excitation of Hot Capillary Plasmas for Soft-x-ray Amplifiers " *Phys. Rev. E* **47**, 1299 (1993).
29. J. von Neumann, and R. D. Richtmyer, "A Method for the Numerical Calculation of Hydrodynamic Shocks," in *J. Appl. Phys.*(AIP, 1950), pp. 232-237.
30. L. Spitzer, *Physics of fully ionized gases* (Interscience Publishers, New York, 1962).
31. S. V. Dresvin, and A. V. Donskoy *Physics and technology of low-temperature plasmas* (Iowa State University Press, Ames, 1977).

32. J. J. Macfarlane, "IONMIX - a code for computing the equation of state and radiative properties of LTE and non-LTE plasmas," *Comput. Phys. Commun.* **56**, 259-278 (1989).
33. N. H. Burnett, and A. A. Offenberger, "Magnetohydrodynamic behavior of a laser-heated solenoid," *J. Appl. Phys.* **45**, 2155-2162 (1974).
34. A. C. Kolb, and R. W. P. McWhirter, "Ionization Rates and Power Loss from theta-Pinches by Impurity Radiation," *Phys. Fluids* **7**, 519-531 (1964).
35. D. Colombant, and G. F. Tonon, "X-ray emission in laser-produced plasmas," *J. Appl. Phys.* **44**, 3524-3537 (1973).
36. N. Nakano, and H. Kuroda, "X-ray generation from laser-produced plasmas and its atomic-number dependence," *Phys. Rev. A* **27**, 2168 (1983).
37. D. Mihalas, and B. Weibel-Mihalas, *Foundations of radiation hydrodynamics* (Oxford University Press, New York, 1984).
38. I. A. B. Zel'dovich, W. D. Hayes, R. F. Probstein, and I. U. P. Raizer, *Physics of shock waves and high-temperature hydrodynamic phenomena* (Academic Press, New York, 1966).
39. J. D. Jackson, *Classical electrodynamics* (Wiley, New York, 1975).
40. D. L. Chapin, J. J. Duderstadt, and D. R. Bach, "Numerical studies of exploding-wire plasmas," *J. Appl. Phys.* **45**, 1726 (1974).
41. S. Humphries, and C. Ekdahl, "Finite-element simulation code for high-power magnetohydrodynamics," *Laser Part. Beams* **16**, 405-430 (1998).
42. B. J. Alder, S. Fernbach, and M. Rotenberg, *Methods in computational physics : advances in research and applications. Vol.9, Plasma physics* (Academic Press, New York ; London, 1970).
43. R. D. Richtmyer, and K. W. Morton, *Difference methods for initial-value problems* (Interscience Publishers, New York, 1967).
44. "NIST: Atomic Spectra Database Levels Form," (National Institute of Standards and Technology).
45. M. Masnavi, M. Nakajima, and K. Horioka, "Effect of nonequilibrium ionization process on gain of neon-like argon x-ray laser " *J. Appl. Phys.* **95**, 434 (2004).
46. J. J. MacFarlane, I. E. Golovkin, P. R. Woodruff, D. R. Welch, B. V. Oliver, T. A. Mehlhorn, and R. B. Campbell, *Inertial Fusion Sciences and Applications* (American Nuclear Society, 2003 ).
47. P. B. Holden, and G. J. Pert, "Long-wavelength, prepulsed driving as a means to greatly increase the gain in low-Z Ne-like XUV lasers," *J. Phys. B: At. Mol. Phys.* **29**, 2151 (1996).
48. B. L. Whitten, R. A. London, and R. S. Walling, "Scaling of neonlike lasers using exploding foil targets," *J. Opt. Soc. Am. B* **5**, 2537-2547 (1988).

49. N. A. Bobrova, S. V. Bulanov, D. Farina, R. Pozzoli, T. L. Razinkova, J. I. Sakai, P. V. Sasorov, and I. V. Sokolov, "MHD simulations of plasma dynamics in pinch discharges in capillary plasmas," *Laser and Particle Beams* **18**, 623-638 (2000).
50. J. J. Rocca, F. G. Tomasel, M. C. Marconi, V. N. Shlyaptsev, J. L. A. Chilla, B. T. Szapiro, and G. Guidice, "Discharge-pumped soft-x-ray laser in neon-like argon," *Phys. Plasmas* **2**, 2547 (1995).
51. G. Niimi, Y. Hayashi, N. Sakamoto, M. Nakajima, A. Okino, M. Watanabe, K. Horioka, and E. Hotta, "Development and characterization of a low current capillary discharge for X-ray laser studies," *IEEE T Plasma Sci* **30**, 616-621 (2002).
52. S. Heinbuch, M. Grisham, D. Martz, and J. J. Rocca, "Demonstration of a desk-top size high repetition rate soft x-ray laser," *Opt. Express* **13**, 4050 (2005).
53. R. A. Nemirovsky, A. Ben-Kish, M. Shuker, and A. Ron, "Effect of Neutral Atoms on a Capillary-Discharge Z Pinch," *Phys. Rev. Lett.* **82**, 3436 (1999).
54. R. A. Nemirovsky, A. Ben-Kish, M. Shuker, and A. Ron, "Erratum: Effect of Neutral Atoms on a Capillary-Discharge Z Pinch [*Phys. Rev. Lett.* 82, 3436 (1999)]," *Phys. Rev. Lett.* **83**, 660 (1999).
55. M. Masnavi, M. Nakajima, and K. Horioka, "Numerical Study on Gain Coefficient of a Capillary-Discharged Neon-Like Argon X-Ray Laser," *IEEJ Trans. FM* **126**, 250 (2006).
56. V. N. Shlyaptsev, A. V. Gerusov, A. V. Vinogradov, J. J. Rocca, O. D. Cortazar, F. Tomasel, and B. Szapiro, "Modeling of fast capillary discharge for collisionally excited soft X-ray lasers; comparison with experiments," in *Ultrashort Wavelength Lasers II*(Proc. SPIE, 1993), p. 99.
57. J. J. Gonzalez, M. Frati, J. J. Rocca, V. N. Shlyaptsev, and A. L. Osterheld, "High-power-density capillary discharge plasma columns for shorter wavelength discharge-pumped soft-x-ray lasers," *Phys. Rev. E* **65**, 026404 (2002).
58. V. N. Shlyaptsev, J. J. G. Rocca, and A. L. Osterheld, "Dynamics of a Capillary Discharge X-ray Laser " in *Soft X-Ray Lasers and Applications*, J. J. G. Rocca, and P. L. Hagelstein, eds. (Proc. SPIE, San Diego, CA, USA, 1995), p. 365.
59. M. C. Marconi, C. H. Moreno, J. J. Rocca, V. N. Shlyaptsev, and A. L. Osterheld, "Dynamics of a microcapillary discharge plasma using a soft x-ray laser backlighter," *Phys. Rev. E* **62**, 7209 (2000).
60. C. Moreno, and et al., "Two-dimensional near-field and far-field imaging of a Ne-like Ar capillary discharge table-top soft-x-ray laser," *Phys. Rev. A* **58**, 1509 (1998).
61. B. H. P. Broks, W. Dijk, and J. J. A. M. v. d. Mullen, "Parameter study of a pulsed capillary discharge waveguide," *J. Phys. D: Appl. Phys.* **39**, 2377 (2006).

62. N. A. Bobrova, S. V. Bulanov, D. Farina, R. Pozzoli, T. L. Razinkova, and P. V. Sasorov, "Magnetohydrodynamic simulation of capillary plasmas," *Plasma Phys. Rep.* **24**, 1 (1998).
63. T. P. Hughes, *Plasmas and Laser Light* (Wiley, New York, 1975).
64. R. A. London, "Beam optics of exploding foil plasma x-ray lasers," *Phys. Fluids* **31**, 184-192 (1988).
65. E. E. Fill, "Ray trajectories in line-focused laser plasmas," *J. Opt. Soc. Am. B* **14**, 1505-1510 (1997).
66. J. J. Rocca, M. C. Marconi, J. L. A. Chilla, D. P. Clark, F. G. Tomasel, and V. N. Shlyaptsev, "Discharge-driven 46.9-nm amplifier with gain-length approaching saturation," *Selected Topics in Quantum Electronics, IEEE Journal of* **1**, 945-948 (1995).
67. J. L. A. Chilla, and J. J. Rocca, "Beam optics of gain-guided soft-x-ray lasers in cylindrical plasmas," *J. Opt. Soc. Am. B* **13**, 2841-2851 (1996).
68. M. Born, and E. Wolf, *Principles of Optics: Electromagnetic Theory of Propagation, Interference and Diffraction of Light* (Cambridge University Press, 1997).
69. F. Girard, J. G. Lunney, J. Larour, and R. Dussart, "Interpretation of capillary discharge EUV pinhole images using a ray-tracing code," *J. Phys. D: Appl. Phys.* **35**, 1164 (2002).
70. D. Benredjem, J. Kuba, C. Möller, and O. Z. Zabaydullin, "Modeling of saturation and refraction in x-ray lasers," *Phys. Rev. A* **67**, 043816 (2003).
71. A. Sureau, and P. B. Holden, "From amplification of spontaneous emission to saturation in x-ray lasers: A Maxwell-Bloch treatment," *Phys. Rev. A* **52**, 3110 (1995).
72. G. J. Pert, "Output characteristics of amplified-stimulated-emission lasers," *J. Opt. Soc. Am. B* **11**, 1425-1435 (1994).
73. P. Vrba, M. Vrbová, N. Bobrova, and P. Sasorov, "Modelling of a nitrogen x-ray laser pumped by capillary discharge," *Cent. Eur. J. Phys.* **3**, 564-580 (2005).
74. N. A. Bobrova, S. V. Bulanov, T. L. Razinkova, and P. V. Sasorov, "Dynamics of a pinch discharge in capillaries," *Plasma Phys. Rep.* **22**, 349 (1996).
75. N. S. Kampel, A. Rikanati, I. Be'ery, A. Ben-Kish, A. Fisher, and A. Ron, "Feasibility of a nitrogen-recombination soft-x-ray laser using capillary discharge Z pinch," *Phys. Rev. E* **78**, 056404 (2008).
76. A. Ben-Kish, M. Shuker, R. A. Nemirovsky, A. Fisher, A. Ron, and J. L. Schwob, "Plasma Dynamics in Capillary Discharge Soft X-Ray Lasers," *Phys. Rev. Lett.* **87**, 015002 (2001).